MEASUREMENTS AND MODELS OF COLLOIDAL PARTICLE DYNAMICS AND ENERGY LANDSCAPES IN MAGNETIC FIELDS AND WITH ADDITIVES IN SOLUTION

by
Anna Chandra Helfeld Coughlan

A dissertation submitted to Johns Hopkins University in conformity with the requirements for the degree of Doctor of Philosophy

Department of Chemical and Biomolecular Engineering
Johns Hopkins University
Baltimore, Maryland
July 2017

ABSTRACT

Measurements and Models of Colloidal Particle Dynamics and Energy Landscapes in Magnetic Fields and with Additives in Solution (July 2017)

Anna Chandra Helfeld Coughlan, B.S., University of Rochester

Academic Advisor: Dr. Michael A. Bevan

Understanding colloidal interactions upon the application of external fields or the addition of secondary components has huge implications for engineering new particle-based materials and products. Electric or magnetic fields can control many particle collective dynamics and structures, leading to novel ordered materials, and can be used for studying nonequilibrium state behavior and for creating innovative active particle systems. Similarly, modulating particle-surface interactions in the presence of additives could enable the design of particles that favorably deposit onto a desired substrate for personal care products and drug delivery. In this dissertation, two different colloidal systems are studied and the dynamics and energies of both are fully characterized. For the first system, the fundamental phenomena influencing magnetic particle behavior in a rotating magnetic field were identified by matching simulations with video microscopy experimental data. In the second system, the mechanisms of core-shell microcapsule binding were characterized as a function of surfactant and polymer concentrations.

Magnetic particle interactions and assembly in rotating magnetic fields were systematically quantified by first measuring single particle and doublet rotation and particle-particle separation across a frequency range for two different field amplitudes. Then, multiple particle assembly from a chain to a condensed structure was measured as a function of field amplitude and frequency. Stochastic models were also developed in

parallel to match the one, two and multiple particle experimental observations and to unequivocally show how specific variables and physics in the model influence key features in the real system. The simulations were then used to further characterize the kinetics and thermodynamics by solving the one-dimensional Fokker-Planck (FP) equation for effective pair potentials for the two-particle system and an order-parameter FP equation to characterize the assembly process for multiple particle systems. The resulting diffusivity and effective energy landscapes illustrate how particle interactions, assembly pathways, and microstructures can be tuned by applied field conditions.

Total Internal Reflection Microscopy (TIRM) was conducted on two different anionic microcapsules, as provided by an industry collaborator, to study how fragrance particle deposition onto human hair can be engineered under shampooing conditions. Experimental videos of the capsules interacting with a glass slide, which is negatively charged to mimic human hair, were analyzed as a function of increasing either amphiphilic surfactant or cationic polymer weight percent. Image analysis algorithms enabled us to capture particle trajectories in *x, y* and *z*, from which deposition lifetimes and potential energy profiles were calculated. The results revealed the various interactions that influence capsule deposition and will inform future work on how the capsules deposit in solutions with both surfactants and polymers.

Committee: Prof. Michael A. Bevan (academic advisor, ChemBE)
Prof. Joelle Frechette (ChemBE)
Prof. Rebecca Schulman (ChemBE)
Prof. Robert L. Leheny (Phys and Astro)
Prof. Francesca Serra (Phys and Astro)

for Dorothy Gordon Helfeld, Michael Coughlan and Joseph Coughlan

ACKNOWLEDGEMENTS

I would like to thank my advisor, Dr. Michael A. Bevan, who nurtured a sense of curiosity and discovery. He taught me how to think like a researcher, to be critical, to work independently, and to explore new ideas and theories that I had never considered. I am grateful for the opportunity to conduct both experiments and simulations as part of my Ph.D. work, and for the faith Dr. Bevan had in me to be successful in this challenging endeavor to do both types of research.

I am exceedingly grateful to Dr. Robert L. Leheny who welcomed me into his laboratory to use the magnetic quadrupole set-up, sat down with me informally several times to discuss the progress of my project, as well as formally sat on several of my annual reviews over the years. I am also grateful to the various students in the Leheny Lab (Clayton LaPointe, Joel Rovner, Dan Allan, Kui Chen, David Rivas, Bilyana Tzolova) who either built some of the equipment, taught me how to use the set-up, worked with me to alter or develop new control codes, or just offered friendship and stimulating conversation about our various research projects.

I would like to thank Dr. Joelle Frechette for her positive guidance over the years as she served on all of my annual reviews and offered her wholehearted support when I applied to various fellowships and she supported me in my general career development. I want to thank Dr. Rebecca Schulman and Dr. Francesca Serra for agreeing to serve on my committee and to Dr. Zachary Gagnon and Dr. Sean Sun for agreeing to be alternates. Dr. Sun also taught a wonderful class on statistical mechanics that deepened my understanding of the topic, and I appreciate our discussions. Dr. Gagnon as well as Dr. Chao Wang also

served on annual reviews of my work early in my graduate career and I thank them for their feedback.

I wholeheartedly thank past and current Bevan group members. Dr. Tara D. Edwards was a phenomenal and meticulous mentor on the experimental techniques in the lab, and corresponded with me even after she had graduated. I very much appreciate the help of Dr. Yuguang Yang and Dr. Daniel J. Beltrán Villegas, who really pioneered a lot of the simulation work and low-dimensional modeling techniques. I want to thank the current postdoc, Dr. Isaac Torres-Diaz, for being a great collaborator on the microcapsule project and for being a friend and mentor in the lab. Matt Petroff and I have also had many fruitful discussions and brainstorming sessions. I want to thank past and current members of the Frechette lab (particularly Charles Dhong and Georgia Pilkington) for being a great "sister" lab, and for our combined lab lunches and social activities at conferences.

I want to thank Dr. Tyrel McQueen for letting me use his particle property measurement system, and to Zachary Kelley and Dr. David Wallace for working with me to use the equipment. I would like to thank Dr. Huda Jerri for her support as a collaborator and for acquiring funding for the microcapsule project. Her perspective as an industry scientist has been educational.

I would like to thank all of my family for their support: my wife Xin Yi Chan, my parents Debbie Helfeld and Rich Coughlan, my brother Daniel Coughlan, my grandfather Edward Helfeld and my grandmother Joan Coughlan. I would also like to thank my cohort in the PhD program, especially Tina Xiong. I would like to thank all of my friends for their support and for the fun times.

TABLE OF CONTENTS

Page

LIST OF TABLES

TABLE Page

LIST OF FIGURES

FIGURE Page

1. INTRODUCTION

1.1 Significance and Objective

1.1.1 Significance

Colloids are nano- to micro-sized particles that experience Brownian motion and are ubiquitous in our lives, found in consumer products,[2] drug and medical applications,[3] and complex materials.[4] The interactions between the particles themselves and with surrounding substrates directly impacts the efficacy of the particles' prescribed function. For example, often it is desirable to control colloidal stability in a solution, meaning the degree to which they are repelled from each other and surfaces, can freely diffuse, and form aggregates, which may cause them to sediment.[5, 6] Or for drug delivery and consumer products, the goal is to control the particle trajectories,[7, 8] eventual deposition onto a target site,[9, 10] while also minimizing toxicity.[11] In materials applications, colloids can be used to fulfill the ideal paradigm of bottom-up assembly,[12, 13] or the ability to form structures by merely tuning the interactions of all of the parts, and enabling them to orient and position themselves into the final configuration, rather than fabricating materials via inefficient top-down techniques such as lithography.[14, 15] The study of colloids is also of interest from a fundamental perspective, as they can be visualized directly under a microscope due to their size,[16] in contrast to molecules and atoms. As such, colloids serve as popular model systems for studying phase behavior[17] and for understanding active, nonequilibrium systems found in nature.[18, 19]

Colloidal particle interactions can be tuned by the application of external fields and by adding various additional components to a solution. Electric and magnetic fields have been used to assemble particles into crystals, hierarchical structures, and complex 3D

architectures.[20-22] Surfactants and polymers can induce attraction or repulsion between particles or between particles and surfaces, leading to ordered structures, disordered arrested states, or to completely stable solutions.[23] Models that mimic the colloidal particle behavior observed in experiments can be powerful tools, useful for quantifying the exact phenomena influencing the interactions. In addition, models enable researchers to engineer and test new systems in computer simulations first before eventually testing them in the laboratory.

Time-dependent magnetic fields have been studied to make ordered materials out of colloids,[24, 25] to direct drug particles[26] and to control rheological properties of particle-based fluids.[27] Although many experimental results show the breadth of behaviors and the potential of controlling colloids with magnetic fields, comprehensive models and a thorough understanding of the physics of these systems have been lacking and are crucial to pioneering applications. Rotating and toggling magnetic fields create nonequilibrium, dissipative effects, thus simulations must be dynamic to reflect the time-dependence and the influence of non-conservative forces. Therefore, Brownian dynamics[28] (BD, pairwise hydrodynamics) or Stokesian dynamics[29] (SD, multi-body hydrodynamics) simulations that solve the Langevin equation are the most appropriate models to use in this system, as opposed to equilibrium Monte Carlo simulations. With the addition of more particles to both experiments and simulations, the system also increases in dimensionality, making it more challenging to describe the observed structures quantitatively. As a consequence, order parameter or low-dimensional modeling can be applied to simplify collective colloidal interactions and capture main dynamic modes.

In many colloidal applications, the particles are in what is known as crowded

environments where additives and multiple components influence the physics. Specifically, for perfume microcapsules used in complex formulations such as shampoo or body gel, the goal is to engineer the irreversible deposition of the capsules to human hair or skin, while also designing an effective shampoo that washes away dirt particles.[30] The study of how added surfactants and polymers influence microcapsule deposition would guide the development of consumer products with increased olfactory sensation.

1.1.2 Objective

The objective of this dissertation is twofold: (a) to understand and model superparamagnetic particle interactions and assembly in a rotating field and (b) to measure and deduce mechanisms of microcapsule interactions with a substrate as a function of additive concentrations.

For the former, experiments are conducted using a quadrupole set-up to directly visualize and quantify single particle interactions with the applied field, 2-particle (doublet) interactions with the field and with each other, and multiple particle interactions and assembly as a function of applied field amplitude and frequency. In parallel, high dimensional BD and SD simulations were developed to model the systems and study how certain parameters influence the behaviors quantitatively. Low-dimensional models were also generated that serve as accurate representations of the higher-dimensional dynamics. Trajectories of the 2 and multiple particle systems are analyzed to numerically calculate the steady state coefficients in their respective low-dimensional Fokker-Planck equations that describes the probability evolution of the systems. In turn, the Fokker-Planck equation can be used to find the effective pair interactions as well as effective energy landscapes in order parameter space.

The perfume microcapsules were provided by an industry collaborator and were fabricated by them to have a buckled or dimpled feature, rendering them anisotropic, meaning they have both a position and orientation dependent interaction with the glass surface. As such, a combination of Total Internal Reflection Microscopy, which only measures the distance dependence of interactions, and dynamical analyses were developed to determine when and how the microcapsules deposit onto the negatively charged glass surface as a function of sodium laureth sulfate (SLES) and the commercial polymer, Salcare SC60, concentrations.

1.2 Background

Rotating magnetic fields have been used in the literature to manipulate particle interactions and microstructures and there is some precedence for identifying and characterizing specific physics relevant to particle interactions in these systems. Developing both high dimensional and low dimensional simulations that accurately model experiments is also key to understanding rotating magnetic field systems. Previous experimental and modeling work with single particles, doublets and multiple particles is briefly reviewed, and the modeling techniques applied to study colloidal interactions is also summarized in the following section. A brief background on particle interactions in the presence of surfactants and polymers is also reviewed.

1.2.1 Particles in Rotating Magnetic Fields

In applied magnetic fields, magnetic particles orient their dipoles along the direction of the field and if there is a gradient, translate towards high field strengths. When the field is continuously rotating, the particles attempt to align their dipoles with the field via two distinct mechanisms depending on the properties of the magnetic material: Brownian

rotation[31] where the particle physically rotates in the fluid, or Néel relaxation[32] where the individual magnetic moments rotate internally. If the field rotates faster than the time scales of the relaxation, a phase lag between the particle dipole and the field develops.[33, 34] The two different types of micron-sized colloids that have been studied in the literature are isotropic polystyrene or silica particles[35-37] embedded with iron oxide nanoparticles and janus particles[38-40] that have a thin film magnetic surface coating[41] on one hemisphere. Both types of particles have been shown to experience a combination of Brownian and Néel relaxation.

In addition to particle-field interactions, two or more magnetic particles under an applied field interact with each other by aligning their dipoles and by translating towards each other due to the local increase in field strength.[42, 43] Thus, in a constant field, it is favorable for the particles to form chains. In a rotating field, the competition between the particle-field interaction and the particle-particle interactions can cause the chains to break up.[44] Depending on the frequency of the applied field, the chain break-up is caused by either the repulsive interaction between particles when the dipoles are not aligned, which occurs at intermediate frequencies or by time averaging of the interactions that results in a net isotropic attraction, which occurs at high field frequencies. [45-48]

Single particles, doublets, chains and condensed structures have all been studied in rotating magnetic fields with various degrees of rigor and modeling. In a couple studies, the magnetic properties and particle-field interactions of single particles were carefully quantified, and magnetic relaxation models that included Brownian and Néel relaxation were developed that accurately reflect the experimental observations.[35, 37] Simplified dynamic models and experiments have also been reported for doublets, showing at low

frequencies that doublets rotate at the same rate as the field, while at critical frequencies, the doublet rotation oscillates and the particles experience intermittent attraction and repulsion as the dipoles become misaligned.[49] However, a comprehensive model that connects single particle magnetic properties and rotation rates to doublet dynamics across a broad frequency range had been lacking in the literature.

Investigations of multiple particles in rotating magnetic fields have either reported experimental or simulation data, with only a few reporting both.[38, 50] The studies that do report simulations that agree with experiments only looked at limiting cases such as narrow frequency ranges[49] or very high field amplitudes.[38], or the simulations only reflect the behaviors at specific conditions.[25] In addition, while there have been studies of how magnetic particle chains break and fold[50-52] under the application of a rotating field, as well as studies of steady state microstructures and phase behaviors,[53-55] there have not been studies that comprehensively report both the assembly process dynamics and the condensed state behaviors as a function of various field conditions. Nonetheless, a key finding of the preceding literature is that multibody hydrodynamics have an impact on multiple particle systems. Specifically, experimental studies observed particle chain folding and rotation and concluded that these behaviors were due to asymmetric friction effects.[51, 56] In addition, a simulation study showed how hydrodynamics affects particle alignment and the condensation rate of magnetic janus particles in quasi-two-dimensional clusters. [57] Given the patchwork of literature on micron-sized particles in rotating fields, a systematic investigation of the key physics affecting interactions, assembly and microstructures across frequency and field amplitude would provide a more thorough understanding of the system in order to engineer and control colloidal assembly[58] and dynamics.

1.2.2 Modeling with Brownian and Stokesian Dynamics

The motion of Brownian particles in solution can be described by the Langevin equation, which is essentially a force balance that includes the stochastic and deterministic forces on the colloids where it is assumed that changes in particle position occur on a much slower time scale than momentum relaxation. The Langevin equation is reported in units of force, and after some integration and algebraic manipulation, an equation can be derived that characterizes particle position in time.[28] Application of this equation is called Brownian Dynamics (BD), and simulations can be implemented in one dimension or up to $6N$ dimensions, or three orientation coordinates and three positional coordinates in a system of N particles. The particles experience friction or resistance from the fluid, referred to as hydrodynamic interactions, which can be expressed as a constant in the case of a single particle moving in an unbounded medium.[59] Simplified BD simulations of bounded particles may also be modeled with a constant resistance coefficient, in the event that coordinate-dependent resistance does not significantly contribute to the key physics or behaviors of the system being studied.

More accurately, resistance terms of systems of multiple particles or particles diffusing close to a surface depend on particle positions with respect to other surfaces, and resistance is no longer a constant but a matrix. As a particle approaches another particle or a surface, the resistance increases, or conversely, the diffusivity (which is related to the inverse of the resistance) decreases. Additional effects also occur due to hydrodynamics: particle movement in one direction is transmitted through the fluid, affecting another particles' motion. Hydrodynamic interactions can be broken into far-field and near-field components, where the short-range (lubrication) only impacts the results as the surfaces come into near

contact. As a result, some BD simulations can accurately describe the dynamics of a real system by including either far-field[60, 61] or lubrication components,[62] while for some systems, both are important. In addition, in systems where particle rotation is not significant, BD simulations that only model position but not orientation accurately reproduce experimental results.[20]

Simulations that only include particle-particle or particle-surface hydrodynamic interactions are generally referred to as BD. However, in some cases, the hydrodynamic interactions are not pairwise additive, meaning multi-body effects significantly contribute to the dynamics of the system. Stokesian Dynamics (SD)[29] is a technique similar to BD in that the positions of the particles are numerically calculated in time, as derived from the Langevin equation. But SD includes far-field multi-body interactions as well as near-field lubrication forces, which by definition can be added pairwise. SD can be used to represent the exact hydrodynamic interactions between particles and surfaces, but the computation is expensive and therefore it is common in the literature to use various BD approximations rather than SD if the results do not significantly differ.[61, 63] However, as alluded to above, such approximations may not always be appropriate.

1.2.3 Dimensionality Reduction and Low Dimensional Langevin Dynamics

For colloidal assembly applications in a 2D plane, the coordinates of interest are often particle positions in x and y, which would mean the system has $2N$ dimensions. However, it is challenging to quantitatively describe and characterize a high-dimensional system. Therefore, order parameters, also known as reaction coordinates, are often used to characterize diverse problems such as protein folding,[64] micelle formation,[65] complex fluid viscoelasticity,[66] and particle clusters.[67] Machine learning techniques can even be applied

to determine the number of order parameters necessary to capture the main dynamic modes of high-dimensional systems,[68] but finding appropriate order parameters is still an area of research is in its infancy, and currently involves lengthy data mining and simulation iterations.[69]

Nonetheless, order parameters can be chosen with machine learning, intuition or both. For example, in colloidal assembly, particles go from a liquid to a solid state, and order along hexagonally closed-packed lattices, and thus order parameters can be chosen to reflect these two main behaviors[67, 70] In addition to succinctly describing high dimensional processes, order parameters can be used to model systems in 1-2 dimensions by constructing a low-dimensional Langevin equation. Analogous to BD/SD simulations that characterize particle position, a low-dimensional Langevin dynamics simulation describes how the order parameters evolve with time.[67, 70]

1.2.4 Particle-Surface Interactions with Additives

In aqueous solutions, particle-particle and particle-surface interactions can be modeled using Derjaguin, Landau, Verwey and Overbeek (DLVO) theory,[71, 72] which incorporates electrostatic and van der Waals interaction potentials. Key parameters that impact the interactions are the salt concentration, which narrows the range of electrostatics, zeta potentials of the surfaces, and the dielectric properties of the materials. When surfactants or polymers are added to the solution, additional interactions can occur, such as steric stabilization,[73] charge reversals, depletion attraction[23] or repulsion,[74] and tethering.[75] Depletion in particular is a common phenomenon in systems of unabsorbed additives,[76] and is due to osmotic pressure differences when the concentration of depletants (the additive) in the bulk is different than the concentration in the volume between the particle

and another surface.

At low depletant volume fractions, the interaction is attractive. Concentrated colloidal dispersions experience phase transitions with changing depletant concentration, and can go from a liquid to a crystal to an arrested gel state, depending on the strength of the interaction.[77] The size of the depletants and their concentration impacts the interaction well depth and range.[23]

Particle-surface interactions can be measured by Total Internal Reflection Microscopy (TIRM) by conducting a Boltzmann inversion on a histogram of sampled heights from a surface to obtain the interaction potential.[78] Other techniques reported in the literature include Atomic Force Microscopy (AFM)[79] and optical tweezers,[80] although for these latter techniques, weak depletion interactions cannot be accurately measured due to resolution limitations.[81]

1.3 Summary and Dissertation Outline

This dissertation is organized as follows: *Chapter 2* provides a theoretical foundation for the work in this thesis and specifically covers (i) colloid and surface interactions and (ii) the equations used to model stochastic systems. *Chapter 3* details the types of particles used, the experimental equipment, the procedures for sample preparation, microscopy and image analysis, and modeling parameters and protocols used in simulations for this dissertation. The main results of this thesis are presented in *Chapters 4-7*. These chapters represent individual papers that have or are in the process of being published. *Chapter 4* reports experimental data of single particle, single particle in a rotating doublet, and doublet rotation as well as particle separation dynamics for two field amplitudes and a broad frequency range. Brownian Dynamics is matched to the dynamics

observed in the experiments, and it is deduced that hydrodynamic coupling and the magnetic relaxation behaviors of the particles are the key phenomena influencing the observed results. *Chapter 5* applies the accurate simulation model developed in the previous chapter to implement many simulations and generate a large number of statistics and high-resolution particle-pair trajectories across several case field conditions as well as a broad frequency range for a particular field amplitude. The dimensionality is reduced to a single variable, the separation distance between two particles, to solve the one-dimensional Fokker-Planck equation for the effective pair potentials between particles in this nonequilibrium rotating magnetic field system. *Chapter 6* reports experimental and simulation results of multiple particle assembly from a chain to a condensed structure(s) as a function of field frequency and amplitude. Order parameters capture the main dynamic modes of the system, and a Fokker-Planck analysis depicts the energy and diffusivity landscapes in order parameter space. Low dimensional Langevin dynamics are conducted and show good agreement with both experiments and the high dimensional simulations. The results illustrate how colloidal assembly can be tuned by rotating magnetic field conditions and shows how coarse-graining techniques can provide useful information about nonequilibrium colloidal structures. *Chapter* 7 details results from TIRM measurements and trajectory characterizations of anisotropic fragrance microcapsules interacting with a surface as a function of either a surfactant or polymer additive. Mechanisms can be deduced by both the dynamic and equilibrium data and will inform future work of particle interactions in more complex solutions. *Chapter 8* summarizes the conclusions from these chapters. Finally, *Chapter 9* explains ongoing and future work related to colloidal assembly and fragrance microcapsules.

2. THEORY

2.1 Colloidal and Surface Interactions

2.1.1 Net Potential Energy Interactions

Colloidal particles experience surface forces from nearby particles or substrates, as well as interactions with external fields. Particles that are anisotropic, either due to shape or material properties, may have orientation as well as position dependent interaction potentials. The two types of particles used in this dissertation are magnetic particles, that have directional dipoles, and buckled microcapsules. Hence, in general the interactions depend on the direction of the dipole and the orientation of the buckled side of the capsule. The net interaction energy on a colloidal particle, labeled as particle 1, can be broke into interactions with the wall, fields, and with *j* neighboring particles as,

$$u_1^{net}\left(\theta_1,\theta_j,\phi_1,\phi_j,\mathbf{r},z\right)=u^{pw}(\theta_1,\phi_1,z)+u^{pf}\left(\theta_1,\phi_1,z\right)+u^{pp}\left(\theta_1,\theta_j,\phi_1,\phi_j,\mathbf{r}\right) \quad (2.1)$$

where θ and ϕ are the azimuthal and polar angles of a particles' director vector, **r** is the center-to-center vector between particles, and *z* is the particle position along the *z*-axis where it is assumed a nearby wall is in the *x*-*y* plane. The distance *h* between the surface of the particle and a wall would be *z*-*a* where *a* is the particle radius. Particle-wall and particle-particle interactions would include electrostatics and van der Waals from DLVO theory. With the addition of small molecules, steric interactions, depletion, or tethering would also contribute to these interactions. In a magnetic field, the particles experience dipole-dipole interactions as well as particle-field interactions. In the absence of a magnetic field, the only field interaction is gravity.

2.1.2 Gravitational Interaction

A particle in a fluid experiences a gravitational potential when the density of the

particle is different than that of the fluid. Particles that are denser than water sediment, while those that are less dense than water cream. The magnetic particles are less dense while the perfume microcapsules are denser, but the gravitational energy is expressed in the same form as,

$$u_g(h) = (4/3)\pi a^3(\rho_p - \rho_f)gh \tag{2.2}$$

where a is particle radius, ρ_p and ρ_f are the particle and fluid densities and g is the acceleration due to gravity.

2.1.3 Electrostatic Interactions

The surface groups of particles or a substrate submerged in a fluid interact with electrolyte ions in the fluid, which induces a local high-density region of counterions to balance the surface charges. The counterion concentration exponentially decays away from the surface, characterized by a Poisson-Boltzmann equation.[82] The distance at which the ion concentration plateaus is known as the Debye length. When two charged surfaces come into close contact, a repulsive pressure builds up between the surfaces as a result of the high concentration of counterions in the volume between them, relative to the bulk. This effect is hereafter referred to as electrostatic repulsion.[72] In systems where a spherical particle of radius a interacts with a surface that has the same zeta potential or surface charge, the electrostatic repulsion can be expressed as,

$$u_E(h) = B\exp(-\kappa h) \tag{2.3}$$

$$B = 64\pi\varepsilon a\left(\frac{k_B T}{e}\right)^2 \tanh\left(\frac{e\Psi_p}{4kT}\right)\tanh\left(\frac{e\Psi_w}{4kT}\right) \tag{2.4}$$

where the Debye length is κ^{-1} and is found by the following equation,

$$\kappa = \left(\frac{2CN_A e^2}{\varepsilon k_B T} \right)^{0.5} \tag{2.5}$$

where ε is the solvent dielectric constant, e is the elemental charge, Ψ_p and Ψ_w are the particle and wall surface potentials, C is the bulk ion concentration and N_A is Avogadro's number. For particle-particle interactions, B (eq. (2.4)) is reduced by a factor of 2.

2.1.4 Van der Waals Interactions

All atoms and molecules interact via van der Waals forces, or instantaneous dipoles that create a temporary polarization in nearby surfaces, leading to a net overall attraction for similar surfaces (or repulsion in some cases for dissimilar surfaces) that decays at a rate of r^{-6}.[83] The interaction depends on the dielectric properties of two nearby surfaces, as well as the properties of the medium. Hamaker derived an expression for van der Waals interactions that assumes atom-atom interactions can be superimposed, although a more vigorous derivation was later conducted by Lifshitz.[84] In this thesis, the van der Waals interactions are not directly measured, but an understanding of the range of van der Waals and their contribution to irreversible interactions is important for studying colloidal stability. Thus, we are satisfied with an approximation for van der Waals interactions,[85]

$$\begin{aligned} u_V^{pw}(h) &= -a2A\left[h + \delta_V\right]^{-p} \\ u_V^{pp}(r) &= -aA\left[r - 2a + \delta_V\right]^{-p} \end{aligned} \tag{2.6}$$

where A is Hamaker's constant, p can be fit to experimental data, and δ_V is a weakening term to account for surface roughness.

2.1.5 Magnetic Field Interactions

Magnetic particles can be described by their magnetic moment, **m**, or dipole moment that is the first term in the particle's multipolar expansion. The magnetic moment interacts with an external field, **H**, as[86]

$$u_{df}^{pf}\left(\theta,\phi\right) = -\mathbf{m}\cdot\mathbf{H} \tag{2.7}$$

As can be seen from this equation, the interaction goes to zero if the magnetic moment is aligned with an external field. And since force is the gradient of a scalar potential, the force on the particle would only be nonzero if **H** is position-dependent.

2.1.6 Magnetic Particle-Particle Interactions

Magnetic forces between particles are most accurately characterized by multipolar interactions. To solve for the exact interaction between two magnetic particles, some version of finite element analysis can be used to first calculate the distribution of a magnetic field in a defined three-dimensional box via Laplace's equation, and then calculating the magnetic force on a particle in that box with another particle using the Maxwell stress tensor.[87] Such a calculation can be conducted using in-house codes or using a software package like COMSOL Multiphysics. Alternatively, the interactions between magnetic particles can be approximated by the point-dipole interaction, which is

$$u_{dd}^{pp}\left(\mathbf{m}_1,\mathbf{m}_2,\mathbf{r}\right) = \frac{\mu_o}{4\pi r^3}\left[\mathbf{m}_1\cdot\mathbf{m}_2 - 3\left(\mathbf{m}_1\cdot\hat{\mathbf{r}}\right)\left(\mathbf{m}_2\cdot\hat{\mathbf{r}}\right)\right] \tag{2.8}$$

where μ_o is the magnetic permeability of free space.

2.1.7 Depletion Interaction

The depletion interaction is essentially created by an osmotic pressure difference between a small volume and the bulk fluid. Therefore, it depends on the geometry of the system, the size of the additives (depletants) with respect to larger colloids, and the

concentration of depletants. The original theory for depletion was derived by Asakura and Oosawa, and assumes that the concentration of depletants is zero in the volume between two surfaces if their surface-to-surface distance is less than the diameter of the depletant.[88] Since this original publication, the depletion potential has been modified to characterize "soft" depletants that can deform and fit into the excluded volume.[23] In addition, when the concentration of depletants is above approximately 10% volume, packing effects can lead to oscillatory osmotic pressure differences in regions between two surfaces, creating a potential energy barrier or depletion repulsion as a kinetic effect.[89, 90] In low depletant solutions, the interaction can be expressed as,

$$u_D(h) = \begin{cases} -\Delta\Pi V_{EV}(h) & h \le L \\ 0 & h > L \end{cases} \tag{2.9}$$

where $\Delta\Pi$ is the osmotic pressure difference, V_{EV} is the excluded volume region and L is the diameter of the depletant. At higher concentrations, more complicated calculations of the distribution profile of the additives is required. A general expression for the interaction in this case is,

$$u_D(h) = -k_B T\left[\Gamma(h) - \Gamma(\infty)\right] \tag{2.10}$$

where Γ is a function that depends on the radial distribution function of the depletant from a surface, and can be calculated by equation of state models for the depletant.[91] For particle-particle interactions, the above two depletant equations would be dependent on r instead of h.

2.1.8 Macromolecular Interactions

Colloidal particles in macromolecular solutions may experience a depletion attraction

if the molecules do not adsorb onto the particle surfaces. However, if adsorption occurs and a "brush" polymer layer forms on colloidal surfaces, this would create a steric repulsive barrier that would prevent the particles from nearing contact with other surfaces, such that the particles would not experience van der Waals attraction and would be stable.[73] In addition, polymers can form bridges between surfaces, causing tethering and deposition.[75]

Steric repulsion between a particle and a surface, both with identical brush layers, is

$$u_S(h) = 16\pi a f_0 \delta_0 \left(\frac{\Gamma}{\gamma}\right) \exp\left(\frac{-h\gamma}{2\delta_0}\right) \tag{2.11}$$

where f_0 and δ_0 are the free energy and thickness of the uncompressed brush, and Γ and γ are dimensionless constants used to fit unique brush architectures with varying density profiles normal to the surface.

Tethering can be modeled like a spring as,

$$u_T(h) = \frac{3Nk_BT}{4PL_T} h^2 \tag{2.12}$$

2.2 Equation of Motion and Dynamic Modeling

2.2.1 Langevin Equation

A particle in a fluid experiences a viscous drag force that acts as a resistance to motion. Particles that are on the order of nano- to micrometers also move randomly due to collisions with the fluid molecules, called Brownian motion, proved by Albert Einstein in 1905.[92] These affects can be modeled in an equation of motion that describes deterministic forces on the particles as well as stochastic forces. This equation is called the Langevin equation, and a general form is,[93]

$$\cdot \qquad (t) \tag{2.13}$$

where v is velocity, γ is friction and $\Gamma(t)$ is the stochastic force. The stochastic force has a mean zero and a variance that is proportional to the friction as,

$$\begin{aligned} &\langle \Gamma(t) \rangle = 0 \\ &\langle \Gamma(t)\Gamma(t') \rangle = q\delta(t-t') \\ &q = 2\gamma k_B T / m \end{aligned} \tag{2.14}$$

where $\delta(t-t')$ is the delta function and m is the particle mass. The above equations can be extended to multi-dimensional systems where the velocity and forces are vectors and the friction term is a matrix.

2.2.2 Fokker-Planck Equation

The Langevin equation is a type of coarse-graining that simplifies all of the microscopic interactions between molecules and approximates them using the random force term. Equivalently, a stochastic system can also be macroscopically characterized by a position probability distribution as a function of time, or its Fokker-Planck (FP) equation.[93] The Fokker-Planck equation can be thought of as a mass balance and a form of a master equation, and the general equation is,

$$\frac{\partial P}{\partial t} = \left[\frac{-\partial v\ (x)}{\partial x} + \frac{\partial^2 D(x)}{\partial x^2} \right] P \tag{2.15}$$

where P is the probability distribution of position variable x, v is drift and D is diffusion. Drift and diffusion are related to the first and second moments of the probability distribution. In equilibrium systems with large friction constants, it is assumed that

conservative forces are directly related to drift. Under this assumption, the Smoluchowski equation can be derived, which is a special form of the FP equation,

$$\frac{\partial P}{\partial t} = \frac{1}{m\gamma}\left[\frac{-\partial F(x)}{\partial x} + k_B T \frac{\partial^2}{\partial x^2}\right] P \tag{2.16}$$

where $F(x)$ is the gradient of a scalar potential, and the diffusion has been re-written in terms of friction and the Boltzmann constant.

2.2.3 Brownian and Stokesian Dynamics

Finding a solution to the Langevin equation and corresponding Fokker-Planck equation can be challenging, and thus numerical simulations are often employed to model dynamic systems. A technique known as Brownian Dynamics[28, 94] has been developed to calculate particle positions in time. The positions and orientations (if relevant), are derived from a multi-dimensional Langevin equation as

$$\mathbf{r}_l = \mathbf{r}_l^0 + \sum_j \frac{\partial \mathbf{D}_{lj}^0}{d\mathbf{r}_j}\Delta t + \sum_{j,j\le 3N} \frac{\mathbf{D}_{lj}^0(\mathbf{F}_j^{P,0} + \mathbf{F}_j^B)}{k_B T}\Delta t + \sum_{j,j>3N} \frac{\mathbf{D}_{lj}^0(\mathbf{T}_j^{P,0} + \mathbf{T}_j^B)}{k_B T}\Delta t \tag{2.17}$$

$$\mathbf{n}_l(t+\Delta t) = \mathbf{n}_l(t) + \left[\left(\sum_{j,j>3N} \frac{\mathbf{D}_{lj}^0}{kT}\left(\mathbf{T}_j^{P,0} + \mathbf{T}_j^B\right) + \sum_{j,j\le 3N} \frac{\mathbf{D}_{lj}^0}{kT}\left(\mathbf{F}_j^{P,0} + \mathbf{F}_j^B\right)\right)\right] \times \mathbf{n}_l(t)\Delta t \tag{2.18}$$

where **r** is the position vector of all particles, **D** is the diffusivity matrix, *F* and *T* are forces, and **n** is the unit orientation vector. This representation contains *6N* dimensions, where the first *3N* are position and the latter are orientation. Superscripts indicate the forces and torques are from scalar potentials (*P)* or Brownian forces (*B).*

2.2.4 Hydrodynamic Interactions and Stochastic Forces

The friction forces on particles are collectively called hydrodynamic interactions. As

described in the definition of the Langevin equation, random forces are correlated to friction, which is a result of the fluctuation-dissipation theorem.[95] Therefore, if the hydrodynamics are known, the stochastic forces are also known and vice versa. The random torques and forces can be combined into one equation, which is related to the diffusivity as shown

$$\mathbf{S}^B = \begin{pmatrix} \mathbf{F}^B \\ \mathbf{T}^B \end{pmatrix} \tag{2.19}$$

$$\left\langle \mathbf{S}_i^B(0)\mathbf{S}_j^B(t) \right\rangle = 2(kT)^2 \mathbf{D}_{ij}^{-1}\delta(t) \tag{2.20}$$

The diffusion coefficient for one particle in an unbounded medium is called the Stoke-Einstein diffusion coefficient, D_0, and is expressed as

$$D_0 = \frac{k_B T}{6\pi\eta a} \tag{2.21}$$

where the denominator is the friction coefficient or resistance and η is the viscosity of the fluid. If additional particles or a wall is added, the diffusivity can no longer be expressed as a constant. In Brownian dynamics, the diffusivity tensor includes pair-wise interactions between particles[96] and surfaces[97, 98] and the diffusion is dependent upon the distances between surfaces. Stokesian Dynamics is an extension of Brownian Dynamics in that it includes multi-body hydrodynamics.

3. METHODS

3.1 Materials and Equipment

3.1.1. Particles, Wall surfaces, and Additives

In the magnetic particle experiments, Dynabeads™ M-270 Carboxylic Acid with an

approximate diameter of 2.8um were used (ThermoFisher Scientific). The fragrance microcapsules studied in the latter part of the thesis were anionic spherical capsules, [30] and anionic buckled capsules[99] as provided by Firmenich, Inc. The microcapsules are polydisperse in size, with diameters of ~10-20μm. All experiments were conducted on either glass slides (Fisher Scientific) or coverslips (Gold Seal, Corning). In the microcapsule experiments, sodium laureth sulfate (Texapon N70, BASF) and Salcare SC6 (Acrylamidopropyltrimonium Chloride/Acrylamide Copolymer, BASF) were acquired from Firmenich, Inc.

3.1.2. Slide and coverslip cleaning

Since particle-surface interactions are extremely sensitive to the surface groups or dust particles on glass slides or coverslips, a rigorous cleaning procedure was employed for all experiments. First, the slides are sonicated in Acetone and then Isopropanol for 30 minutes each to clean off oil residues. Then, the slides are rinsed 10x with deionized (DI) water, and dried with nitrogen gas. The slides are soaked in Nochromix (Godax Laboratories), which is a strong acid solution used for cleaning glassware, for 1-24 hours. Finally, the slides are sonicated in a 1M KOH solution to negatively charge the surfaces, and then rinsed in DI water and dried again with nitrogen gas.

3.1.3. Fabricating magnetic "optical janus" particles

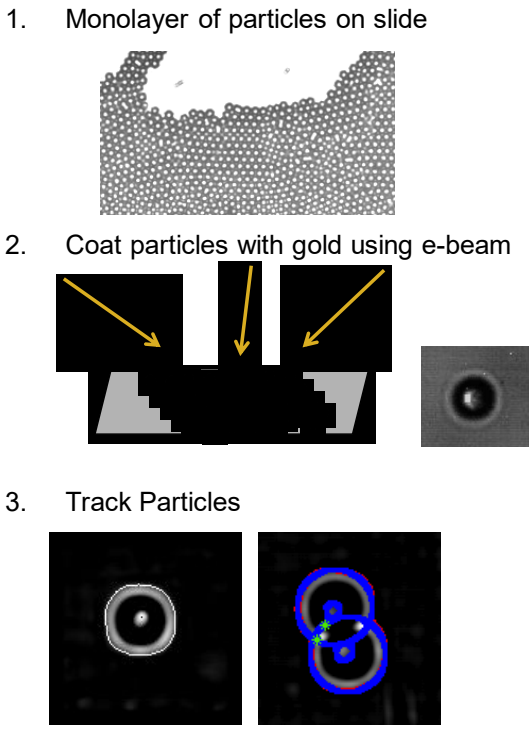

Figure 3.1: Fabricating Optical Janus Particles to Track Particle Rotation. The particles are dried as a monolayer on a glass slide, and then are placed in an E-beam evaporator so that only one side of the particles is coated. Then, the particles can be tracked using image analysis codes.

To visualize the magnetic particle rotation, the Dynabeads were coated on one side with a nonmagnetic metal to render them optically anisotropic. First, the particles were dried onto a glass slide. Then, a layer of Cr, then Au, then SiO2 were electrodeposited onto the sample using an E-beam evaporator in a clean room, such that only the exposed side of the particles (not attached to the slide) were coated. The slides with the dried particles were then submerged in water and sonicated to release the particles from the slide, and then the samples were centrifuged to collect the particles. Figure 3.1 summarizes the steps to making the optical janus particles.

3.1.4. Sample cell preparation

For the experiments, particles were diluted in solution of various salt and additive concentrations. To make the solutions, a 2mL plastic centrifuge tube was rinsed 5x in DI

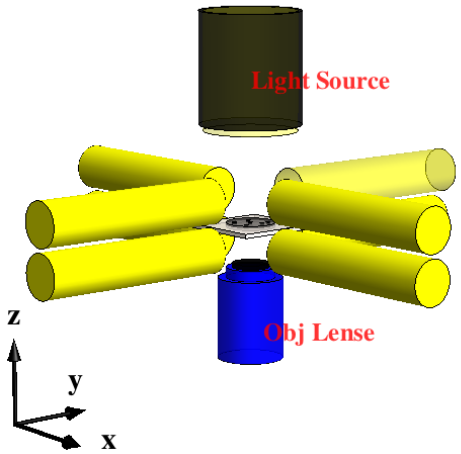

Figure 3.2: Schematic of the Magnetic Quadrupole Set-up. Two sets of four solenoids each are arranged above an objective lens. The coverslip with the particle solution contained in an o-ring is placed on a stage (not shown) in the middle of the quadrupole set-up.

water and dried overnight, and then solutions of 1.8mL were made. For experiments that required dilute particle concentrations (1-5 particles in the field of view), approximately 1µl of stock particle solution was pipetted into the 1.8mL aqueous solution. For more concentrated experiments, approximately 3µl of the Dynabead stock was used and 6µl of the PDA and PGA solutions were used. Immediately after the slide and coverslip cleaning procedure, a Viton o-ring (McMaster Carr) was attached to the center of the slides using vacuum grease and epoxy (Loctite). Then, 100µl of the particle solution (for the 10mm o-ring) was pipetted into the o-ring, and the sample was sealed with a coverslip and more epoxy. For the microcapsule experiments, the epoxy is allowed to dry for 1-5 minutes, and then the samples are flipped over to allow the particles to interact with the clean slide rather than the coverslip.

3.1.5. Magnetic quadrupole

The rotating magnetic field is generated by eight solenoids positioned in a quadrupole arrangement where two sets of four solenoids are stacked on top of each other, as shown in Figure 3.2. The set-up was built and calibrated by Dr. Clayton LaPointe.[100, 101]

The applied current is controlled by a computer LabView interface, where sinusoidal functions control the currents sent to pairs of solenoids to create a uniform field that rotates in the *x*-*y* plane. Due to the stacking of the solenoids in the *z*-axis, constant and rotating fields can also be applied in all three dimensions. Periodically, the set-up needs to be re-calibrated, where current is matched to gauss meter readings via a linear function with adjustable slope and intercept.

3.2 Microscopy and Particle Tracking

3.2.1 Inverse Total Internal Reflection Microscopy

In order to conduct Total Internal Reflection Micrscopy (TIRM) measurements on particles less dense than water, a laser was aligned with an adjustable mirror so that the beam hits the top of a glass prism at a 90º angle (see Fig. 3.3). In this set-up, the prism is placed on top of the slide, rather than the reverse.

The intensity of the particle scattering is related to its distance from the glass surface by,[78]

$$I\left(h\right) = I_0 \exp\left(-\beta h\right) \tag{3.1}$$

Thus from equilibrium scattering data, a histogram of heights can be developed, from which interaction potentials are derived via the Boltzmann equation,

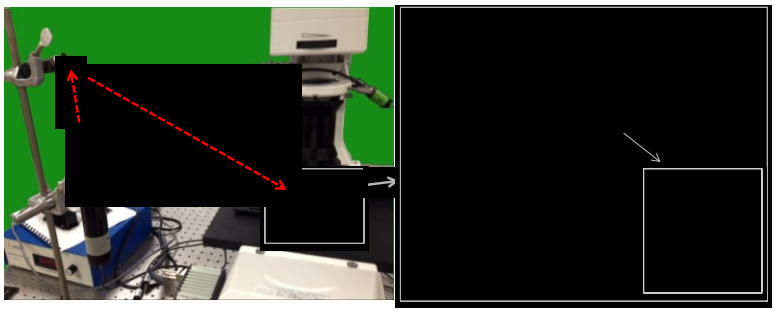

Figure 3.3: Image and schematic of the Inverse Total Internal Reflection Microscopy (TIRM) set-up. A laser is mounted to the air table, and a mirror is oriented such that the laser is directed to hit the side of the prism at a 90º angle. The prism is placed on top of the glass slide. On the slide, an aqueous solution is contained in a black o-ring and coverslip. An evanescent wave is created at the glass-water interface, the intensity of which scales exponentially with distance from the interface. As such, the particles interacting with the top surface of the slide scatter light that can be directly related to the distance of the particle from the glass surface. Videos are taken that record the intensity of this scattering, to build a histogram of relative heights. The probability of relative heights can be used to calculate the interaction potential between the particle and the glass slide via the Boltzmann equation.

$$p(h) = A\exp\left[-\frac{u(h)}{k_B T}\right] \tag{3.2}$$

3.2.2 Video Microscopy and Particle Tracking

Particle interactions, rotation and assembly were captured in the quadrupole set-up by recording videos using Photron Fastcam, which captures video at 60 frames per second (fps). Then, the trajectories of the particles (specifically isotropic, non-optical janus particles) were tracked using FORTRAN codes based on the strategy introduced by Crocker and Grier.[102]

3.2.3 Tracking Optical Janus Particles

The orientations of the optical janus particles were tracked using home-built codes in MATLAB. Specifically, the *bwboundaries* function identifies the outline of the particles and the bright patch due to the gold surface layer. The position of the bright patch with respect to the center of the particle (calculated by averaging the particle outline pixels) thus gives the orientation of the particle. As the position of the bright patch changes throughout

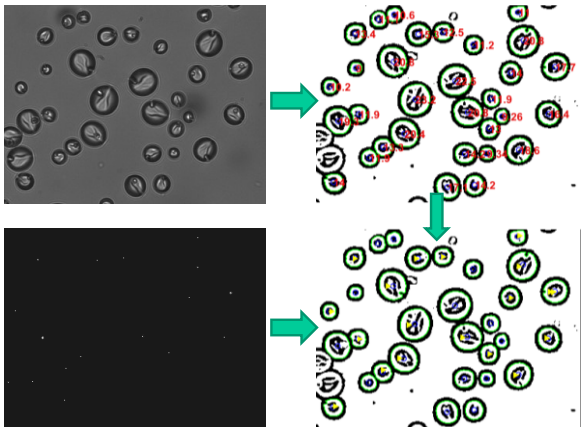

Figure 3.4: Sizing Polydisperse Microcapsules: To test whether particle size impacts the association to the surface and the particle-wall interaction, we have developed a particle tracking code in MATLAB that sizes the particles, then matches the particles that were sized to the TIRM tracking. The code works as follows: (1) Application of a band pass filter to increase contrast. (2) Apply the Matlab function *bwboundaries* to obtain the outlines (large green circles) of the particles. The radii of the particles that can be tracked are approximated by finding the center of the outlined shape (small blue circles), and then calculating the average distance from the center to all of the outline (green) pixels. Measured diameters are shown in red text. (3) The particle tracking that was done from the TIRM experiments gives a bright spot that is to the left of the real particle center (bottom left image – note that this particular slice of the video does not track all of the particles, but in the algorithm, particle coordinates are averaged over the whole video length and more are tracked than is shown in this slice). These coordinates were shifted, and then matched to the previously tracked particle centers (blue circles). All of the particles that can be matched are marked with a yellow triangle.

the video, the rotation rate of the particle in the 2-dimensional plane can be determined.

3.2.4 Sizing polydisperse microcapsule images

In a similar manner to tracking the optical janus particles, light microscopy images of the microcapsules were analyzed using the *bwboundaries* function to obtain the outline pixels of the particles. Then, the size of the particles is determined by calculating the center, and then the radius is the average distance from the center to the outline pixels. The particles that are tracked in this manner are then matched to the TIRM particle tracking videos to obtain the sizes of the unique particles and correlate the TIRM trajectory data to the static light microscopy images. Figure 3.4 summarizes how these particles were sized.

3.3 Brownian and Stokesian Dynamics

Brownian and Stokesian Dynamics simulations were implemented following eq. (2.17) -(2.18) with a numerical integration fime of 0.01ms, which is slower than momentum relaxation. The midpoint scheme[103] was applied in all simulations to avoid calculating the gradient of the diffusion tensor. For most of the simulations, the particle initial positions were in a doublet or chain along the *x*-axis and the dipole orientation was parallel to the *x*-axis. The field orientation also started parallel to the *x*-axis.

4. ROTATING COLLOIDS IN ROTATING MAGNETIC FIELDS: DIPOLAR RELAXATION & HYDRODYNAMIC COUPLING*

Video microscopy (VM) experiments and Brownian Dynamics (BD) simulations were used to measure and model superparamagnetic colloidal particles in rotating magnetic fields for interaction energies on the order of the thermal energy, kT. Results from experiments and simulations were compared for isolated particle rotation, particle rotation within doublets, doublet rotation, and separation within doublets vs. field rotation frequency. Agreement between VM and BD results was obtained at all frequencies and amplitudes only by including exact two-body hydrodynamic interactions and relevant relaxation times of magnetic dipoles. Frequency dependent particle forces and torques cause doublets to rotate at low frequencies via dipolar interactions and at high frequencies via hydrodynamic translation-rotation coupling. By matching measurements and simulations for a range of conditions, our findings unambiguously demonstrate the quantitative forms of dipolar and hydrodynamic interactions necessary to capture non-equilibrium, steady state dynamics of Brownian colloids in magnetic fields.

4.1 Introduction

---

* Published as A. C. H. Coughlan and M. A. Bevan, Physical Review E **94** (4), 042613 (2016). Permission to include in thesis granted from the American Physical Society, License number 4146040818834.

The dynamics of magnetic colloidal particles in time-dependent magnetic fields are relevant to many applications such as measuring biomolecular interactions,[104, 105] developing microfluidic devices,[106, 107] tuning magnetorheological suspensions,[108] and increasingly, colloidal assembly.[25, 55, 109-111] For example, magnetic dipolar colloidal chains can be used to tune suspension rheological properties by forming, bending, breaking, translating, and rotating in dynamic fields. [46, 50, 112, 113] Microstructures of dipolar colloidal particles can be manipulated in external fields to form chains, clusters, crystals, and many other configurations.[21, 47, 114] Controlling colloidal interactions in rotating fields is becoming a promising approach to manipulate two-dimensional colloidal assembly[25, 55, 109, 110] as well as three-dimensional microstructures.[21] Rotating fields, when combined with field gradients, can also transport, disperse, and order colloidal particles.[115]

In applications involving magnetic colloids, it is important to understand how single dipoles interact with dynamic magnetic fields in balance with hydrodynamic drag. Superparamagnetic micron-sized particles have induced dipoles that display a range of relaxation times based on the ensemble response of individual magnetic domains (due to many magnetic nanoparticles dispersed within each micron sized colloidal particle). Practically, for a given field frequency, a separation of relaxation times allows net dipoles to be considered as the sum of two contributions: (1) Néel dipoles that appear to be instantaneous as a result of their relatively fast relaxation via stochastic reorientation within magnetic domains, and (2) Brownian dipoles that appear to be permanent as a result of their slow relaxation relative to the stochastic rotation of the colloidal particle.[35, 37] Both of these dipoles contribute to frequency-dependent dipole-field torques in rotating fields

while viscous forces oppose rotation. Previous work has shown the fast Néel relaxation dominates the ensemble dipole.[36]

In addition to single particle interactions, two (or more) particles have been shown to rotate in response to external fields due to particle-particle interactions, including dipole-dipole and hydrodynamic interactions. Dipole-dipole interactions lead to torques on particle doublets (or chains) due to the favorable head-to-tail alignment of dipoles.[25, 49, 116, 117] Particle-particle interactions also determine whether doublets rotate as rigid bodies or as free rotating particles. For doublets to rotate rigidly, a tangential force between two particles is required (which has been used to study macromolecular and electrostatic interactions[118, 119]). Rigidly rotating doublets rotate slower than doublets in which the particles can freely rotate. These results suggest that the dynamics of individual particles within doublets, as well as particle-particle interactions, are crucial to understanding doublet rotation (and vice versa).

Previous research suggests that hydrodynamic interactions and dipole relaxation both affect the frequency dependence of magnetic doublet rotation in rotating fields. It has been observed that doublets rotate at the same frequency as rotating fields up to a critical frequency, after which the rotation rate declines due to viscous drag.[25, 48, 49, 120] These studies showed at frequencies slightly higher than the critical frequency: (1) individual dipoles no longer remain aligned along the line of centers, (2) for freely rotating doublets, the interparticle distance oscillates, and (3) for both rigid and freely rotating doublets, the angular trajectories oscillate about an average steady rotational velocity. At even higher frequencies, where Brownian relaxation cannot occur, larger clusters[55, 56] and rigid doublets[121] continue to rotate, which has been suggested to occur via the balance of an out-

of-phase dipole and hydrodynamic interactions. Although prior modeling studies of small chains and clusters have considered various aspects relevant to rotating doublets in rotating fields (including hydrodynamic interactions,[46, 50, 112, 113] translation-rotation coupling[57], and non-trivial Néel relaxation[56, 121]), none have included thermal motion, exact hydrodynamics, and dipolar relaxation necessary to quantify both single particles and doublet rotation and relative particle translation vs. frequency.

In this work, we investigate superparamagnetic particles in rotating magnetic fields including single particle rotation, doublet rotation, single particle rotation within rotating doublets, and relative particle translation within doublets (see Fig. 4.1). VM is used to measure the translation and rotation of particles vs. field rotation frequency for small field amplitudes that allow for thermal motion to probe kT-scale interactions. Each experiment is simulated using BD simulations that include conservative forces and torques (i.e., the gradients of scalar potential functions), non-conservative forces and torques (i.e., exact pair hydrodynamic interactions between particles including translation-rotation coupling and

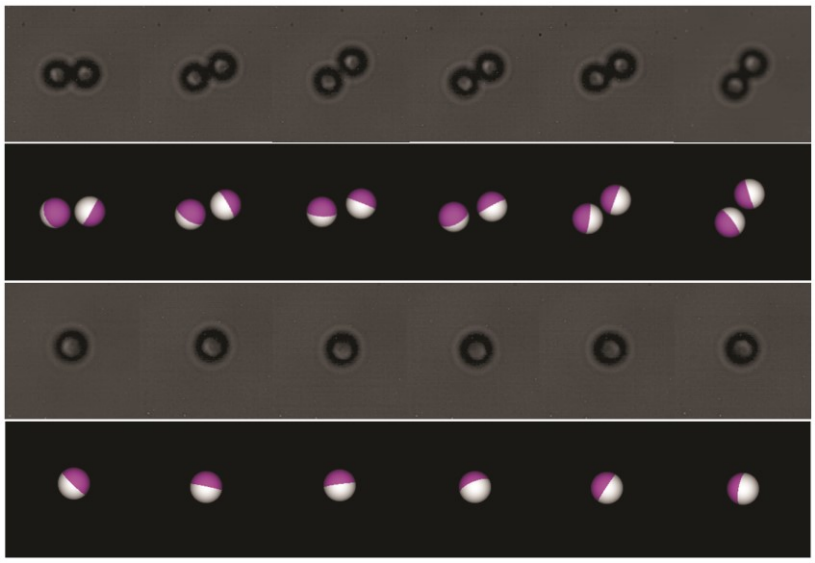

FIG. 4.1. Single particle and doublet rotation in experimental images and BD simulation renderings (6 Gauss, 0.8 Hz; image time step of 0.167s) (see Videos S1-S3 in the *Supplemental Material* (SM)[1]).

near-field and far-field[122]), Brownian motion, and the effects of a distribution of relaxation times. To increase model complexity in a systematic fashion, we first match simulations and experiments for single particles by determining their dipole moments and their relaxation vs. field rotation frequency. We then measure and model all rotational and translational modes in doublets vs. field frequency. This process provides a unique rigorous model that qualitatively and in most cases quantitatively captures all frequency dependent interactions and dynamics of superparamagnetic Brownian colloids in rotating magnetic fields.

4.2 Theory

4.2.1 Equation of Motion

The translational and rotational motion of a particle with mass m can be expressed by the Langevin equation as (for coordinates labeled in Fig. 4.2) [94],

$$m\frac{d\mathbf{u}}{dt} = \mathbf{F}^P + \mathbf{F}^H + \mathbf{F}^B \tag{4.1}$$

$$m\frac{d\boldsymbol{\omega}}{dt} = \mathbf{T}^P + \mathbf{T}^H + \mathbf{T}^B \tag{4.2}$$

where $\mathbf{u}$ and $\boldsymbol{\omega}$ are translational and angular velocity vectors, and $\mathbf{F}$ and $\mathbf{T}$ are force and torque vectors. Superscripts in Eqs. (4.1) and (4.2) denote contributions from: *P,* conservative forces on particles due to the gradient of a scalar potential field, *H,* non-conservative forces due to hydrodynamic interactions that couple translation and rotation between particles, and *B*, random thermal forces and torques due to Brownian motion.

Particle position vs. time is modeled by solving the Langevin equation for position. A new position $\mathbf{r}_l$ where l coordinates correspond to translation only (*i.e.*, $l \le 3N$), is calculated as,

$$\mathbf{r}_l = \mathbf{r}_l^0 + \sum_j \frac{\partial \mathbf{D}_{lj}^0}{d\mathbf{r}_j}\Delta t + \sum_{j,j\le 3N} \frac{\mathbf{D}_{lj}^0(\mathbf{F}_j^{P,0} + \mathbf{F}_j^B)}{kT}\Delta t + \sum_{j,j>3N} \frac{\mathbf{D}_{lj}^0(\mathbf{T}_j^{P,0} + \mathbf{T}_j^B)}{kT}\Delta t \tag{4.3}$$

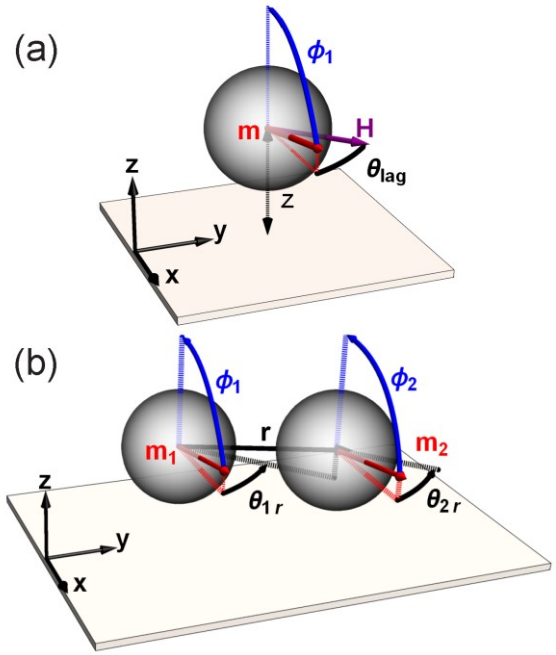

FIG. 4.2. Schematics showing (a) a dipole **m**, defined in Eq. (4.20), and its phase lag in the x-y plane with respect to a field **H**, which produces a torque on the particle as expressed in Eq. (4.37), and (b) the relevant angles and vectors of a doublet system, including dipole polar and azimuthal angles with respect to the particle-particle vector **r** in the x-y plane, used in the dipole-dipole potential, Eq. (4.16)(note k has been dropped to generalize the schematic).

where, $\mathbf{F}_j^{P,0}$ and $\mathbf{T}_j^{P,0}$ $\mathrm{T}_j^{P,0}$ are the force and torque vectors at the start of each step, and $\mathbf{F}_j^B$ and $\mathbf{T}_j^B$ are the random force and torque vectors. Brownian Dynamics of the angular displacement of a particle has been derived in a similar manner [94]. The orientation of the particle main axis is calculated from unit vector $\mathbf{n}$ whose displacement is related to the conservative forces and torques as [123],

$$\mathbf{n}_l\left(t+\Delta t\right)=\mathbf{n}_l\left(t\right)+\left[\left(\sum_{j,j>3N}\frac{\mathbf{D}_{lj}^0}{kT}\left(\mathbf{T}_j^{P,0}+\mathbf{T}_j^B\right)+\sum_{j,j\le 3N}\frac{\mathbf{D}_{lj}^0}{kT}\left(\mathbf{F}_j^{P,0}+\mathbf{F}_j^B\right)\right)\right]\times\mathbf{n}_l\left(t\right)\Delta t \qquad (4.4)$$

where l coordinates correspond to rotation only i.e. $l>3N$.

4.2.2 Conservative Forces and Torques

A colloidal particle experiences a net potential energy that includes particle-wall, particle-field, and particle-particle interactions with a nearby particle. The dipoles are distinguished using an index, k, where $k=N, B$ for Néel, and Brownian as shown,

$$u^{net}\left(\theta_{1,k},\theta_{2,k},\phi_{1,k},\phi_{2,k},\mathbf{r},z\right)=u^{pw}(z)+u^{pf}\left(\theta_{1,k},\phi_{1,k},z\right)+u^{pp}\left(\theta_{1,k},\theta_{2,k},\phi_{1,k},\phi_{2,k},\mathbf{r}\right)$$

(4.5)

where $\theta_{l,k}$ and $\phi_{l,k}$ are the azimuthal and polar angles of the *l* particle-centered dipole moment, $\mathbf{r}$ is the 1-2 center-to-center distance and *z* is the particle center-to-wall-surface position. Three-dimensional force and torque vectors can be derived from Eq. (4.5) by taking partial derivatives with respect to a position or angle, keeping all other variables constant. For example, the force along the $\mathbf{r}$ direction and the torque in $\theta_{l,k}$ are given by,

$$\mathbf{F}_r^{\ P}=-\frac{\partial}{\partial r}u^{net}\left(\theta_{1,k},\theta_{2,k},\phi_{1,k},\phi_{2,k},\mathbf{r},z\right) \tag{4.6}$$

$$\mathbf{T}_{\theta_{1,k}}^{\ P}=-\frac{\partial}{\partial \theta_{1,k}}u^{net}\left(\theta_{1,k},\theta_{2,k},\phi_{1,k},\phi_{2,k},\mathbf{r},z\right) \tag{4.7}$$

4.2.3 Particle-Wall Potential

The only interaction with the particle and the wall is electrostatics [124], given by,

$$u_{el}^{pw}\left(z\right)=B^{pw}\exp\left[-\kappa\left(z-a\right)\right] \tag{4.8}$$

$$B^{pw}=64\pi\varepsilon\varepsilon_0 a\left(\frac{k_BT}{ze}\right)\tanh\left(\frac{z_v e\varsigma_p}{4k_BT}\right)\tanh\left(\frac{z_v e\varsigma_w}{4k_BT}\right) \tag{4.9}$$

where a is particle radius, κ^{-1} is Debye length, k_B is Boltzmann's constant, T is temperature, ε is the medium dielectric constant, ε_0 is the vacuum permittivity, e is the charge of an electron, z_v is the electrolyte valence, and ς_p and ς_w are the particle and wall surface potentials.

4.2.4 Particle-Field Potentials

Particle-field interactions include gravitational and dipole-magnetic field mediated potentials given as,

$$u^{pf}\left(\theta_{1,k},\phi_{2,k},z\right)=u_g^{pf}(z)+u_{df}^{pf}\left(\theta_{1,k},\phi_{1,k}\right) \tag{4.10}$$

such that the gravitational field only depends on *z*,

$$u_g^{pf}(z) = \frac{4}{3}\pi a^3 \left(\rho_p - \rho_m\right) gz = Gz \tag{4.11}$$

where ρ_p and ρ_m are particle and medium densities, and g is acceleration due to gravity. A particle dipole of moment, $\mathbf{m}$, interacts with a magnetic field, $\mathbf{H}$ [86], as given by (see Fig. 4.2(a)),

$$u_{df}^{pf}\left(\theta_{1,k}, \phi_{1,k}\right) = -\mathbf{m} \cdot \mathbf{H} \tag{4.12}$$

where $\mathbf{m}$ can correspond to either a Néel or Brownian dipole (discussed in the following).

4.2.5 Particle-Particle Potentials

Two interacting particles experience a magnetic dipole-dipole potential and an electrostatic double layer repulsion as,

$$u^{pp}\left(\theta_{1r,k}, \theta_{2r,k}, \phi_{1,k}, \phi_{2,k}, \phi_r, r\right) = u_{el}^{pp}(r) + u_{dd}^{pp}\left(\theta_{1r,k}, \theta_{2r,k}, \phi_{1,k}, \phi_{2,k}, \phi_r, r\right) \tag{4.13}$$

where angles in the *x*-*y* plane are relative to the particles' center-to-center vector, $\mathbf{r}$, are denoted as $\theta_{1r,k}$ and $\theta_{2r,k}$; the subscript *r* indicates the angles are relative to $\mathbf{r}$ (see Fig. 4.2(b), note *k* is dropped). At low ionic strengths, particles do not experience van der Waals attraction and only the electrostatic term from DLVO theory needs to be taken into account, which is given by [124],

$$u_{el}^{pp}(r) = B^{pp} \exp\left[-\kappa\left(r - 2a\right)\right] \tag{4.14}$$

$$B^{pp} = 32\pi\varepsilon_m a \left(\frac{k_B T}{ze}\right) \tanh\left(\frac{ze\varsigma_p}{4k_B T}\right)^2 \tag{4.15}$$

The magnetic dipole-dipole interaction is given by (expanding the typical vector expression) [86],

$$u_{dd}^{pp}\left(\theta_{1r,k},\theta_{2r,k},\phi_{1,k},\phi_{2,k},\phi_r,r\right)=$$
$$\frac{\mu_o}{4\pi r^3}\sum_{k=N,\mathrm{B}} m_{1,k}m_{2,k}\begin{Bmatrix}\mathrm{os}\left(\theta_{1r,k}-\theta_{2r,k}\right)\sin\left(\phi_{1,k}\right)\sin\left(\phi_{2,k}\right)+\cos\left(\phi_{1,k}\right)\cos\left(\phi_{2,k}\right)\\ -3\left[\cos\left(\theta_{1r,k}\right)\sin\left(\phi_{1,k}\right)\sin\left(\phi_r\right)+\cos\left(\phi_{1,k}\right)\cos\left(\phi_r\right)\right]\\ \left[\cos\left(\theta_{2r,k}\right)\sin\left(\phi_{2,k}\right)\sin\left(\phi_r\right)+\cos\left(\phi_{2,k}\right)\cos\left(\phi_r\right)\right]\end{Bmatrix} \tag{4.16}$$

where μ_0 is the vacuum permeability, and $m_{1,k}$ and $m_{2,k}$ are the magnitudes of the dipole moments on particles 1 and 2, which can correspond to either a Néel or Brownian dipole, which we review in more detail in the following section.

4.2.6 Magnetic Field & Dipoles

The force and torque expressions in the preceding sections require the field vector and dipole moments, which are inputs in the particle-field potential (Eq. (4.12)) and field mediated particle-particle potentials (Eq. (4.16)). In the following, we provide more detailed information on the time varying external magnetic field, the magnetic fields of nearby particles, and predicted dipole moments based on material properties. In an applied rotating field, the field vector can be expressed as a function of the intensity H_o and the magnetic permeability μ_o such that $H_o = B_o / \mu_o$, where B_o is the applied field. The field orientation depends on rotation speed, ω_f, as (where $\theta_f = \omega_f t$),

$$\mathbf{H}_o = H_o cos\left(\theta_f\right)\hat{\boldsymbol{x}} + H_o sin\left(\theta_f\right)\hat{\boldsymbol{y}} \tag{4.17}$$

When two particles are in proximity to each other, the field from a neighboring

particle's dipole is added to the total field. The magnetic intensity of a nearby particle is given by [44],

$$\mathbf{H}_p(r) = \frac{3\hat{\mathbf{r}}(\mathbf{m}\cdot\hat{\mathbf{r}}) - \mathbf{m}}{4\pi r^3 \mu_o} \tag{4.18}$$

and the total external field in Eq. (4.12) is the sum of the applied and local dipolar fields given as,

$$\mathbf{H} = \mathbf{H}_o + \mathbf{H}_p(\mathbf{r}) \tag{4.19}$$

When a magnetic dipole moment $\mathbf{m}$ is induced by an external magnetic field (for superparamagnetism [86]), its values is given by,

$$\mathbf{m} = \frac{4\pi a^3 \chi(\omega_f)\mu_o \mathbf{H}}{3} \tag{4.20}$$

where $\chi(\omega_f)$ is the dynamic susceptibility, which is a function of the static susceptibility and dipole relaxation times. The dipole in Eq. (4.20) can be used to compute the dipole-field interaction potential in Eq. (4.12). Practically, the Brownian dipole is modeled with a fixed magnitude. By combining Eqs. (4.18)-(4.20), the Néel dipole on one particle, $\mathbf{m}_{1,\mathrm{N}}$, induced by both an applied external field and the Néel, $\mathbf{m}_{2,\mathrm{N}}$, and Brownian, $\mathbf{m}_{2,\mathrm{B}}$, dipoles of a second adjacent particle is given by,

$$\mathbf{m}_{1,\mathrm{N}} = \frac{4}{3}\pi a^3 \mu_o \chi_N(\omega_f)\left[\mathbf{H}_o + \frac{3\hat{\mathbf{r}}(\mathbf{m}_{2,\mathrm{N}}\cdot\hat{\mathbf{r}}) - \mathbf{m}_{2,\mathrm{N}}}{4\pi r^3 \mu_o} + \frac{3\hat{\mathbf{r}}(\mathbf{m}_{2,\mathrm{B}}\cdot\hat{\mathbf{r}}) - \mathbf{m}_{2,\mathrm{B}}}{4\pi r^3 \mu_o}\right] \tag{4.21}$$

where $\chi_N(\omega_f)$ is the dynamic susceptibility corresponding to the Néel dipole only. The

magnitude of the Néel dipoles on particles 1 and 2 for use in the dipole-dipole potential in Eq. (4.16) are obtained by: (1) assuming the dipoles are equal in magnitude and direction (*i.e.*, $\mathbf{m}_{1,N} = \mathbf{m}_{2,N}, \mathbf{m}_{1,B} = \mathbf{m}_{2,B}$) on the right and left hand sides of Eq. (4.21), (2) algebraically solving for either $\mathbf{m}_{1,N}$ or $\mathbf{m}_{2,N}$, and (3) taking the magnitude of the dipole vector to obtain m_1 and m_2. The inaccuracy due to assuming $\mathbf{m}_{1,B} = \mathbf{m}_{2,B}$ (in this equation only) is negligible when the permanent dipoles are much smaller than the instantaneous dipoles.

4.2.7 Particle Susceptibility

The effective static susceptibility, $\chi_o(H)$, for a spherical particle is defined as a function of the static susceptibility, $\chi(H)$, as, [86]

$$\chi_o(H) = \chi(H)\left[1 + \left(\chi(H)/3\right)\right]^{-1} \tag{4.22}$$

The dynamic susceptibility as a function of the fractional contributions of the Néel and Brownian dipoles, f_N and f_B, and their associated relaxation times, τ_N and τ_B, is given by,

$$\chi(\omega_f) = \chi_N(\omega_f) + \chi_B(\omega_f) \tag{4.23}$$

$$\chi(\omega_f) = \chi_o\left[\frac{f_N}{1 + \left(i\omega_f\tau_N\right)^{1-\alpha}} + \frac{f_B}{1 + i\omega_f\tau_B}\right] \tag{4.24}$$

where α determines the Néel relaxation time distribution width.[33, 125] If some of the individual Néel dipoles have relaxation times on the order of the field rotation rate, they cannot overcome the energy barrier to reorient with the field.[32, 34] As a result, the Néel

dipole in a rotating field has in-phase, $\chi_N^{'}(\omega_f)$, and out-of-phase, $\chi_N^{''}(\omega_f)$ components of the susceptibility as,[35]

$$\chi_N(\omega_f) = \frac{f_N \chi_o}{1+(i\omega_f \tau_N)^{1-\alpha}} = \chi_N^{'}(\omega_f) - i\chi_N^{''}(\omega_f) \tag{4.25}$$

The Néel phase lag is defined as,

$$\theta_{lag,\mathrm{N}}(\omega_f) = arctan\left(\frac{\chi_N^{''}(\omega_f)}{\chi_N^{'}(\omega_f)}\right) \tag{4.26}$$

and components can be modeled as, [125]

$$\chi_N^{''}(\omega_f) = \frac{f_N \chi_o (\omega_f \tau_N)^{1-\alpha} \cos\left(\frac{1}{2}\pi\alpha\right)}{1+2(\omega_f \tau_N)^{1-\alpha} \sin\left(\frac{1}{2}\pi\alpha\right)+(\omega_f \tau_N)^{2(1-\alpha)}} \tag{4.27}$$

$$\chi_N^{'}(\omega_f) = \frac{f_N \chi_o \left[1+(\omega_f \tau_N)^{1-\alpha} \sin\left(\frac{1}{2}\pi\alpha\right)\right]}{1+2(\omega_f \tau_N)^{1-\alpha} \sin\left(\frac{1}{2}\pi\alpha\right)+(\omega_f \tau_N)^{2(1-\alpha)}} \tag{4.28}$$

4.2.8 Hydrodynamic Forces & Torques

Hydrodynamic forces and torques oppose translational and rotational motion of the particle. For low-Reynolds number dynamics, translational and angular velocities of particles can be directly related to the forces and torques by a mobility matrix, $\mathbf{M}$, given as,

$$\begin{pmatrix} \mathbf{u_1} \\ \mathbf{u_2} \\ \boldsymbol{\omega_1} \\ \boldsymbol{\omega_2} \end{pmatrix} = \mathbf{M} \begin{pmatrix} \mathbf{F}_1 \\ \mathbf{F}_2 \\ \mathbf{T}_1 \\ \mathbf{T}_2 \end{pmatrix} \tag{4.29}$$

$$\mathbf{M} = \begin{pmatrix} \mathbf{a}_{11} & \mathbf{a}_{12} & \tilde{} & \tilde{} \\ \mathbf{a}_{21} & \mathbf{a}_{22} & \tilde{} & \tilde{} \\ \mathbf{b}_{11} & \mathbf{b}_{12} & \mathbf{c}_{11} & \mathbf{c}_{12} \\ \mathbf{b}_{21} & \mathbf{b}_{22} & \mathbf{c}_{21} & \mathbf{c}_{22} \end{pmatrix} \tag{4.30}$$

where $\mathbf{M}$ is the mobility matrix containing near-field and far-field terms, obtained for two particles using twin multipole expansions [122]. When expanded, the mobility matrix has 6N × 6N terms. Here, N=2 so that the mobility matrix $\mathbf{M}$ is 12 × 12. If the particles are infinitely far from each other, only diagonal terms are nonzero and for spheres, $a_{ii} = 1/6\pi\eta a$ and $c_{ii} = 1/8\pi\eta a^3$. The mobility matrix is related to the resistance matrix, **R,** by,

$$\mathbf{MR} = \mathbf{I}$$

$$\begin{pmatrix} \mathbf{a}_{11} & \mathbf{a}_{12} & \tilde{} & \tilde{} & & & \tilde{} & \tilde{} & & & 0 & 0 \\ \mathbf{a}_{21} & \mathbf{a}_{22} & \tilde{} & \tilde{} & & & \tilde{} & \tilde{} & & & 0 & 0 \\ \mathbf{b}_{11} & \mathbf{b}_{12} & \mathbf{c}_{11} & \mathbf{c}_{12} & & & & & & & & \\ \mathbf{b}_{21} & \mathbf{b}_{22} & \mathbf{c}_{21} & \mathbf{c}_{22} & & & & & & & & \end{pmatrix} \begin{pmatrix} \mathbf{B}_{11} & \mathbf{B}_{12} & \mathbf{C}_{11} & \mathbf{C}_{12} \\ \mathbf{B}_{21} & \mathbf{B}_{22} & \mathbf{C}_{21} & \mathbf{C}_{22} \end{pmatrix} = \begin{pmatrix} 0 & 0 & 1 & 0 \\ 0 & 0 & 0 & 1 \end{pmatrix} \tag{4.31}$$

The elements in **R** are dependent upon the relative distances and orientations of particles as given by expressions using the notation of the original reference [122],

$$\begin{aligned} A_{ij}^{\alpha\beta} &= X_{\alpha\beta}^{A} e_i e_j + Y_{\alpha\beta}^{A} (\delta_{ij} - e_i e_j) \\ B_{ij}^{\alpha\beta} &= \tilde{} \quad {}_{ijk} e_k \\ C_{ij}^{\alpha\beta} &= X_{\alpha\beta}^{C} e_i e_j + Y_{\alpha\beta}^{C} (\delta_{ij} - e_i e_j) \end{aligned} \tag{4.32}$$

where the terms on the right-hand-side correspond to Jeffrey and Onishi's resistance functions defined at "arbitrary separations" (including recently reported corrections [126]), α, β correspond to particle number, and $\boldsymbol{e} = \mathbf{r}/r$ such that $e_i e_j$ and $\delta_{ij} - e_i e_j$ indicate parallel and perpendicular to the line of particle centers, respectively.

4.2.9 Brownian Forces & Torques

The Brownian force and torque can be combined into one vector $\mathbf{S}^B$ as,

$$\mathbf{S}^B = \begin{pmatrix} \mathbf{F}^B \\ \mathbf{T}^B \end{pmatrix} \tag{4.33}$$

which follows a Gaussian distribution with a mean of zero and variance given by,

$$\left\langle \mathbf{S}_i^B(0)\mathbf{S}_j^B(t) \right\rangle = 2(kT)^2 \mathbf{D}_{ij}^{-1}\delta(t) \tag{4.34}$$

where in practice $\mathbf{S}^B$ is computed from a vector of normal deviates weighted by a Cholesky decomposition of the resistance matrix, $\mathbf{R}$. [94]

4.2.10 Particle & Doublet Rotation

The angular velocity of a particle in a rotating magnetic field can be calculated by balancing the viscous torque, $\mathbf{T}^{H,R}$, against the dipole-magnetic field torque, $\mathbf{T}_{df}^P$, as,

$$\mathbf{T}_{df}^P = -\mathbf{T}^{H,R} \tag{4.35}$$

The gradient of the dipole-field potential (Eq. (4.12)) with respect to orientation gives the torque on the dipole moment of a particle, which is the sum of the torques due to the Néel and Brownian dipolar contributions given as,

$$\mathbf{T}_{df}^P = \sum_{k=N,\mathrm{B}} \mathbf{m}_k \times \mu_o \mathbf{H} \tag{4.36}$$

In a field in the *x-y* plane, Eq. (4.36) depends on the angle of the dipole in the *x-y* plane, $\theta_{l,k}$ and with respect to the z-axis $\phi_{l,k}$ (see Fig. 4.2(a)) as given by,

$$T_{df,z}^P = \sum_{k=N,\mathrm{B}} m_k \mu_o H_o sin\left(\theta_f - \theta_{1,k}\right) sin\left(\phi_{1,k}\right) \tag{4.37}$$

and $\theta_{lag,k} = \theta_f - \theta_{1,k}$ is defined as the phase lag of either the Néel dipole (from Eq. (4.26)) or Brownian dipole (determined directly from the particle main axis).

For isolated particles, the particle is also rotating around the axis perpendicular to the wall, leading to a negligible wall hydrodynamic correction [127], and negligible motion with respect to the polar axis is assumed. As such, the hydrodynamic drag is approximated as,

$$T_z^{H,R} = \omega_p 8\pi\eta a^3 \tag{4.38}$$

For the Néel dipole, only the out-of-phase component contributes to the torque, therefore the velocity can be written as (using Eq. (4.20) for the Néel out-of-phase dipole),

$$\omega_p = \frac{m_B \mu_o H_o sin\left(\theta_f - \theta_{1,\mathrm{B}}\right) + \frac{4}{3}\pi a^3 \chi_N^{"}\left(\omega_f\right)\mu_o H^2{}_o}{8\pi\eta a^3} \tag{4.39}$$

The critical frequency is the frequency at which the particle experiences a maximum dipole-field torque. If the critical frequency is less than the field frequency, the angle between the particle and the field gradually increases. When that angle reaches π, the particle experiences backwards rotation until it is once again aligned with the field. The frequency of one such forwards-backwards oscillation for single particles can be inferred from a previous model for rigid doublet rotation [116]. When this model is applied to a single particle, the oscillation frequency, ω_{osc}, relates to single particle critical frequency, ω_{crit}, and field frequency as,

$$\omega_{osc} = \omega_{crit}\sqrt{\left(\frac{\omega_f}{\omega_{crit}}\right)^2 - 1} \tag{4.40}$$

During each oscillation for single particles, the particle axis angular displacement is -

2π with respect to the field. In this regime, the average frequency of particle rotation is the difference in the field frequency and the frequency of one oscillation cycle given by,

$$\bar{\omega} = \omega_f - \omega_{osc} \tag{4.41}$$

Similar to the single particle analysis, a critical frequency exists for a rotating rigid doublet. The oscillation frequency has the same form as Eq. (4.40) but considers the weighted contribution from both Néel and Brownian dipoles as given by,

$$\frac{\omega_{d,osc}}{2} = \omega_{d,crit}\sqrt{\left(\left[\frac{\sum_{k=N,\mathrm{B}} m_k\omega_k}{\sum_{k=N,\mathrm{B}} m_k}\right] / \omega_{d,crit}\right)^2 - 1} \tag{4.42}$$

where $\omega_{d,crit}$ and $\omega_{d,osc}$ are the critical and oscillation frequencies of the doublet vector $\mathbf{r}$. In one cycle of forward-backward rotation, the doublet angular displacement is -π with respect to the average dipole trajectory. The average frequency of rotation in this regime is the difference in the overall dipole rotation and half of one doublet-oscillation cycle given by,

$$\bar{\omega}_d = \left[\frac{\sum_{k=N,B} m_k\omega_k}{\sum_{k=N,B} m_k}\right] - \frac{\omega_{d,osc}\left(\bar{\omega}\right)}{2} \tag{4.43}$$

4.3 Materials and Methods

4.3.1 Particles and Surfaces

M-270 carboxylic acid-coated microparticles composed of iron oxide nanoparticles embedded in a polystyrene matrix with nominal diameter 2.8um were used as received (Dynabeads, Life Technologies). To visualize particle orientation, a nonmagnetic film was coated on one hemisphere to make “optical Janus” particles (Fig. 3.1). The particles as

received were dried as a monolayer on a glass slide. The slides with the half-exposed dried particles were coated using an E-beam evaporator by first depositing a 15nm thin film of Cr to aid the adhesion of Au, followed by 35 nm Au film, and finally a 30 nm SiO_2 film. The microscope slides were sonicated in DI water to remove the coated particles from the surface and the solution was centrifuged to collect the particles.

Experiments were conducted on glass coverslips (Gold Seal, Corning) for 100x objectives or regular glass slides (Fisher Scientific) for 40x objectives. Coverslips or slides were sonicated in Acetone (Sigma-Aldrich Company) and then Isopropanol (Sigma-Aldrich Company), and soaked in Nochromix (Godax Laboratories) for 1-24 hours, rinsed in deionized water, sonicated in 0.1M KOH for 35 minutes to charge the surface, rinsed with deionized (DI) water, and dried with nitrogen gas. Sample cells containing dilute particles in 0.1mM NaCl were prepared by dispensing the dispersion into Viton o-rings (McMaster Carr) coated with vacuum grease on coverslips/slides and sealed using epoxy quickset glue (Loctite) and a top coverslip.

4.3.2 Microscopy & Magnetic Field Apparatus

FIG. 4.3. Image of the magnetic quadrupole apparatus, showing the two sets of four solenoids.

For rotating doublet and single particle magnetophoresis experiments, a 40x objective (Nikon) was used to monitor particles. For single particle and particle rotation in doublet experiments, a 100x oil objective (Nikon) was used to detect orientation of "optical Janus" particles. For all experiments, a Photron PCI-512 camera was used to record video at 60 or 120 frames per second (fps) of the field of view of the microscope. Coverslips/slides with the colloidal particles were placed on a stage in the center of a magnetic quadrupole set-up, which has been described elsewhere. [101] Briefly, two sets of four solenoids are arranged in a quadrupole (see Fig. 4.3) and solenoids receive a current that is $90°$ out of phase with the preceding solenoid to produce a constantly rotating field with uniform magnitude. In a second operating mode, a differential current through opposing solenoids creates a controllable field gradient along a single axis. A uniform 5 Gauss/mm gradient was applied for magnetophoresis experiments.

Videos were analyzed using particle tracking codes written in FORTRAN for doublet rotation or in MATLAB for particle rotation. For particle angular orientation images, we apply the bandpass filter bpass.m (adapted for MATLAB from the original particle tracking codes [128]) that enhances the contrast between the gold particle patch, the rest of the particle, and the background. We then use the MATLAB built-in function bwboundaries to identify the boundaries of our particles and the patch by their higher intensities relative to the rest of the image. The coordinate of the patch is determined by weighting the intensities of all pixels within the patch. For single particles, the center of the particle is the average position of the boundary pixels. For particles within doublets, two circles are fit to the doublet outline to find the centers of the particles. Lastly, the orientation is calculated based on the angle of the patch with respect to the centers of the particles. Figure 4.4 shows experimental

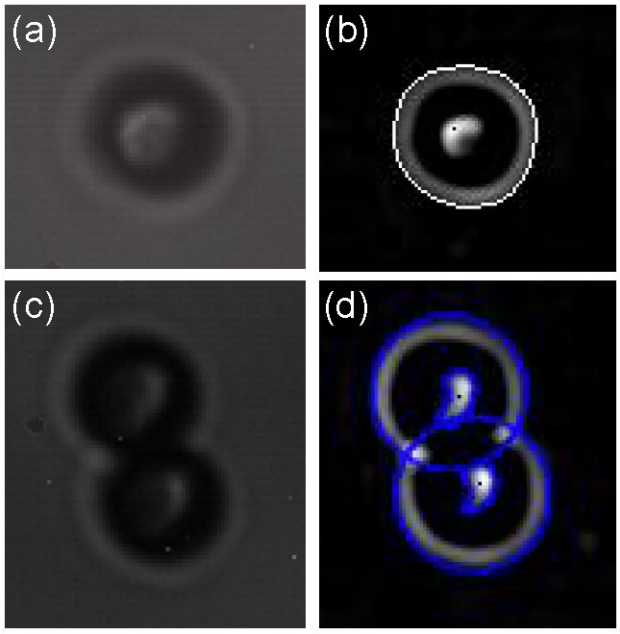

FIG. 4.4. (a) Experimental image of single particle with gold patch, and (b) the corresponding image obtained from increasing the contrast, identifying the outline of the particle and the patch, and calculating the location of the patch, marked with a black dot. (c) An experimental image of two particles within a doublet, both with gold patches, and (d) the corresponding image after analysis, showing in blue the circles fit to the outlines of the particles, the borders of the patches, and the locations of the patches marked with black dots.

images before and after the analysis is applied for single particles and particles within doublets.

4.3.3 Particle Characterization

Single particle drift in a field gradient, or magnetophoresis, can be used to calculate the static susceptibility as a function of field intensity in the case where the intensity negligibly changes in the field of view [43]. Static susceptibility values (for brevity here and throughout, the effective static susceptibility is referred to as the static susceptibility) calculated from magnetophoresis experiments are shown in Table I. Further details on the measurements are in the Appendix (see Figure 4.9).

The dynamic susceptibility due to the Néel dipole (Eqs. (4.25)-(4.28)) was determined by two independent methods: PPMS measurements and single particle rotation at high frequencies (when the Brownian dipole does not contribute to rotation in Eq. (4.39)). Phase lag and the in-phase and out-of-phase components at different magnetic field frequencies were measured using a Particle Property Measurement System (PPMS) (Quantum Design). The magnetic microparticles were characterized either as a powder or in a dried agar matrix. For the powder, the microparticles were dried on a glass slide and scrapped off. For the agar matrix, agar powder (Type I, Sigma-Aldrich Company) was heated until dissolved in DI water. Colloids were directly added to the solution and sonicated. The dispersion was then poured onto a petri dish and left overnight to harden. Prior to measurement, the agar gel was vacuum-dried. Frequencies ranged from the minimum of 10 Hz to 200 Hz at a constant field of 10 Gauss and an oscillating field of 6 Gauss. Equations (4.26)-(4.28) were used to fit the PPMS measurements for unknowns α and τ_N (note χ_o and f_N cancel in E q. (4.26)), assuming they do not change in this field range. In the second method, we

conducted a torque balance of single particle rotation at 10 Hz, 50 Hz, and 100 Hz at 6 Gauss and 10 Gauss, respectively, and fit $\chi_N''(\omega_f)$ (Eq. (4.27)) via adjustable parameters α and τ_N, given χ_o and an estimate of f_N (which was verified via an iterative method to simultaneously fit the Néel dipole measurements and the Brownian dipole, described below). The parameters that fit both PPMS and particle rotation data are shown in Table I, and the PPMS data along with the susceptibility theory is plotted in the Appendix in Figures 4.10-4.11.

The magnitude of the Brownian dipole can be determined from a torque balance at critical frequencies, at which the Brownian dipole dominates the torque expression (Eq. (4.37)). At frequencies < 10 Hz, the Néel dipole component $\chi_N''(\omega_f)$ is estimated to be $\approx$ 0.02 (from the above-mentioned model) and at the critical frequency, the Brownian dipole phase lag $\theta_f - \theta_{1,B} = \pi/2$, hence m_B is the only unknown in Eq. (4.39). The Brownian dipole m_B and fractions f_B and f_N were determined in an iterative fashion by minimizing error in Eqs. (4.26)-(4.28) and Eq. (4.39). Explicitly, $f_B = m_B / \mathbf{m}$ where $\mathbf{m}$ is the total dipole in A/m^2 by using χ_o for susceptibility in Eq. (4.20) and $f_N = 1 - f_B$, which is used to calculate $\chi_N''(\omega_f)$ in Eq. (4.27), then $\chi_N''(\omega_f)$ used in Eq. (4.39). The values are shown in Table I. It is assumed that the magnitude of the Brownian dipole does not change significantly in this field and frequency range. Figure 4.11 in the Appendix shows the critical frequency data and theoretical fits to describe the particles' dynamic susceptibility.

4.3.4 Brownian Dynamics Simulations

BD simulations were performed based on Eqs. (4.3) and (4.4) with an integration

time of 0.01 ms, which is short enough to assum[3]e constant force but long enough for momentum relaxation.[28] Equation (4.3) can be approximated by using the midpoint rule to avoid calculating the gradient of the diffusion tensor.[129-131] Initial doublet, particle, and field orientation was always 0° or parallel to the x-axis, with an initial separation of 3.03 μm, which is an estimate of the energy minimum at all frequencies determined from a probability distribution from experimental data. Simulations were run for at least 15 s, which was found to be sufficient to obtain particle and doublet average rotation frequency, and adequate given doublets reach steady state after approximately <1 s. Particle coordinates (positions, angles) were recorded every 1 ms. Particle, wall, and solution properties used in the simulation are shown in Table 1. The Néel phase lag values from the model (see Eq. (4.26)-(4.28)**,** Table I) were directly used in BD simulations at 6 Gauss.

TABLE 4.I. Parameters used in the BD Simulations.

Parameter	Value	Equation
$-\zeta_p$ (mV)[a], $-\zeta_w$ (mV)	50	(4.9), (4.15)
a (nm)[b]	1400	(4.8), (4.9), (4.11), (4.14), (4.15), (4.21)
κ^{-1} (nm)	30.3	(4.8), (4.14)
χ_o at 6 Gauss[c]	1.46	(4.24),(4.25),(4.27) ,(4.28)
χ_o at 10 Gauss[c]	1.33	(4.24),(4.25),(4.27) ,(4.28)
α [d]	0.87	(4.24),(4.25),(4.27) ,(4.28)
τ_N (s)[d]	2.5E-9	(4.24),(4.25),(4.27) ,(4.28)
m_B (10^{-16} A/m^2)[e]	3.0	(4.12), (4.16), (4.21)
f_B at 6 Gauss (%)[f]	3.75	(4.24),(4.25)
f_B at 10 Gauss (%)[f]	2.5	(4.24),(4.25)
f_N at 6 Gauss (%)[f]	96.25	(4.24),(4.25)
f_N at 10 Gauss (%)[f]	97.5	(4.24),(4.25)

[a]Reference [25]
[b]Reported by the manufacturer.
[c]Fit to magnetophoresis experiments.
[d]Fit to both PPMS measurements and torque balance experiments.

[e]Fit to single particle critical frequency measurements.

[f]Calculated using m_B and the total dipole (plug in χ_o in Eq. (4.20)).

Due to the particles' proximity to the underlying wall, translational motion parallel to the wall will be slowed.[97] However, translation-rotation coupling increases with wall proximity,[127] speeding up translational motion. We made the assumption that the overall net effect of the wall would be a reduction in translational motion, although not as reduced as a single particle translating parallel to the wall. To validate this assumption, we ran Stokesian Dynamics (SD) test cases that included particle-particle, particle-wall and multi-body hydrodynamics[127, 131, 132] and compared them to BD simulations run with a 1.35 resistance increase for the translational diagonal terms. The simulations agreed qualitatively near the critical frequency and at high frequencies. Regarding quantitative agreement, for 10 trials at a high frequency case (50 Hz at 6 Gauss), the difference in mean doublet rotation for SD vs. BD was ~20% and the results were within one standard deviation of each other. For 10 trials at a frequency right after the critical frequency (0.6 Hz at 6 Gauss), the difference in mean doublet rotation was ~30%. Since both the SD and BD results at these frequencies were still within the ranges that were observed in experiment, we used the computationally less expensive BD simulations.

4.4 Results and Discussion

4.4.1 Single Particle Rotation

Single particle rotation rates were measured in fields of 6 and 10 Gauss and rotation frequencies from 0.1 Hz to 100 Hz. Representative rotational trajectories are plotted in Fig. 4.5(a) from VM and BD simulations for particles in 0.8 Hz and 80 Hz fields at 6 Gauss. Oscillations in the angular trajectory at 0.8 Hz demonstrate that the particle cannot rotate as fast as the field, which occurs after a critical frequency. Fig. 4.5(b) shows the Fast

Fourier Transform (FFT) of the sine of the angular trajectories (normalized by the greatest nonzero peak) for both the simulation and experiment at 0.8 Hz. The BD simulation reproduces the single particle rotation, capturing both a dominant frequency at 0.8 Hz and a secondary frequency at ≈ 0.3 Hz.

Figure 4.5(c) and Fig. 4.5(d) summarize single particle rotation frequency vs. field rotation frequency at 6 and 10 Gauss for experiments and simulation. Particles rotate at the same frequency as the field up to critical frequencies of ≈ 0.6 Hz for 6 Gauss and ≈ 1 Hz for 10 Gauss. The results can be understood by considering the torques on both the Brownian and Néel dipoles. At low frequencies (<2 Hz for 6 Gauss, <8 Hz for 10 Gauss), the particles have an effectively "permanent" dipole, on the time scale of the experiment, which aligns with the field orientation via Brownian relaxation. At frequencies >2 Hz for 6 Gauss and >8 Hz for 10 Gauss, the field is rotating with a time scale on the order of ~0.1 s, whereas the Brownian relaxation time is $\tau_B = 4\pi\eta a^3/kT \approx 7.5$ s, and therefore the torque from the Brownian dipole averages to zero.

Because the ensemble Néel dipole has a characteristic relaxation time of $\tau_N \approx 1\text{x}10^{-9}$s, it is aligned with the field at all frequencies. However, the Néel relaxation time distribution is broad (described by α), with a finite out-of-phase component of the Néel dipole,[37] which produces a frequency-dependent torque on the particle.[31, 35] As such, the particle rotation frequency plateaus, and then slightly increases as the phase lag begins to increase in external fields up to 100 Hz. It is expected that at frequencies >100 Hz, particle rotation will continue to increase as the out-of-phase component increases.[37] The agreement between simulations and experiments shows the dipole relaxation model accurately captures the measured dynamics. We proceed with these properties to analyze doublet

rotation experiments.

4.4.2 Particles Rotating within Rotating Doublets

We report in Fig. 4.6 the rotation of individual particles within doublets in 6 and 10 Gauss fields from 0.1 Hz to 100 Hz. Rotation frequency results were not significantly different from those of isolated rotating particles. The variation in particle rotation rates is most likely due to non-uniformity between particles, such as size, static susceptibility, and phase lag. To demonstrate the particle non-uniformity, Fig. 4.6(a) shows angular trajectories of particles rotating at 0.8 Hz and 80 Hz at 6 Gauss. The two experimental plots shown for the 0.8 Hz case are distinct particles rotating in the same doublet. For comparison, the isolated particle at 0.8 Hz in Fig. 4.5(a) rotates at a frequency in between these two particles.

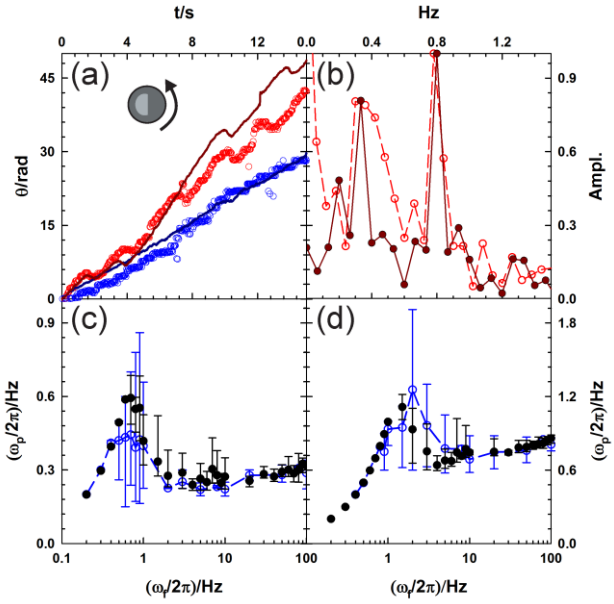

FIG. 4.5. (a) Angular trajectories of VM experiments and BD simulations of isolated single particles at 6 Gauss and 0.8 Hz (red, top) and 80 Hz (blue, bottom) (see VM movies and BD renderings of particles rotating at 0.8 Hz in Video S1[1]). In all plots, experimental results are shown by light filled symbols, and simulation results are shown by dark unfilled symbols. (b) Fast Fourier transform (FFT) of the sine of the angular coordinate of the 0.8 Hz trajectories for both experiment and simulation. Single particle rotation frequency vs. applied field frequency for (c) 6 Gauss and (d) 10 Gauss with experimental averages with range bars (min & max) and BD simulation results.

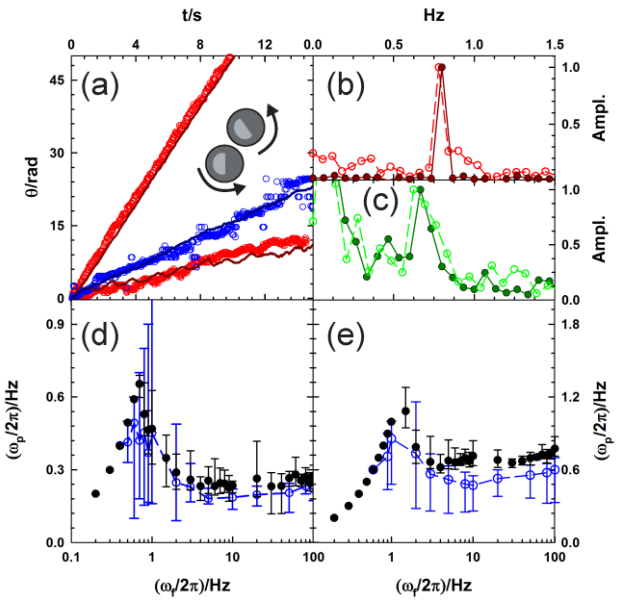

FIG. 4.6. (a) Angular trajectories of VM experiments and BD simulations of particles rotating within a doublet at 6 Gauss and 0.8 Hz (red, top and bottom) or 80 Hz (blue, middle) (see VM movies and BD renderings of particles rotating in a doublet at 0.8 Hz and 80 Hz in Videos S2 and S3[1]). The two 0.8 Hz experimental plots are of particles within the same doublet, illustrating the range in magnetic properties. In all plots, experimental results are shown by light filled symbols, and simulation results are shown by dark unfilled symbols. (b) FFT of the sine of the angular coordinate of the faster 0.8 Hz trajectory for both experiment and simulation and (c) the FFT of the slower 0.8 Hz angular trajectory minus a linear fit of the same trajectory to capture the oscillation frequency of both experiment and simulation. Single particle rotation frequency within doublets vs. applied field frequency for (d) 6 Gauss and (e) 10 Gauss with experimental averages with range bars (min & max) and BD simulation results.

Figure 4.6(b) shows the FFT of the sine of the angular trajectory of the faster particle in the doublet in Fig. 4.6(a). The faster particle has a critical frequency greater than 0.8 Hz because it can still rotate with the field at 0.8 Hz, while its partner cannot. The slower particle is oscillating about an average rotation rate, indicating it is in a regime just past the critical frequency. BD simulations are fit to match the two particles' trajectories by increasing the Néel dipole phase lag for the faster particle (relative to the measured average) (to increase torque), and decreasing the phase lag for the slower particle (to decrease torque). Figure 4.6(c) shows the FFT of the slower particle trajectory minus a linear fit to the average trajectory (which captures the secondary oscillation frequency) for

both experiment and simulation in Fig. 4.6(a). The simulation captures the oscillation frequency in the experiment, as seen by the matching peaks at ≈ 0.67 Hz.

Figure 4.6(d) and Fig. 4.6(e) summarize particle rotation frequency within doublets vs. the field rotation frequency for 6 Gauss and 10 Gauss. The same general behavior is observed in these plots as isolated, single particles (Fig. 4.5). The particle follows the frequency of the field until a critical frequency of ≈ 0.6 Hz at 6 Gauss. For 10 Gauss experiments, the critical frequency is at ≈1 Hz, which is less than the ≈ 2 Hz simulation estimate. The discrepancy is most likely due to experimental over-sampling of "slow" particles (*i.e.*, particles with a smaller phase lag and/or smaller static susceptibility). Like the single particles, particles in a doublet continue to rotate even when the field frequency is several orders of magnitude greater than the Brownian relaxation time because the torque on the Néel dipole is nonzero. In the field frequency range 10-100 Hz, the particle frequency plateaus just above 0.2 Hz and 0.5 Hz for 6 and 10 Gauss, similar to the plateaus seen for single particles in Fig. 4.5(c) and Fig. 4.5(d).

The trajectory of the oscillating particle at 0.8 Hz is fit to a linear function to obtain an average rotation speed of 0.13 Hz. An available literature model[116] (Eqs. (4.40), (4.41)) predicts the frequency of oscillations given the average particle rotation and the field frequency as 0.8 Hz - 0.13 Hz = 0.67 Hz, which is close to the measured peak in Fig. 4.6(c). The critical frequency can also be estimated from this model, and is found to be ≈ 0.44 Hz, which is lower than the average measured value (see Fig. 4.6(d)). This also confirms what has been observed experimentally for this unique particle; it has a smaller overall susceptibility, Brownian dipole, and/or a smaller Néel dipole phase lag with the field, decreasing the field torque and reducing the critical frequency.

The effect of unique particle properties is evidenced by the large variation in particle rotation in the frequency regime near the critical frequency, as shown in Fig. 4.5(c), Fig. 5(d), Fig. 6(d), and Fig. 6(e). As expressed in Eq. (4.39), the Brownian dipole m_B and the out-of-phase Néel susceptibility $\chi_N^{"}\left(\omega_f\right)$ impact rotation at the lower frequencies and near the critical frequency, while $\chi_N^{"}\left(\omega_f\right)$ influences high frequency rotation. Changing the Néel dipole phase lag by ~0.01 radian will shift the critical frequency for unique single particles. It has been noted previously for these particles that non-uniformity can alter the observed dynamics [36], thus the stochastic nature of the system, including particle

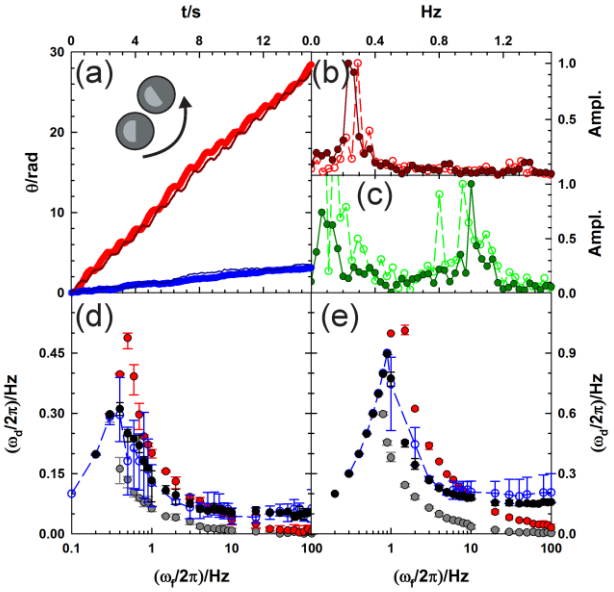

FIG. 4.7. (a) Angular trajectories of VM experiments and simulations of doublets rotating at 6 Gauss and 0.8 Hz (red, top) or 80 Hz (blue, bottom) (see VM movies and BD renderings of rotating doublets at 0.8 Hz and 80 Hz in Videos S2 and S3[1]). In all plots, experimental results are shown by light filled symbols, and simulation results are shown by dark unfilled symbols. (b) FFT of the sine of the angular coordinate of the 0.8 Hz trajectory for both experiment and simulation and (c) the FFT of the 0.8 Hz angular trajectory minus a linear fit of the respective trajectory to capture the oscillation frequency for both experiment and simulation. Doublet rotation frequency vs. applied field frequency for (d) 6 Gauss and (e) 10 Gauss with experimental averages with range bars (min & max) and BD simulation results. In plots (d) and (e), simulations with exact mobility matrix (Eq. (4.30)) (black) are compared to simulations run as if the particles are non-interacting with all off-diagonal elements in the matrix zero (red) and as if the particles have no translation-rotation or rotation-translation coupling (*i.e.*, $\mathbf{b}$, $\tilde{\Gamma}$ in Eq. (4.30) are zero) (gray).

heterogeneity, explains why in some cases the simulation data is not within range of the experimental data. The parameters presented in Table I reproduce with good agreement the features observed in the single particle and particle in doublet experiments, but can be tuned to obtain more quantitative agreement for distinct particles.

4.4.3 Doublet Rotation

Figure 4.7 displays representative measured and simulated doublet rotational trajectories for doublets experiencing a 0.8 Hz or 80 Hz field at 6 Gauss. Oscillations in the 0.8 Hz trajectories indicate this frequency is greater than the critical frequency for doublets. The normalized FFT plots of the sine of the 0.8 Hz experiment and simulation trajectories in Fig. 4.7(b) show alignment of the peaks at ≈ 0.3 Hz, demonstrating that the simulation captures the dominant doublet frequency. The FFT of the 0.8 Hz trajectories minus linear fits is shown in Fig. 4.7(c) to obtain the frequency of the rotational oscillations. The experiment data has two peaks at ≈ 0.8 and ≈ 1 Hz, most likely due to particle non-uniformity, whereas the simulation shows a single oscillation frequency at ≈ 1 Hz.

Oscillations in doublet rotation occur just past the observed critical frequency because the dipoles of two particles rotate faster than the doublet vector. When the angle between the doublet vector and the weighted average dipole (*i.e.* Néel and Brownian) reaches 90°, the doublet vector rotates backwards to realign with the particle dipoles, and the cycle begins again. The previously mentioned model for single particle rotation, which relates the critical frequency and oscillation frequency to the average rotation frequency for a given field frequency, is adapted from a one-dimensional torque balance of a bound doublet [116]. Such a simple torque balance may not easily capture the doublet rotation rate, because: (1) the doublet may not be rigidly rotating, (2) the doublet vector is coupled to a torque

balance involving the individual particle dipoles, and (3) the dipoles experience stochastic translation and rotation that may not be captured by a simple average interaction.

We compare the simple model to the double rotational trajectory at 0.8 Hz to determine how the model's assumptions may limit its applicability for quantitative predictions of freely rotating doublets. First, we estimate that the overall dipoles rotate at the same frequency as the field at 0.8 Hz; this should be a valid assumption given the relaxation time of the Néel dipole and the fact that the Brownian dipole is an order of magnitude smaller than the Néel dipole (see Table I). Then, given the average doublet rotation rate of 0.3 Hz, the oscillation frequency should be 2(0.8 Hz - 0.3 Hz) = 1 Hz (see Eq. (4.43)). This is comparable to the observed peak in Fig. 4.7(c) for the simulation, but the secondary peak at 0.8 Hz for the experiment may indicate that the dipoles are not rotating at the same rate as the field. Next, using the value of 0.8 Hz as the dipole rotation, the estimate of the critical frequency can also be calculated from the model, and for this doublet it is ≈ 0.6 Hz, which is higher than the experimental upper bound of 0.4 Hz (see Fig. 4.7(d)). We attribute this discrepancy to the fact that the doublet is not rigidly rotating.

Figure 4.7(d) and Fig. 4.7(e) summarizes doublet frequency vs. field frequency at 6 and 10 Gauss. BD simulations with the exact particle-particle hydrodynamic tensor (Eq. (4.30) with all terms) are plotted as dark circles and fall within the upper and lower values observed in the experiments. Critical frequencies are observed at 0.4 Hz for 6 Gauss and 1 Hz for 10 Gauss. Low frequency rotation below the critical frequency can be understood as follows; the particles' Brownian and Néel dipoles rotate at the same frequency as the field, and as a result, the doublet also rotates due to the favorable head-to-tail alignment of their dipoles. This is captured in Eq. (4.16) where particles experience a tangential force in

the θ_r direction when their dipoles are not aligned along the center-to-center vector **r**. At intermediate frequencies just above the critical frequency, the doublet vector increasingly lags behind the particle dipoles and when the lag reaches 90°, the doublet rotates backwards (hence the observed oscillations in the angular trajectory) to re-align with the dipoles. As described earlier, at higher frequencies, the Brownian dipole orientation averages out to zero but the Néel dipoles of the particles are still rotating with the field (with a characteristic lag). In this regime, the particles cannot reorient around each other, on the time scale of the field rotation, to align their Néel dipoles as part of doublet rotation. This would imply that the doublet would not rotate at frequencies much greater than the critical frequency for doublets due to viscous drag. However, doublets are observed to continue to rotate at high frequencies in VM experiments (see VM movie at 80 Hz in Video S3).

The significance of hydrodynamic interactions and their contribution to doublet rotation is illustrated by testing two additional approximate mobility matrices in the BD simulations, which are also shown in Fig. 4.7(d) and Fig. 4.7(e). One approximation is a mobility matrix with only diagonal terms corresponding to $a_{ii} = 1/6\pi\eta a$ and $c_{ii} = 1/8\pi\eta a^3$ (red points in Fig. 4.7(d) and Fig. 4.7(e) shifted to the right of the critical frequency). These simulations overestimate the critical frequency because the particles experience an overall smaller viscous resistance. In addition, doublet rotation vanishes at high frequencies in simulations with only diagonal terms. These results imply that the doublet rotates at low frequencies due to dipolar interactions, a behavior that is still qualitatively captured by the simple hydrodynamic model, and at high frequencies due to hydrodynamic interactions that are not captured by this model. It appears that rotation of the particles within the doublet couples to their translation ($\mathbf{b}$, $\tilde{\Gamma}$ in Eq. (4.30)), leading to overall doublet rotation

at high frequencies.

To test the role of translation-rotation, BD simulations were also performed with $\mathbf{b}$ and $\tilde{\Gamma}$ removed from the mobility matrix; the results are shown as gray points (shifted to the left of the critical frequency) in Fig. 4.7(d) and Fig. 4.7(e). In this case, the doublet rotation rate is underestimated for frequencies >0.3 Hz for 6 Gauss and >0.7 Hz for 10 Gauss, indicating that translation-rotation coupling contributes to doublet rotation even at low frequencies. At higher field frequencies, doublet rotation vanishes without including coupling, which indicates that the translation-rotation coupling is the sole mechanism causing doublet rotation in this regime. This effect would still occur in simulations that only include far field hydrodynamics, although to a lesser extent, because the coupling terms in Eq. (4.32) remain qualitatively unchanged.

The results highlight the connection between individual particle dynamics and doublet dynamics: the particles' rotation within the doublet produces an asymmetric flow, causing particles to translate around each other and the doublet to rotate. This finding is supported by another literature study that also showed individual particle rotation contributed to rotation of larger clusters via a translation-rotation coupling mechanism [57]. Due to the relationship between particles and doublet rotation, the doublet experimental results can be used to confirm the dipole relaxation model applied in BD. At 10 Gauss, slightly greater phase lag values (+ ~0.01 radian) than those from the model fit parameters (α and τ_N in Eqs. (4.26)-(4.28)) were found to better match single particle and doublet experiments, but follow the trend of the model.

4.4.4 Particle Separation Dynamics

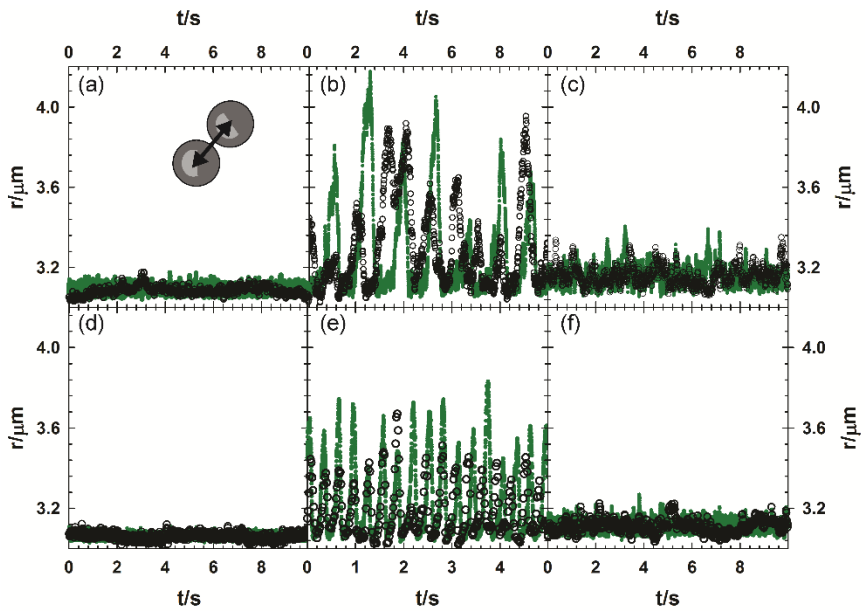

FIG. 4.8. Representative plots of particle-particle separation, r, vs. time, t, at 6 Gauss (a-c) and 10 Gauss (d-f) at frequencies below the critical frequency (a,d: 0.1 Hz), just after the critical frequency (b: 0.6, d: 2 Hz), and two orders of magnitude higher than the critical frequency (c: 50 Hz, f:100 Hz) for experiments (black, open circles) and simulations (green, closed circles). Oscillations in r are observed at frequencies near 0.5 Hz for 6 Gauss and near 2 Hz for 10 Gauss (similar to frequencies where secondary angular oscillations are seen for single particles and doublets in Figs. 4.5-7).

Particles in rotating doublets experience varying degrees of fluctuations in their center-to-center distance, $r = |\mathbf{r}|$ with varying field frequency. Separation distance as a function of time is plotted in Fig. 4.8 for three representative frequency ranges at 6 and 10 Gauss. At frequencies below the critical frequency (Fig. 4.8(a), Fig.4. 8(d)), the dipoles are aligned with **r**, and the dipole-dipole interaction is the same as if the field were constant. As such, strong dipolar attraction holds particles together with minimal fluctuations in r. At field rotation frequencies much greater than the critical frequency (Fig. 4.8(c), Fig. 4.8(f)), the Néel dipole is rotating several orders of magnitude faster than **r** such that the average angle between **r** and the dipoles is assumed to be $\approx 45°$. This still corresponds to a net attraction between particles (Eq. (4.16)), although it is much weaker than aligned dipoles at 0°, thus producing slightly larger fluctuations in r compared to the low frequency limit.

For field rotation frequencies near the critical frequency (Fig. 4.8(b), Fig. 4.8(e)), the particles intermittently separate and came back together at the same frequency as the oscillations in the doublet rotation (see Fig. 4.8). The simultaneous oscillations in θ_r and *r* are observable in both experiment and simulations. In this regime, the angle between the single particle dipoles and the doublet vector is periodically between 55°-90° and the particles experience a temporary repulsion. For comparison, the angular transition from attraction to repulsion occurs at ≈ 55° by solving a simplified version of Eq. (4.16) for point dipoles with identical magnitude restricted to the x-y plane. The temporary repulsion causes the particles to separate at the same time as the temporary reversal in rotation direction when the relative angle reaches 90°.

The BD simulation results in Fig. 4.8 capture the observed *r* oscillations at 0.6 Hz and 2 Hz for 6 and 10 Gauss, as well as the Brownian fluctuations in *r* in the low and high frequency ranges below and above the transition frequency range. The dipolar attraction is strongest when the angle between the single particle dipoles and doublet vector is ≈ 0°, which is the case at 0.1 Hz where the variation in *r* is seen to be ≈ 100 nm. The dipolar attraction between particles decreases at 50-100 Hz, as shown by the ≈ 200 nm variation in *r* at these frequencies. Variation in *r* is slightly greater in the simulation than is observed experimentally (observed in histograms of *r*), and this discrepancy is most pronounced in the oscillation regime. The error is most likely due to the approximate point-dipole potential (*i.e.*, Eq. (4.16)) used in simulations, which at close-range overestimates the repulsion by ~10% when the dipoles are perpendicular to the doublet vector and underestimates the attraction for aligned dipoles by ~20% [133].

4.5 Conclusions

Our findings demonstrate agreement between experiments, simulations, and models of superparamagnetic particle dynamics in rotating magnetic fields for single particles and doublets. Rotation of particles and doublets depends on dipole-field interactions, dipole-dipole interactions, and hydrodynamic interactions. Our results show that both dipolar interactions (including relaxation mechanisms) and hydrodynamic interactions (including exact 2-body, translation-rotation coupling) play an essential role in capturing non-equilibrium, steady-state rotation of magnetic particles vs. field rotation frequency. Simulations and modelling results verify that single particle rotation within doublets directly affects overall doublet rotation (via hydrodynamics), which we show is essential for qualitatively and quantitatively matching experiments with simulations. The effect is most notable at high frequencies when an increased Néel phase lag causes the particles to continue rotating. The direct measurements and rigorous models developed for single particles and rotating particle pairs within doublets provide a foundation to understand interactions and dynamics of magnetic particles in time varying fields important to colloidal assembly in field-driven systems.

4.6 Appendix

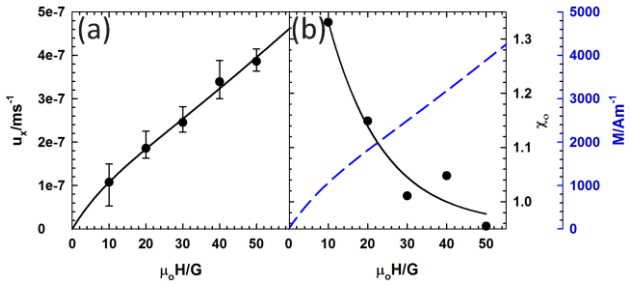

FIG. 4.9. (a) Measured mean drift, u_x, (points) vs. field strength, $\mu_o H$, in Gauss. The bars are max and min values. (b) Susceptibility, χ_o, (points) vs. $\mu_o H$ computed from Eq. (4.A.4) and fit to the empirical function in Eq. (4.A.5) (solid line). The solid line in part (a) is obtained by inserting Eq. (4.A.5) for the value of $\chi_o(H)$ in Eq. (4.A.4) and solving for u_x. Magnetization, $M = \chi_o(H) H$, is also plotted in (b) (dashed line) and agrees qualitatively with previously reported magnetization curves for superparamagnetic particles [134].

The effective static susceptibility, χ_o, for the particles is reported by the manufacturer as 0.96, but to obtain an estimate at the order of the field intensities used in this work, magnetophoresis experiments were conducted with a 5 Gauss/mm gradient at several field intensities. Single particle drift $\mathbf{u}$ is measured using particle tracking, and measurements are shown in Fig. 4.9(a). The susceptibility is calculated by solving a force balance between the magnetophoretic force [135] and viscous drag as,

$$\mathbf{F}_{mag} = (4/3)\pi a^3 \chi_o(H)\mu_o H \nabla \mathbf{H} \qquad (4.A.1)$$

$$\mathbf{F}_{drag} = 6\pi\eta a f(h)\mathbf{u} \qquad (4.A.2)$$

where $f(h)$=2.8 is a hydrodynamic correction due to lateral movement at height h from the wall [131, 136], and h is estimated from a balance of gravity and electrostatic repulsion as [137],

$$h = \kappa^{-1} \ln\left[\kappa B^{pw}/G\right] \qquad (4.A.3)$$

By equating Eqs. (4.A.1) and (4.A.2) at steady state, the susceptibility as a function of field strength, where the field gradient and the drift are in the x-direction, is as shown,

$$\chi_o(H) = \frac{(4/3)\pi a^3 \mu_o H \nabla H_x}{6\pi\eta a f(h) u_x} \tag{4.A.4}$$

We conducted 6 trials at 10 Gauss, and 3 trials for all other field intensities. The results are fit to an empirical function that has the form,

$$\chi_o(H) = c_1 + c_2 \exp(-c_3 \mu_o H) \tag{4.A.5}$$

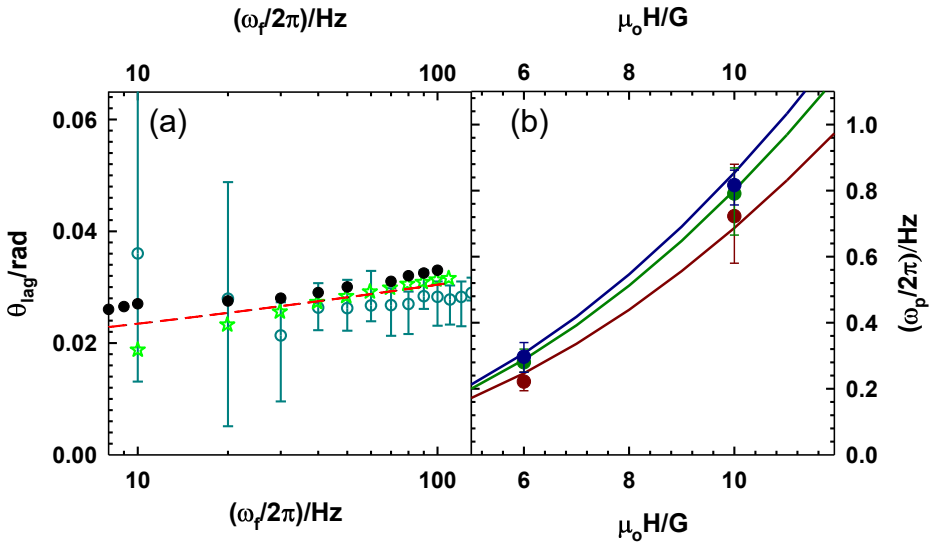

FIG. 4.10 (a) PPMS phase lag measurements for a powdered sample (green stars) and for a sample in an agar matrix (cyan open circles) with error bars, compared to a theoretical fit to Eqs. (4.26)- (4.28) (red dashed line) that also fits single particle rotation torque balance calculations. Phase lag values used in simulations at 10 Gauss (solid circles). Error bars are max and min values. (b) Average single particle rotation frequencies at 6 and 10 Gauss and 10 Hz (red, bottom), 50 Hz (green, middle) and 100 Hz (blue, top) are fit using a torque balance (Eq. (4.39), neglecting the Brownian dipole) to find theoretical $\chi_N^{"}(\omega_f)$ that follow the model (Eq. (4.27)). Parameters determined from the torque balance fits agree with the fit to independent PPMS measurements.

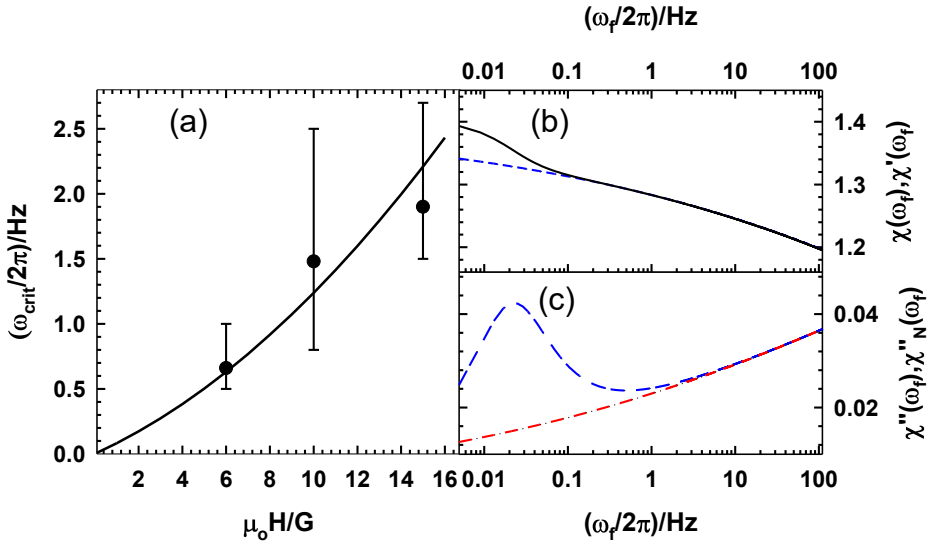

FIG. 4.11. (a) Single particle critical frequency is plotted (solid circles with error bars) at different field magnitudes to find an estimate for the Brownian magnetic dipole using an approximate Néel out-of-phase susceptibility value of 0.02 (fit is the solid line). All error bars are max and min values. Theoretical functions for the susceptibility components that include both Brownian and Néel relaxation times (see Eq. (4.24)) are plotted in (b) and (c). (b) In-phase component of the susceptibility (blue dashed line) and the magnitude of the susceptibility (solid line) and the (c) out-of-phase susceptibility (blue dashed line) and the Néel out-of-phase component only (red dotted line) at 6 Gauss.

where c_1=0.9569, c_2=0.7709, c_3=0.072. Experiments are not conducted at 6 Gauss due to the need to run very long videos to get an accurate drift. Instead, $\chi_o(6G/\mu_o)$ was determined based on Eq. (4.A.5). Magnetization defined as $M=\chi_o(H)H$ is plotted on a separate *y*-axis in Fig 4.9(b). Note that throughout the main text, the H in $\chi_o(H)$ is dropped and χ_o is referred to as the static susceptibility.

5. EFFECTIVE COLLOIDAL INTERACTIONS IN ROTATING MAGNETIC FIELDS

Non-equilibrium, steady state effective pair potentials of micron-sized superparamagnetic particles in rotating magnetic fields are obtained vs. field frequency and amplitude. Trajectories of center-to-center distance between particle pairs from Brownian Dynamic (BD) simulations, which were previously matched to experimental measurements, are analyzed to obtain local drift and diffusion coefficients. These coefficients are used to obtain effective interaction potentials from solving a one-dimensional Fokker-Planck (FP) equation. Biased sampling of the effective energy landscape was implemented by intermittent switching between the field of interest and a repulsive field. Our findings show how the shape and attractive well-depth of pair interactions can be tuned by changing field frequency and amplitude.

5.1. Introduction

The application of external fields to colloidal dispersions is of interest for controlling particle interactions, dynamics, and microstructure.[58, 138-142] A subset of these systems are non-equilibrium, steady state processes that can produce novel flow fields and configurations.[114, 143, 144] Rotating[25, 55, 109] and toggling[24] external fields include field frequency as a parameter to engineer colloidal assembly pathways. Moreover, rotating

magnetic fields have been used to produce micro-swimmers[145-147] and exhibit emergent collective behavior[57, 148] reminiscent of "active" systems such as rotating bacteria,[18] algae[19] and active rotors[149] of interest for clustering. Characterizing effective potentials and state diagrams of non-equilibrium particle dispersions provides a parallel to equilibrium potentials and phase behavior[150-152] in terms of designing, controlling, and optimizing new colloidal structures.[58, 153]

Rotating magnetic fields have been used to create complex colloidal arrangements and

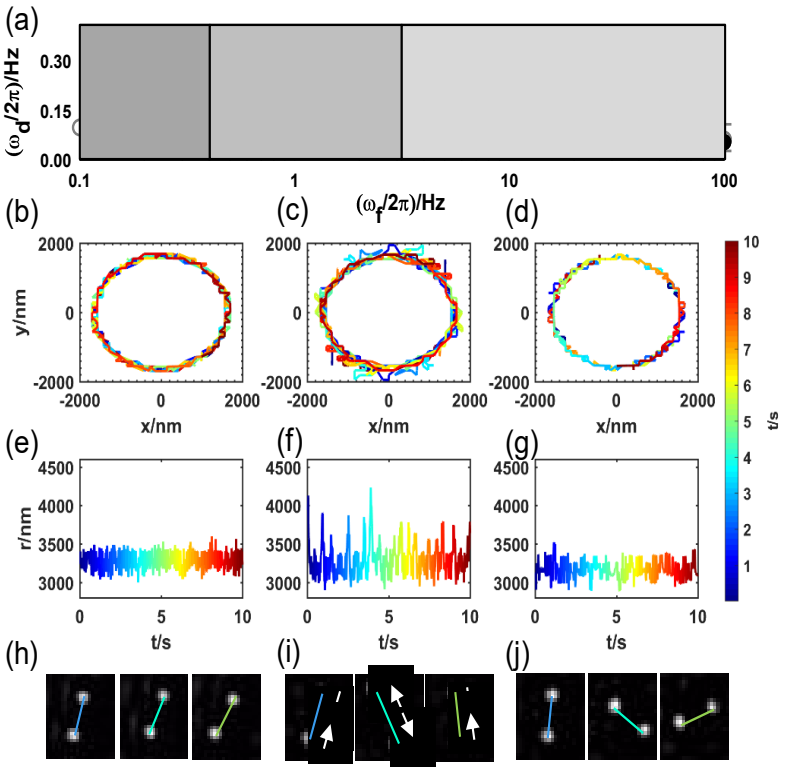

Fig. 5.1. (a) Doublet rotation vs. field frequency at 6 Gauss with experiments (open circles) and simulations (filled circles) from a previous study[1] with shaded regions indicating the low frequency, critical frequency, and high frequency regimes. The decline in rotation marks the critical regime, while the plateau is the high frequency regime. (b-d) The x, y trajectories of representative experiments of particles in rotating doublets, adjusted so the doublet center of mass is at the origin, for the three regimes: (b) 0.1 Hz, (c) 0.5 Hz, and (d) 50 Hz. (e-g) Corresponding trajectories reduced to a single dimension, the center-to-center distance, *r*. In (f), periodic increases in *r* corresponds to the excursions from the circular path in (c), while the relatively steady trajectories in (e) and (g) correspond to the circular paths in (b) and (d). Snapshots of the experiments are shown in (h-j), with lines connecting the particles that match the colored trajectories. The arrows in (i) are a guide to show how the particles periodically separate in the critical regime.

behaviors.[21, 57, 110] For the simplest case of a rotating field in a plane, it has been shown that by adjusting the field amplitude at high frequencies, quasi two-dimensional colloids can transition from a fluid to a crystal phase.[25] This phase behavior was explained by an effective interparticle attraction, which was measured experimentally from a histogram of separation distances. With enough statistics, the histogram represents the time-averaged probability distribution and can then be related to the effective pair interaction energy from a Boltzmann-like equation (*i.e.*, $p(h) \sim \exp[-u(h)]$).[154, 155] Inversion of this equation to obtain the potential from the measured probability can be referred to as an effective inverse Boltzmann analysis. The term "effective" indicates the inclusion of non-conservative forces, rather than the usual Boltzmann equation that relates probability to a scalar potential field due to conservative forces. An effective Boltzmann-like equation exists if detailed balance is satisfied.[93]

In addition to amplitude, previous work has shown the frequency of rotating magnetic fields impacts colloidal particle behavior. For example, experimental observations of fluctuating particle-particle separation, when dipolar relaxation rates are comparable to field rotation frequency, have been used to explain chain break-up in magnetorheological fluids[45] and drug delivery applications.[48] Unique frequency-dependent particle separation dynamics at lower frequencies[1, 49] indicate effective pair potentials depend on both the rotational frequency and the field amplitude. At high frequencies, pair potentials have been estimated by time-averaging over all dipole orientations by assuming the field rotates much faster than the particle's rate of Brownian motion,[133] but this assumption is not accurate at lower frequencies.

The goal of the present study is to connect particle separation dynamics in a rotating

doublet to effective interaction potentials for a range of field frequencies and amplitudes. For two particles interacting in a rotating magnetic field, their dynamics and interactions can be characterized by three regimes (Fig. 5.1). At low frequencies, the doublet rotates at the same frequency as the field and the interaction can be considered the same as it would be for a non-rotating field. Then at a critical field frequency, the average doublet rotation declines and the rotation becomes oscillatory.[49] Just past this critical frequency, particles exhibit interesting dynamics as they separate and come back together as their dipoles experience intermittent periods of alignment and misalignment with the particles' center-to-center vector.[49] In the high frequency regime, the doublet is still rotating and the particle separation distance is relatively constant.[1]

Pair potentials are often obtained from a Boltzmann inversion of measured pair distribution functions. However, unbiased sampling limits measurements to interactions on the order of the thermal energy, kT. To overcome this limitation, biased sampling in equilibrium systems has been performed by using optical tweezers in experiments, [156-158] using biasing potentials in Monte Carlo umbrella sampling simulations.[159] For example, in blinking optical tweezer experiments, trajectories are evaluated when the optical tweezer is released to obtain interaction potentials from the relationship between the transition matrix and the equilibrium solution of the Smoluchowski equation.[156, 157] In a similar set-up, forces and potentials were calculated from measurements of the mean displacement and displacement variance to determine interactions from the coefficients of the Smoluchowski equation.[160] A simulation study of "blinking" optical tweezer experiments showed that rigorous treatment of multi-dimensional and multi-body hydrodynamic interactions can influence the interpretation of conservative forces.[131] Thus, care must be

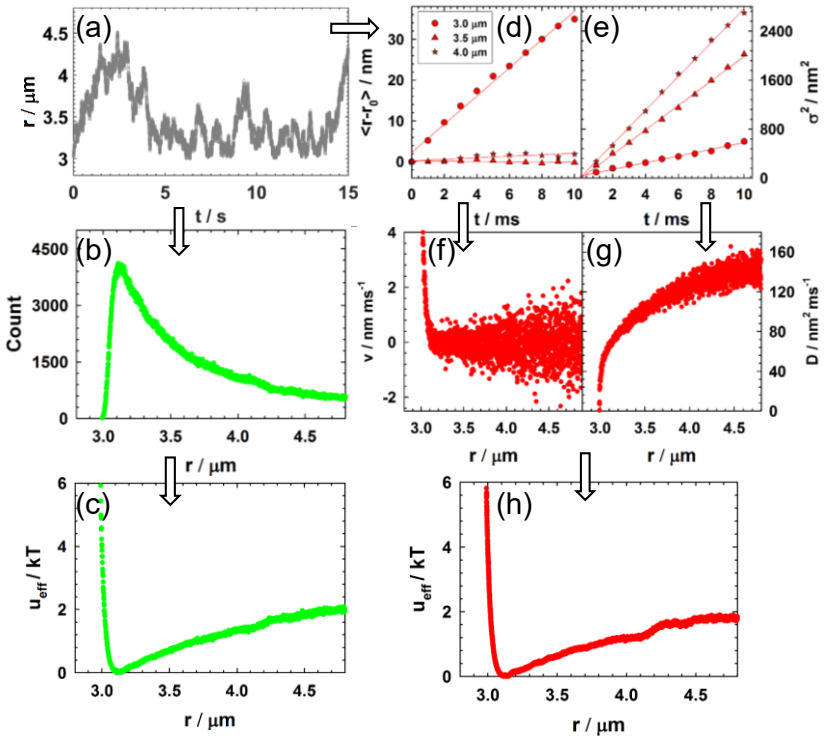

Fig. 5.2. Strategy for obtaining the potential (or effective potential) from trajectory data. Shown in (a) is a representative trajectory of particle-particle separation r in a doublet at 2 Gauss, 50 Hz. (b) The separation distances of many simulations can be binned into a histogram, which is then inverted to obtain (c) the potential from Eq. (5.18). Alternatively, the (d) displacements and (e) variances can be plotted at different distances r, 3 of which are shown as illustrative values, and then linearly fit to obtain (f) drift and (g) diffusion from Eqs. (5.11)-(5.12). The effective potential is calculated from the solution to the steady state FP equation, Eq. (5.17), setting C_1 such that the minimum energy is 0.

taken when extracting potentials from measured trajectories for equilibrium conditions. A similar analysis is appropriate when non-conservative forces (*e.g.*, hydrodynamics) also contribute to the effective pair interaction in non-equilibrium steady-state systems. For example, such analyses have been used to infer effective potentials between particle pairs during their steady-state non-equilibrium electrophoretic deposition on an electrode.[161] In this particular case, the FP equation could be solved analytically for the particle-wall and particle-particle "pseudo-potentials." Unlike the Smoluchowski equation, the FP equation makes no assumptions about the relationship between drift and conservative forces.

In the following, we report for the first time the application of the FP equation to obtain

non-equilibrium, steady-state pair potentials from simulation data. Particles experience unique tunable effective potentials vs. rotating magnetic field frequency. The displacements and variances of the interparticle separation distance, r, vs. time are fit to linear functions at short times to obtain drift and diffusivity. These quantities are then used to obtain effective potential energies, analogous to our prior treatment of equilibrium particle-surface interactions.[162] BD simulations, previously matched to single particle and doublet dynamics,[1] are used for the analysis, as the spatial and temporal resolutions needed for accurate calculations could not be obtained directly in the experiments. For certain field conditions, a "blinking" protocol was applied where an out-of-plane constant field periodically causes dipolar repulsion, which can be applied in the original magnetic quadrupole set-up. This blinking protocol could be translated to experiments for a system not limited by stringent resolution requirements. The trajectories are analyzed only when the repelling field is switched off and the field of interest in the x-y plane is turned on. Since the goal is to obtain effective steady-state potentials, unsteady trajectory data directly after the field of interest is turned on are discarded, up to an empirically determined lag time. The results are checked for accuracy against the partial curves obtained from either an inverse Boltzmann analysis (for equilibrium, non-rotating fields) or an effective inverse Boltzmann-like analysis (for non-equilibrium, rotating fields). The shapes and well-depths of the potentials demonstrate how particle interactions can be tuned by changing the field rotation frequency and amplitude.

5.2. Theory

5.2.1. Particle interactions in rotating magnetic fields

A pair of superparamagnetic colloidal particles interacting in a rotating magnetic field

of intensity H_o experience conservative, hydrodynamic, and stochastic forces, which is described in detail in our previous paper.[1] In brief, the Langevin equation for translational $\mathbf{u}$ and angular $\boldsymbol{\omega}$ velocity vectors is,[94]

$$m\frac{d\mathbf{u}}{dt} = \mathbf{F}^P + \mathbf{F}^H + \mathbf{F}^B \tag{5.1}$$

$$m\frac{d\boldsymbol{\omega}}{dt} = \mathbf{T}^P + \mathbf{T}^H + \mathbf{T}^B \tag{5.2}$$

where $\mathbf{F}$ and $\mathbf{T}$ are force and torque vectors and the superscripts correspond to conservative particle forces due to the gradient of a scalar potential field (*P)*, non-conservative hydrodynamic interactions (*H)*, and random thermal forces and torques due to Brownian motion (*B*).

The conservative forces can be calculated from partial derivatives of particle-particle and particle-wall potentials.[1] The main contribution to the particle-particle potential is the dipolar interaction. Particle 1 with dipole $\mathbf{m}_1$ interacts with particle 2 with dipole $\mathbf{m}_2$, which can be approximated by the point-dipole model as,

$$u_{dd}^{pp}\left(\mathbf{m}_1, \mathbf{m}_2, \mathbf{r}\right) = \frac{\mu_o}{4\pi r^3}\left[\mathbf{m}_1 \cdot \mathbf{m}_2 - 3\left(\mathbf{m}_1 \cdot \hat{\mathbf{r}}\right)\left(\mathbf{m}_2 \cdot \hat{\mathbf{r}}\right)\right] \tag{5.3}$$

where μ_o is the magnetic permeability. The magnetic dipole moment $\mathbf{m}$ of a particle, by the definition of superparamagnetism,[86] is

$$\mathbf{m} = \frac{4\pi a^3 \chi\left(\omega_f\right)\mu_o \mathbf{H}}{3} \tag{5.4}$$

where *a* is radius, χ is the susceptibility, and $\mathbf{m}$ can be characterized as two separate

dipoles based on the mechanisms of alignment with the field: (1) internal Néel relaxation and (2) Brownian rotation.[1] The net field is the sum of an external field and the field of a neighboring particle, separated by vector **r** as given by,

$$\mathbf{H} = \mathbf{H}_o + \mathbf{H}_p(\mathbf{r}) \tag{5.5}$$

The external field intensity is uniform and rotates with a frequency ω_f,

$$\mathbf{H}_o = H_o cos\left(\theta_f\right)\hat{\boldsymbol{x}} + H_o sin\left(\theta_f\right)\hat{\boldsymbol{y}} \tag{5.6}$$

where the time-dependence of the angle of the field components is given by $\theta_f = \omega_f t$.

In this study, the interaction of interest is the effective particle-particle potential. If particles are modeled as point-dipoles restricted to a two-dimensional (2D) plane, an effective mutual dipole model at high frequencies has been reported as,[25]

$$u_{dd}^{pp}\left(r,\theta_{mr}\right) = \frac{\mu_o m^2}{4\pi r^3}\frac{1}{\left(1-\frac{2\chi}{3}\left(\frac{a}{r}\right)^3\right)^2}\left\{1-3\cos^2\theta_{mr}+\left[\left(\frac{1-\frac{2\chi}{3}\left(\frac{a}{r}\right)^3}{1+\frac{\chi}{3}\left(\frac{a}{r}\right)^3}\right)^2-1\right]\sin^2\theta_{mr}\right\} \tag{5.7}$$

where particle dipoles are assumed to have on average the same magnitude *m* and azimuthal angle (in the x-y plane) θ_m, including both Néel and Brownian contributions, the center-to-center vector **r** has azimuthal angle θ_r, and $\theta_{mr} = \theta_m - \theta_r$ is the angle between the average dipole and **r**. All polar angles (with respect to the z-axis) are assumed to be 90º thus Eq. (5.7) implies the particles and dipoles are restricted to the 2D plane. Equation (5.7) also takes into account the neighboring dipole's contribution to the local field **H** and is

derived such that *m* in this particular equation is only the contribution from the external field ($\mathbf{H}_o$ is used in Eq. (4.20)). Previously,[25] the assumption was that this equation can be applied at high frequencies, where on average $\theta_{mr} \to 45^\circ$ or $\hat{\mathbf{m}}_i \cdot \hat{\mathbf{r}} = \sqrt{2}/2$ in Eq. (5.3) .

5.2.2. Fokker-Planck equation for steady-state, non-equilibrium doublet rotation

Experimental trajectories (Fig. 5.1) confirm that frequency-dependent particle interactions are complex and may not be found by simple approximations. The first step to solving the effective potential is to recast the multi-dimensional Langevin equation for a pair of Brownian colloids, Eqs. (4.1)-(4.2), into a one-dimensional equation of motion, reduced to a single "coarse" variable, *r*, (*i.e.*, the center-to-center distance) as

$$\frac{dr}{dt} = v^d(r) + \sqrt{D(r)}\varsigma(t) \tag{5.8}$$

where $v^d(r)$ is the deterministic drift (due to conservative forces from scalar potentials and dissipative forces from hydrodynamics) and $D(r)$ is diffusion (to be described below), and the stochastic component $\varsigma(t)$ is characterized by $\langle \varsigma(t) \rangle = 0$ and $\langle \varsigma(t)\varsigma(t') \rangle = 2\delta(t-t')$.

From the Langevin equation, there is a corresponding Fokker-Planck (FP) equation that describes the probability distribution of the system in time.[93] For the case of two particles interacting along their center-to-center distance *r*, the one-dimensional FP equation that corresponds with Eq. (5.8) is

$$\frac{\partial P(r,t)}{\partial t} = \left[\frac{-\partial v(r)}{\partial r} + \frac{\partial^2 D(r)}{\partial r^2} \right] P(r,t) \tag{5.9}$$

where the total drift coefficient $v(r)$ is related to the deterministic drift in eq. (5.8) according to the Stratonovich convention as,[93, 163, 164]

$$v(r) = v^d(r) + \frac{\partial D(r)}{\partial r} \tag{5.10}$$

where $\frac{\partial D(r)}{\partial r}$ is the noise-induced (Brownian motion) drift and $P(r,t)$ is the probability distribution of *r* in time *t*. It should be noted that the multi-dimensional Langevin equation (Eq. (4.1)-(4.2)) is fully modeled in the simulations and therefore a multi-dimensional Fokker-Planck equation could be numerically solved and then projected down to lower dimensional space. This approach would involve more complexity and would produce the same one-dimensional effective potential as Eq. (5.9) and therefore we proceed with Eqs. (5.8)-(5.9).

The drift $v(r)$ and diffusion $D(r)$ are related to the central moments of the distribution as,[65, 93, 162]

$$\begin{aligned} v(r) &= \frac{\partial \mathrm{E}[X]}{\partial t} \\ &= \lim_{\Delta t \to 0} \frac{1}{\Delta t} \left\langle \xi_i(t_0 + \Delta t) - \xi_i(t_0) \right\rangle \Big|_{\xi_k(t) = r_k} \end{aligned} \tag{5.11}$$

$$\begin{aligned} D(r) &= \frac{1}{2}\frac{\partial \sigma^2}{\partial t} = \frac{1}{2}\frac{\partial \left\{ \mathrm{E}\left[\left(X - \mathrm{E}[X] \right)^2 \right] \right\}}{\partial t} = \frac{1}{2}\frac{\partial \left\{ \mathrm{E}\left[X^2 \right] - \mathrm{E}[X]^2 \right\}}{\partial t} \\ &= \lim_{\Delta t \to 0} \frac{1}{2\Delta t} \left\{ \left\langle \left[\xi_i(t_0 + \Delta t) - \xi_i(t_0) \right]^2 \right\rangle - \left\langle \xi_i(t_0 + \Delta t) - \xi_i(t_0) \right\rangle^2 \right\} \Big|_{\xi_k(t) = r_k} \end{aligned}$$

(5.12)

where the notation $\mathrm{E}[X]$ implies expected value of a generic variable X, and the stochastic variable $\xi_k(t)$ at time *t* has the value r_k. For Eq. (5.9) to be valid, it is assumed that the process is Markovian and that the stochastic component in Eq. (5.8) is Gaussian.[65, 165] For systems at steady state, $v(r)$ and $D(r)$ are independent of time.

The FP equation can be used to solve for an effective steady state potential by setting the left-hand side of Eq. (5.9) to zero as shown,

$$0 = \left[\frac{-\partial v(r)}{\partial r} + \frac{\partial^2 D(r)}{\partial r^2} \right] P_{SS}(r) \tag{5.13}$$

The probability distribution $P_{SS}(r)$ is specified to be at steady state and is solved from Eq. (5.13) as

$$P_{SS}(r) = \frac{C}{D(r)} \exp\left[\int^{r} \frac{v(r')}{D(r')} dr' \right] \tag{5.14}$$

where *C* is a normalization constant. It should be noted that Eq. (5.14) is equivalent mathematically to

$$P_{SS}(r) = C \exp\left[\int^{r} \frac{v(r') - \frac{\partial D(r')}{\partial r'}}{D(r')} dr' \right] \tag{5.15}$$

such that the steady state effective potential can be related to $P_{SS}(r)$ from an effective Boltzmann equation[166]

$$P_{SS}(r) = C\exp\left[-u_{eff}(r)/kT\right] \tag{5.16}$$

$$u_{eff}(r)/kT = \ln\left(D(r)\right) - \int^{r} \frac{v(r')}{D(r')}dr' + C_1 \tag{5.17}$$

where C_1 is a constant. Eq. (5.16) can also be used to obtain the effective potential if a histogram of r values, $n(r)$, adequately samples the probability distribution,

$$\frac{u_{eff}(r) - u_{eff}(r_m)}{kT} = -\ln\left[\frac{n(r)}{n(r_m)}\right] \tag{5.18}$$

where r_m is the separation corresponding to the energy minimum or the most sampled r. Fig. 5.2 provides a visual guide to obtaining the (effective) potential from either the Fokker-Planck or effective inverse Boltzmann method.

5.3. Methods

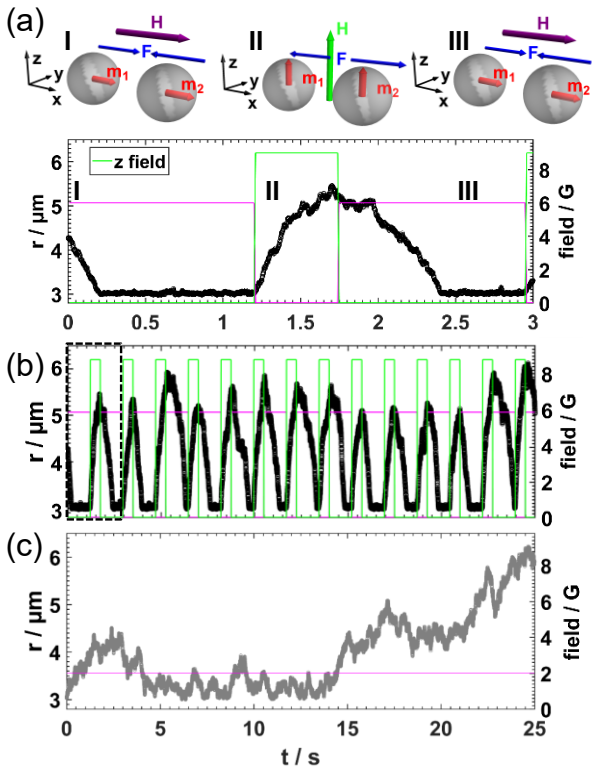

Fig. 5.3. (a) Schematic and plot (~3s) of the blinking protocol, showing the dipoles, field, and force vectors and the particle-particle separation trajectory vs. time. A 6 Gauss field is first applied in the x-direction (field of interest, magenta), along the line of centers of the particles, causing the particles to come together. Then, a 9 Gauss field is applied in the z-direction, resulting in dipole-dipole repulsion, and the particles separate. The field is once again applied in the x-direction, and the particles come together again. Dynamic data is only analyzed when the applied field of interest is on. The z-field serves to separate the particles to sample separations that are not otherwise achievable. (b) A longer (25s) BD particle-particle separation trajectory vs. time for the blinking protocol, where the outlined section of the trajectory corresponds to plot (a). (c) The trajectory of particle-particle separation in a weak, 2 Gauss, 50 Hz field in the x-y plane (field of interest, magenta), which shows that the particles sample many separations even without blinking due to the shallow effective energy well.

BD simulations of two particles were performed using the same particle properties and model as previously reported,[1] including both a Brownian and Néel dipole. In brief, the Brownian dipole has a fixed orientation within the particle, and only reorients when the particle physically rotates with respect to the x, y and z axes. The Néel dipole orients independently of the particle orientation, and follows the field vector with a frequency-dependent phase lag. The simulations also included the same particle-particle hydrodynamic interactions, with an increase in the translational resistance by 1.35 (to

approximate the effect of the wall).[1] The only exception to this was the 6 Gauss, 0 Hz (constant field) test case, for which the exact particle-particle hydrodynamic terms[96] were used in order to validate the numerical calculation of Eq. (5.12) with a known theoretical particle-particle diffusivity. The radius a of the particles is 1.4μm.

To generate enough statistics to accurately calculate drift and diffusion (Eqs. (5.11)-(5.12)), 50 BD simulations with unique trajectories (with different random number seeds, but same starting configuration) were performed for each condition, generating 50 s trajectories with a numerical integration time of 0.01 ms. All simulations started with a particle-particle separation distance of r=3.03 μm, which is based on an estimate of the energy minimum at all frequencies, determined from probability distributions of experimental data.

Table 5.1. Parameters used in the blinking protocol.

Field	t_{on} (s)	t_{lag} (s)	t_{off} (s)	B_{rep} (G)
6 G, 0 Hz	1.2	0	0.55	9
2 G, 50 Hz	4	0.7	0.5	5
6 G, 0.6 Hz	4.5	3.2	0.5	7.3
6 G, 0.8 Hz	4.5	3.0	0.5	7.3
6 G, 1 Hz	4.5	2.8	0.5	7.3
6 G, 3 Hz	3	0.7	0.8	7.3
6 G, 50 Hz	3	0.7	0.8	7.3

To facilitate adequate sampling of particle separations, a repelling field (along the z-axis) and a field of interest in the x-y plane were periodically switched on and off, controlled by a set of parameters termed the "blinking" protocol. The time that the field of interest is on, t_{on}, the lag time to ensure steady state, t_{lag}, the time that the repulsive field is

on and the field of interest is off, t_{off}, and the intensity of the repulsive field $B_{rep}=\mu_o H_z$ were determined empirically for each condition. These parameters were chosen to ensure enough sampling to characterize the full potential and are shown in Table 1. As an example, the blinking protocol implemented for the constant field case, 6 Gauss, 0 Hz, is illustrated in Fig. 5.3a-b. Because this condition is at equilibrium, t_{lag}=0 s. For a 2 G, 50 Hz field, the potential well is only a few *kT,* and it was found that blinking was unnecessary to obtain good sampling of particle-particle separations (see Fig. 5.3c and Fig. 5.2). Fifty simulation sets were also run without blinking for all cases to compare potentials calculated from an effective inverse Boltzmann analysis Eq. (5.18) to those calculated from the FP Eq. (5.17) . Drift and diffusion were calculated at discrete *r* values by fitting a linear function to displacements and variances following Eq. (5.11) and (5.12) (see Fig. 5.2). The calculations were binned in *r* with a spatial resolution of Δr and with varying temporal resolutions, Δt.

5.4. Results and Discussion

5.4.1. Constant Field

The effect of spatial and temporal resolution on linear fitting to measured displacements and variances is shown in Fig. 5.4 for a constant field (0 Hz) of 6 Gauss. Spatial and temporal resolution practically have experimental limitations, and therefore it is important to determine the lowest resolution that can still achieve the correct FP parameters. Results are shown in Fig. 5.4 for displacement and displacement variance for spatial resolutions of 1nm, 5nm, and 10nm and the points are plotted with a spacing of 0.1ms up to 3ms. It is shown that the choice of points to use in the linear fit, and hence the temporal resolution, may change the result, as the plots become non-linear past 1ms, especially for the 10nm spatial resolution. The lines shown in Fig. 5.4 are fit to the first 15

points (1.5ms).

The most efficient spatial and temporal resolution to use in the calculations of diffusivity and energy (Eqs. (5.12) and (5.17)) from data like that shown in Fig. 5.4 can be determined by checking the results against known theory for relative diffusivity[96] and potential energy (Eq. (5.3)). These comparisons are shown in Fig. 5.5b-c. As is expected, the analysis at the highest resolution of Δr=0.1nm and Δt=0.01ms captures the theory, although the analysis is computationally expensive and only a section of the curves is plotted. As shown in Fig. 5.5b-c, by changing both the spatial and temporal resolution by an order of magnitude to Δr=1nm and Δt=0.1ms, the FP analysis results still agree with the expected analytical solutions. Interestingly, if the temporal resolution is increased but the spatial resolution is kept constant, an incorrect diffusion and potential are found (the case of Δr=1nm and Δt=0.5 ms). In contrast, at Δr=5nm and Δt=0.5ms, the FP numerical

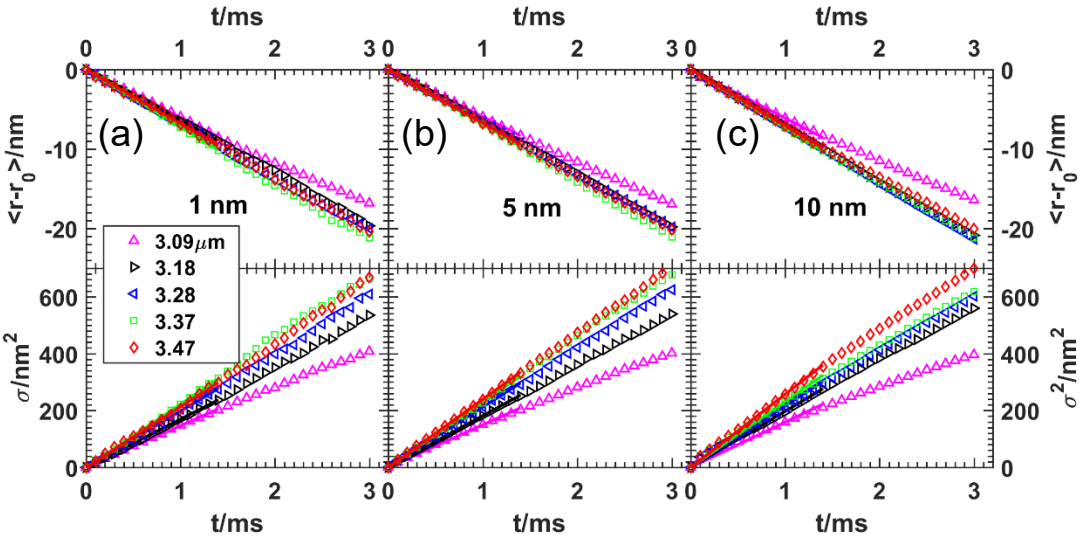

Fig. 5.4. Displacement and variance of the displacement obtained from simulations at a constant field (0 Hz) of 6 Gauss, plotted at temporal grid-points of 0.1 ms, at specific *r* values shown in the legend. The averages for 50 trajectories (open symbols) are calculated using different spatial resolutions: (a) 1 nm, (b) 5 nm and (c) 10 nm. A linear fit to the first fifteen points (1.5 ms) is plotted (solid lines).

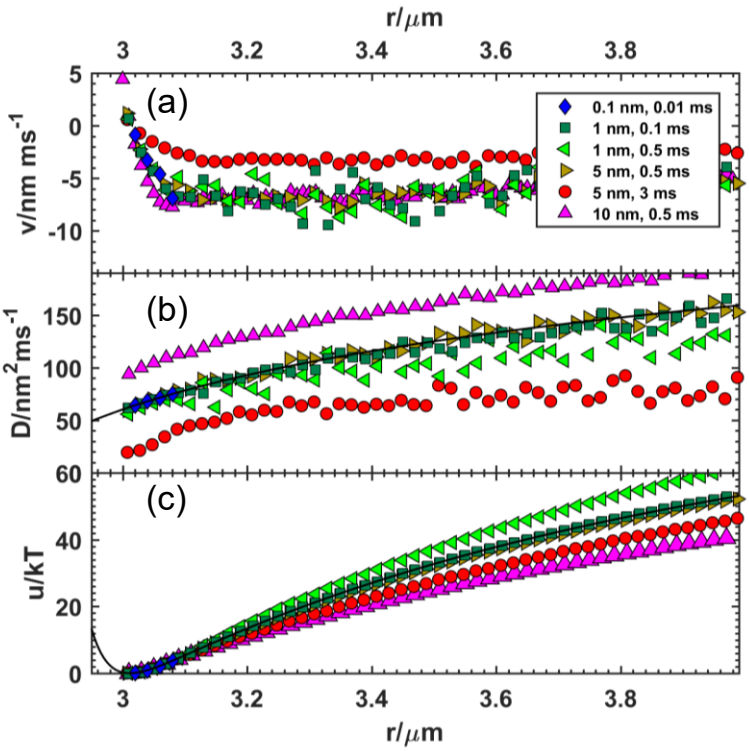

Figure 5.5. (a) Drift, (b) diffusivity, and (c) energy measured from simulated blinking experiments for a non-rotating (0 Hz) 6 Gauss field. Not all points are shown for clarity. The drift and diffusivity are calculated from linear fits to displacement and displacement variance vs. time (Fig. 5.4) using different spatial and temporal resolutions (reported in the legend). Linear fits are fit to two data points: the origin and the first point at the given temporal discrete grid (i.e. 0.01 ms, 0.1 ms, etc). The theoretical particle-particle diffusivity (solid line in (b)) is shown as well as the theoretical particle-particle potential energy in (c).

calculation is mostly accurate. Thus, spatial and temporal resolution must be modulated simultaneously. The constant field case provides a good test for the FP analysis, since at this condition the theoretical interaction potential is known beforehand. And by design, the diffusivity can be compared to the hydrodynamic terms[96] directly put into the simulation.

5.4.2. Small Amplitude Rotation Field

At 2 Gauss, a high frequency rotating field produces weak particle-particle interactions. For this condition, the FP drift, diffusion and effective potentials were generated from both non-blinking (Fig. 5.6a-c) and blinking (Fig. 5.6d-f) trajectories at different resolutions by numerically solving Eqs. (5.11)-(5.12) and (5.17). The full potential can be obtained from the effective inverse Boltzmann method, Eq. (5.18), shown on both plots, and agrees with the higher resolution FP analyses. It is clear that blinking is unnecessary to obtain the full potential, and is even worse than non-blinking due to lower statistics (in some trials, the particles drifted apart and became singlets). The effect of resolution agrees with the

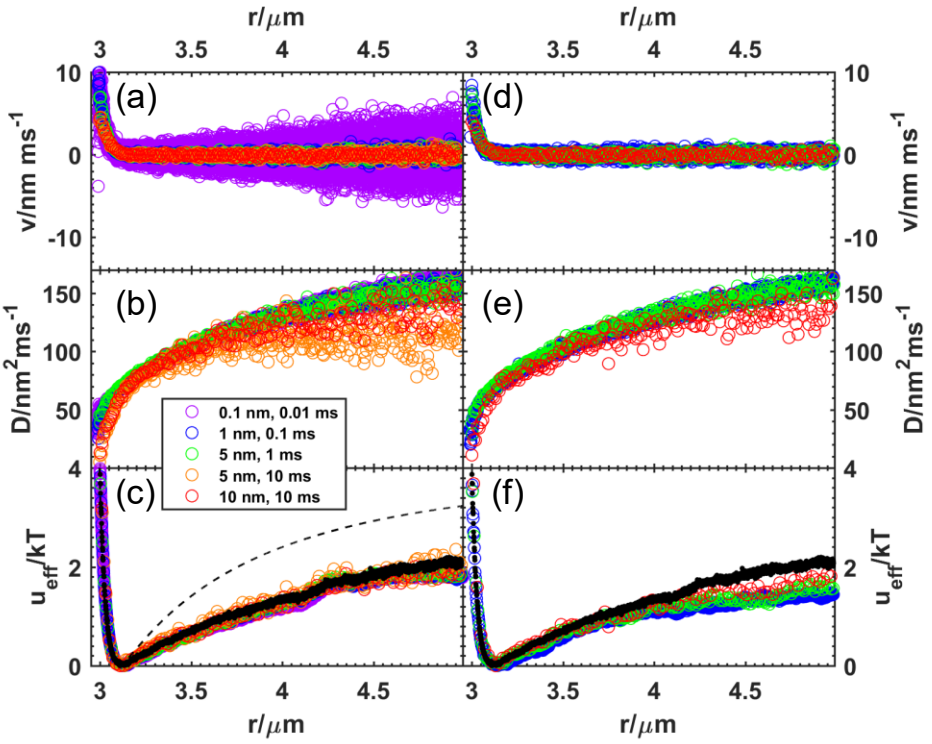

Fig. 5.6. (a,d) Drift, (b,e) diffusivity and (c,f) effective energy for 2 Gauss, 50 Hz field simulations with no blinking (a-c) and with blinking (d-f), showing a shallow energy well (~2kT). Spatial and temporal resolution values used in the FP analysis are color coded in the legend and affect the accuracy of the results beginning at 5 nm and 10 ms. By comparing the left and right-hand side plots, blinking is not necessary to capture the full energy profile, and blinking also does not agree as well past a certain separation distance (limited sampling as particles drift too far apart). The effective inverse Boltzmann (black points) method also fully captures the energy profiles. A theoretical potential using the 2D mutual dipole model (Eq. (5.7), dashed line) is plotted as a comparison. (Note the very high resolution and the second-lowest resolution are not plotted for the blinking simulations for clarity).

previous results for the constant field case in that the very high resolution is unnecessary, but a breakdown begins to occur for spatial and temporal resolutions lower than Δr=5nm and Δt=1ms.

An analytical curve is shown in Fig. 5.6c to compare the simulation results to the simplified two-dimensional theory, Eq. (5.7). The discrepancy between the theory and the simulation is most likely not because $\theta_{mr} \to 45^{\circ}$ is invalid, since we can monitor θ_{mr} and on average it is slightly less than 45° when r<3a (which has the effect of slightly increasing

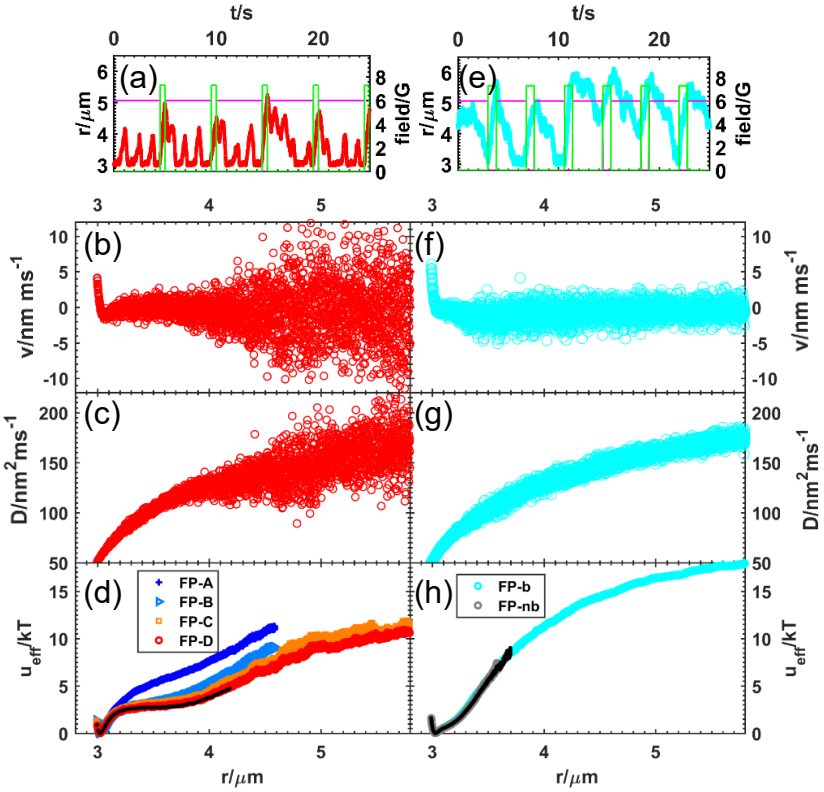

Figure 5.7. Trajectories of the blinking protocols that produce the most accurate results for 6 Gauss at (a) an intermediate frequency (0.6 Hz) and at (e) the beginning of the high frequency (3 Hz) regime. (b,f) The drifts and (c,g) diffusivities for the most optimized blinking protocols, and (d,h) the effective energies calculated from simulations with various blinking protocols. The lettered plots in (d) correspond to simulations run with blinking protocol parameters as follows; A: t_{on}=3s, t_{lag}=2.0s, B: t_{on}=3s, t_{lag}=1.5s, C: t_{on}=4.5s, t_{lag}=3.0s, and D: t_{on}=4.5s, t_{lag}=3.2s. The most accurate protocol is D (red) as it agrees with the effective inverse Boltzmann analysis (black). At 3 Hz, the blinking protocol (cyan) is t_{on}=3s and t_{lag}=0.7s, which is verified by matching the lower end of the curve with the effective inverse Boltzmann result (black), and with a FP analysis conducted on dynamic trajectories with no blinking (grey).

the potential, not decreasing it). Rather, the particles can rotate and translate in three-dimensional space and due to this Brownian motion, the dipoles and **r** may not always be restricted to the x-y plane, which effectively decreases the potential.

5.4.3. Varying Frequency

Fig. 5.7 shows blinking protocol trajectories, drifts, diffusivities, and effective potentials for a frequency just greater than the critical frequency (0.6 Hz) and for a frequency in the transition to the high frequency regime (3 Hz) at 6 Gauss. The resolutions in the FP analysis (Eq. (5.11)-(5.12), (5.17)) used to obtain these curves are Δr=1nm and Δt=0.1ms, which yield equivalent results to Δr=0.1nm and Δt=0.01ms and are conservatively chosen to be well within the resolution limitations of the analysis. In the critical regime, even without blinking, the particles separate and come back together (Fig. 5.7a) as their dipoles become misaligned with **r**. They temporarily experience intermittent repulsion until the dipoles re-align along **r** and their interaction becomes attractive again. When chosen carefully, blinking protocol parameters can capture a greater part of the potential curve than is possible even with this natural separation mechanism. However, steady state must be reached before analyzing the trajectories in order to obtain the correct effective potential.

The drift and diffusivity calculated from the most accurate blinking protocol is shown in Fig. 5.7b,c. The noise in these plots is due to the time-averaging over different conditions and poor sampling at some separation distances. Interestingly, the noise has been smoothed out for the corresponding potential curve in Fig. 5.7d (red), calculated from Eq. (5.17). Several blinking protocol potentials are shown in Fig. 5.7d. Some of the potentials become noisy for r>4.5um due to poor sampling and have been truncated. These results

demonstrate that a lag time that is long in comparison to the total interval in the on phase could lead to a less accurate effective potential due to limited sampling of the full time-averaged interaction, as is the case for protocol A compared to B. Conversely, not allowing enough lag time once the field of interest is turned on can also lead to incorrect results, as shown by comparing protocols C and D. The equivalence of the potentials from the FP and the effective inverse Boltzmann analyses confirm that the effective potential from the optimal blinking trajectory is accurate, at least up to a certain separation.

As the field frequency increases to 3 Hz, steady state is achieved at shorter times; as such, only a sub-second lag time (t_{lag}=0.7s) is needed in the blinking protocol to obtain an effective steady state potential. From prior work[1] (see Fig 5.1), 3 Hz is the frequency for 6 Gauss at which the doublet rotation is no longer in the critical regime, and the rotation rate begins to plateau. Unlike the pair potential in the critical regime in Fig. 5.7d, the potential at 3 Hz does not have any unique features, and appears to have a generic r^{-3} dependency for dipole-dipole interactions. The effective potential from the FP blinking trajectory analysis at 3 Hz agrees with the effective inverse Boltzmann results at shorter separations. A second FP analysis conducted for non-blinking ("nb") simulations (t_{on}=constant) are nearly identical to the effective inverse Boltzmann and blinking FP analysis curves, showing agreement at shorter distances as well as the utility of blinking for capturing the full potential.

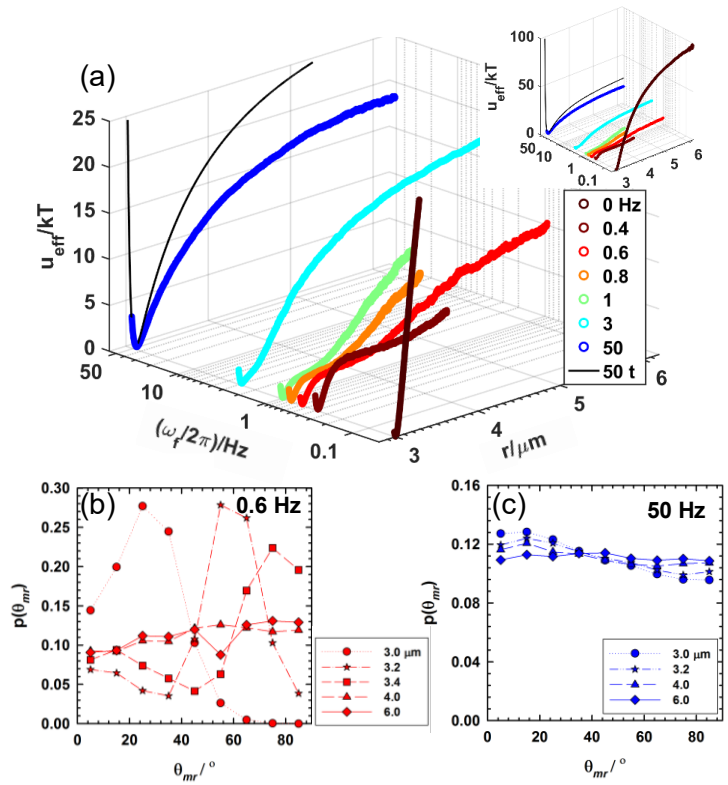

Fig. 5.8. (a) Effective energies at various frequencies in a 6 Gauss field illustrating that the potential energy well decreases by several *kT* in a rotating field once the critical regime is reached. As the field frequency increases to the high regime, the potential energy well increases, and saturates at ~18kT at the same frequencies at which the doublet rotation plateaus in Fig. 1.[1] A theoretical potential at 50 Hz ("50 t") is also plotted. The probability distribution of the angle between the average magnetic dipole **m** and **r** (b) just past the critical frequency (0.6 Hz) and (c) at a high frequency (50 Hz) case at different separations.

Fig. 5.8a summarizes effective potentials at 6 Gauss for a range of frequencies, including for a non-rotating field and for frequencies in the critical and high frequency regimes (resolutions Δr=1nm and Δt=0.1ms). The inset in Fig. 5.8a shows the same potential plots but with an energy axis from 0-100 *kT*, demonstrating how superparamagnetic particle interactions can be tuned via frequency over a couple orders of magnitude. The larger, zoomed-in plot on the scale 0-25 *kT* illustrates how the potential shapes change with frequency.

In the critical frequency regime, there are several limitations that prevent some of the potentials from being fully resolved. It was determined that blinking could not be used to

obtain the 0.4 Hz effective potential since this is the critical frequency for doublets at 6 Gauss. As such, an extended lag time of several seconds is needed to reach steady state, rendering any separation gain from blinking ineffectual. At 0.8 and 1 Hz, the lag time to reach steady state is shorter, but the effective potential is stronger than it is at 0.6 Hz, meaning that the particles come back together quicker, making sampling difficult at greater distances. Hence the potential plots are much noisier at 0.8 and 1 Hz for separations >4um than they are for 0.6 Hz. At the transition from the critical to the high frequency regime, as noted in Fig. 5.7e-h at 3 Hz, the full potentials can be reliably measured. The fact that the potentials are similar at 3 Hz and 50 Hz demonstrates that the interaction potential is essentially the same once the high frequency regime has been reached (in conjunction with a plateau in doublet rotation rate, Fig. 5.1). A theoretical potential is also plotted at 50 Hz, Eq. (5.7). This equation overestimates the potential, again due to the assumption that the particles and dipoles remain in the plane, which was seen for 50 Hz at 2 Gauss (Fig. 5.6).

We also explore the angle between the dipoles and **r** by tracking θ_{mr} as a function of separation distance. At 50 Hz, the assumption that on average $\theta_{mr} \to 45^{\circ}$ is accurate, as can be seen in Fig. 5.8c; the probability distribution of all angles is relatively flat, or the average is 45°. At the shorter distances, the average is less than 45°, which would increase the potential relative to Eqn. (5.7), but not enough to overcompensate for the decrease as a result of Brownian translation and rotation out of the x-y plane. However, three-dimensional motion plays a lesser role at 6 Gauss than at 2 Gauss because of the stronger dipole-field and dipole-dipole forces in the x-y plane. The shapes of the curves in the critical regime can also be understood from the probability plot of θ_{mr} at different *r* values

for 0.6 Hz (Fig. 5.8b). When the particles are close together, θ_{mr} is much less than the crossover angle from attractive to repulsive (that occurs at $\sim 55^{\circ}$) (see Eq. (5.3)), meaning the attraction is strong, but at intermediate distances, r≈3.3um, the particles are on average repelled since θ_{mr} is greater than the crossover angle. The probability distribution of θ_{mr} flattens as the particles become farther apart, meaning $\theta_{mr} \to 45^{\circ}$ on average at greater separations.

5.5. Conclusions

Here we reported a Fokker-Planck trajectory analysis to obtain the drifts, diffusivities, and effective pair potentials between particles for non-equilibrium, steady-state conditions in rotating magnetic fields. A new blinking field strategy was applied to separate particles to obtain better sampling of particle separation distances. The accuracy of measured potentials was highly dependent on the spatial and temporal resolutions used in the numerical analysis; this was confirmed by comparing with known potentials for a constant field case, and against an effective inverse Boltzmann analysis of unbiased sampling of energy wells. The unique shapes and depths of the resulting interaction potentials, particularly at the intermediate frequencies where dependencies on *r* do not follow a common power law relationship, correlate to the doublet rotation dynamics from previous experiments.[1] As such, the qualitative behavior of the interactions between superparamagnetic micron particles can be inferred merely by noting the critical and high frequency regimes at different field magnitudes. Frequency could be intelligently utilized for engineering colloidal assembly as a tuning "knob" to melt and condense systems to eliminate defects and achieve desired structures. In addition, the reported measurement strategy and analysis employing the FP equation is general and could be applied to obtain

effective potentials in “active” and other non-equilibrium systems.

6. DYNAMICS AND FREE ENERGIES OF NON-EQUILIBRIUM COLLOIDAL CHAIN FOLDING AND ASSEMBLY IN A ROTATING MAGNETIC FIELD

Simulations and experiments are reported of small cluster colloidal particle assembly in nonequilibrium rotating magnetic fields at several field frequencies and amplitudes. The simulations capture the kinetics as well as the favored structures (thermodynamics) observed in the experiments and can be used to determine which physics are most important in the system. The assembly process is characterized by two order parameters, such that the system can be modeled using the low-dimensional Langevin and Fokker-Planck (FP) equations. Trajectories of the high-dimensional simulation data are converted to these order parameters, and then the diffusivity landscapes and effective potentials in order parameter space are numerically calculated from the FP equation. The resulting low-dimensional landscapes are then used to conduct low-dimensional Langevin dynamics simulations, which were compared to the higher-dimensional experiments and simulations via first passage times. Agreement across all three sets of data show that the main dynamic modes are well represented by coarse-graining. In addition, the results illustrate how nonequilibrium fields can be exploited to design efficient assembly pathways and to tune particle interactions and morphologies.

6.1. Introduction

The study of micron-sized colloidal particles interacting under non-equilibrium external fields has applications in particle assembly for photonic crystals,[152, 167] creating and understanding active particle systems,[168-170] examining and visualizing unique phase behavior,[19, 171, 172] and modeling diverse systems in nature.[18, 51] Knowledge of the

dynamics, free energies and particle interactions associated with the application of an external field can inform the efficient design of assembly policies[58] and lab-on-chip biotechnological devices.[173] In contrast to equilibrium systems, dissipative forces play a crucial role on observed time scales and structures in non-equilibrium.[114, 174] For example, hydrodynamics influence doublet rotation,[1] chain folding[51] and clustering[175] in rotating magnetic fields, similar to trends important in protein folding.[176] Dissipative forces lead to steady state "pseudo potentials," or effective nonequilibrium energies beyond those derived solely from conservative forces.[177, 178]

For the case of magnetic fields, particles form chains under the application of a constant field, then experience bending[44] and breaking[179] when the field rotates in a two-dimensional plane, until a steady state is reached. The chain collapse process has been studied in the context of magnetorheological fluids[52] and biomolecular sensors,[180] and separate studies have also been conducted on the final configurations of colloidal particles[25, 53] in rotating magnetic fields. A logical next step would be to connect the dynamics of chain collapse, assembly pathways, and the favored steady state structures comprehensively, analogous to reports on cluster assembly in electric fields[181, 182] and with depletion attraction.[67] Further motivating such a study, the dynamics and energies of small cluster formation in colloidal systems are of interest for understanding ensemble phenomena at macroscopic levels.[183]

In order to quantify high-dimensional behavior, low-dimensional order parameters (a.k.a. reaction coordinates) have been employed in equilibrium systems to describe signature dynamics and structures. For example, radius of gyration, *Rg*, captures condensation, while orientation order parameters describe ordering and grain boundary

formation in colloidal particle assembly in an electric field.[184] Likewise, protein folding has been described by the number of native contacts and free energy[64] and micelle formation can be characterized by cluster size.[65] Finding physically-relevant low-dimensional parameters that accurately capture high-dimensional dynamical processes is a complex task. Some inroads have been made to use sophisticated techniques such as diffusion mapping to determine the number of parameters needed,[68] although the results merely serve as a guide for the actual selection of appropriate parameters.[70, 185] Assuming suitable order parameters are found, the high-dimensional Langevin and corresponding Smoluchowski equation can be reduced to a low-dimensional set of equations. Previous work demonstrated how drifts, diffusivities, and free energies in order-parameter space can be extracted from dynamical data via Bayesian inference[20] or linear fitting displacements and displacement variances,[70] both for colloidal systems at equilibrium where the Smoluchowski equation applies.

There has been some precedent for describing the time evolution of non-equilibrium particle assembly through coarse-graining, for example for particles in an oscillating pH solution,[178] active particles in kinetic Monte Carlo simulations,[186] simulations of opposing rotating spinners,[187] and simulations and experiments of magnetic particle wire length growth at an air-liquid interface.[188] Statistical mechanical principles can be applied to non-equilibrium colloidal structures in high dimensions to find effective potentials, as was theoretically shown.[189] However, the determination of effective energies in order parameter space for colloidal systems has been limited to the case of pair interactions,[177, 190, 191] as far as we are aware. Beyond the colloidal literature, the low-dimensional modeling strategy

under nonequilibrium conditions has been used to describe viscoelastic fluids [66] and quantum fields.[192]

Here we report the first course-graining of a nonequilibrium system to solve the steady state Fokker-Planck (FP) equation for diffusivity and effective energy landscapes. The FP equation is more general than the Smoluchowski equation in that it does not assume drift is directly related to conservative forces.[93] The results describe magnetic colloidal chain folding and assembly as a function of field amplitude and frequency for system sizes of 4, 7 and 13 particles, building from our previous work with one and two particles.[1, 193] High dimensional Stokesian Dynamics (SD) (multi-body hydrodynamics) simulations are carefully matched to experimental trajectories across all three system sizes and at four different field conditions. Like the 2-particle case, emergent collective hydrodynamic interactions are crucial to modeling the particle assembly, as preliminary BD simulations that only included pair-wise hydrodynamics did not show quantitative or even qualitative agreement with experiments. The key features of the assembly process are condensation and asymmetric chain folding, the former of which can be described by radius of gyration. A second order parameter, which is an angle related to the first and second moments of the gyration tensor, was developed to describe the latter. The suitability of the order parameters to describe the various experimental results is assessed by comparing first passage time distributions of the experiments with those from SD and low dimensional Langevin dynamics (LDLD). The diffusivities and effective potentials show how chain folding pathways as well as steady state structures can be tuned in rotating magnetic fields.

6.2. Theory

6.2.1. Equation of Motion

The high-dimensional equation of motion for many particles that describes translational and rotational velocity vectors $\mathbb{u}$ and $\boldsymbol{\omega}$ along all three axes is the Langevin equation, which was previously reported for the two-particle case[1] and is reproduced here as shown,

$$m\frac{d\mathbf{u}}{dt} = \mathbf{F}^P + \mathbf{F}^H + \mathbf{F}^B \tag{6.1}$$

$$m\frac{d\boldsymbol{\omega}}{dt} = \mathbf{T}^P + \mathbf{T}^H + \mathbf{T}^B \tag{6.2}$$

where m is particle mass, and force and torque contributions are derived from scalar potentials (*P*), hydrodynamics (*H*) and Brownian motion (*B*). Particle positions are then numerically calculated by solving eqs. (6.1) and (6.2) for particle position and orientation, in identical form to our previous work,[1]

$$\mathbf{r}_l = \mathbf{r}_l^0 + \sum_j \frac{\partial \mathbf{D}_{lj}^0}{d\mathbf{r}_j}\Delta t + \sum_{j,j\le 3N} \frac{\mathbf{D}_{lj}^0(\mathbf{F}_j^{P,0} + \mathbf{F}_j^B)}{k_B T}\Delta t + \sum_{j,j>3N} \frac{\mathbf{D}_{lj}^0(\mathbf{T}_j^{P,0} + \mathbf{T}_j^B)}{k_B T}\Delta t \tag{6.3}$$

$$\mathbf{n}_l\left(t+\Delta t\right) = \mathbf{n}_l\left(t\right) + \left[\left(\sum_{j,j>3N} \frac{\mathbf{D}_{lj}^0}{kT}\left(\mathbf{T}_j^{P,0} + \mathbf{T}_j^B\right) + \sum_{j,j\le 3N} \frac{\mathbf{D}_{lj}^0}{kT}\left(\mathbf{F}_j^{P,0} + \mathbf{F}_j^B\right)\right)\right] \times \mathbf{n}_l\left(t\right)\Delta t \tag{6.4}$$

where, $\mathbf{F}_j^{P,0}$ and $\mathbf{T}_j^{P,0}$ are the force and torque vectors at the start of each step, $\mathbf{F}_j^B$ and $\mathbf{T}_j^B$ are the random force and torque vectors, **n** is the unit orientation vector, k_B is Boltzmann's constant, T is temperature, l is particle number, and j is particle coordinate such that $j \le 3N$ indicates translational coordinates and $j > 3N$ is rotational coordinates.

6.2.2. Conservative Forces and Torques

The conservative forces and torques in eqs. (6.1)-(6.2) are gradients of scalar potentials, which include the dipole-field interaction, electrostatic particle-particle and particle-surface interaction potentials, and the gravitational potential, as described in our previous paper.[1] The remaining scalar potential is the magnetic interaction between particles, which was previously described by the point-dipole model. Although the point-dipole model is a popular equation to approximate multipolar superparamagnetic particles,[1, 25] it becomes less accurate in many-body systems as particles approach each other.[87] To achieve some improvement beyond the point-dipole model without introducing the complexity of three-body interactions, exact pair potentials were calculated by solving the three-dimensional Laplace equation in COMSOL Multiphysics (see Methods).

6.2.3. Hydrodynamics and Brownian Forces

Forces from hydrodynamics and Brownian motion are intrinsically connected by the fluctuation-dissipation theorem[95, 194] that states that the variance of random forces is proportional to the resistance. In multi-body systems, the resistance matrix that accounts for multi-body hydrodynamic interactions between particles as well as an underlying surface is given as,[29, 195]

$$\mathbf{R} = \left(\mathbf{M}^{\infty}\right)^{-1} + \mathbf{R}_{PP} + \mathbf{R}_{PW} - \mathbf{R}_{PP}^{\infty} - \mathbf{R}_{PW}^{\infty} \tag{6.5}$$

where $\mathbf{M}^{\infty}$ is the mobility matrix of the far-field pair interactions, which when inverted, becomes a far-field multi-body resistance matrix. The remaining near-field (lubrication) interactions can be accounted for indirectly by adding exact pairwise particle-particle interactions ($\mathbf{R}_{PP}$),[196] and exact particle-wall interactions ($\mathbf{R}_{PW}$),[197-199] and then subtracting

the far-field particle-particle ($\mathbf{R}_{PP}^{\infty}$) and particle-wall ($\mathbf{R}_{PW}^{\infty}$) interactions as they are already included in **M**.

The diffusivity matrix is related to the resistance matrix by $\mathbf{D} = k_B T / \mathbf{R}$. Brownian forces and torques can be combined into one vector,

$$\mathbf{S}^B = \begin{pmatrix} \mathbf{F}^B \\ \mathbf{T}^B \end{pmatrix} \tag{6.6}$$

which follows a Gaussian distribution with mean zero and variance

$$\left\langle \mathbf{S}_i^B(0)\mathbf{S}_j^B(t) \right\rangle = 2(kT)^2 \mathbf{D}_{ij}^{-1}\delta(t) \tag{6.7}$$

6.2.4. Order Parameters

Two order parameters are chosen to capture the main dynamic modes observed in the chain folding and assembly process. Radius of gyration describes the compression of the particles in the *x*-*y* plane, and is calculated as,[200]

$$Rg/a = \frac{1}{2N}\left[\sum_{i=1}^{N}\sum_{j=1,j\neq i}^{N}\left(x_i - x_j\right)^2 + \left(y_i - y_j\right)^2\right]^{0.5} \tag{6.8}$$

where *N* is the number of particles.

In previous work studying multiple colloidal particles in an external field, ordering was a key feature along the pathway to assembly,[20] but in the rotating magnetic field system, ordering of the particles in a hexagonally closed-packed arrangement almost always occurs and is therefore not of interest. The asymmetric chain folding is a key feature of the assembly and is unique to this particular method to form quasi-two-dimensional colloidal

crystals. A new order parameter, called A, was developed that measures the degree of "folding" by first setting a reference axis for each particle by minimizing the angles (arctan) with all other particles with respect to that reference axis. By then finding the average of the average angle for each particle, a new order parameter is defined,

$$A_i = \left(N-1\right)^{-1} \min\left[\sum_{j,i\neq j}^{N} \arctan\left(\frac{\left|y_i - y_j\right|}{\left|x_i - x_j\right|}\right)\right] \tag{6.9}$$

$$A = N^{-1}\left[\sum_{i}^{N}\left(A_i\right)\right] \tag{6.10}$$

This angle order parameter A can be thought of as related to the x and y principal moments of the gyration tensor. A is reported in degrees, and has a limit of zero for particles in a straight chain and 45º for an infinitely large system (where angles ranging from 0º to 90º average out to 45º).

6.2.5. Low Dimensional Langevin and Fokker-Planck Equations

The high-dimensional Langevin equation introduced in eqs. (6.1)-(6.2) can be reduced to a low-dimensional equation that describes the motion of vector $\mathbf{X}$, where $\mathbf{X} = \left\{Rg/a, A\right\}$, as

$$\frac{d\mathbf{X}}{dt} = \mathbf{v}^d\left(\mathbf{X}\right) + \mathbf{g}\left(\mathbf{X}\right)\boldsymbol{\varsigma}\left(t\right) \tag{6.11}$$

where $\mathbf{v}^d\left(\mathbf{X}\right)$ is the determinist drift, $\mathbf{g}\left(\mathbf{X}\right)$ is related to the diffusivity matrix as

$$D_{ij}\left(\mathbf{X}\right) = g_{ik}\left(\mathbf{X}\right)g_{jk}\left(\mathbf{X}\right) \tag{6.12}$$

and $\boldsymbol{\varsigma}\left(t\right)$ is a vector of Gaussian random variables with mean and variance as follows,[93]

$$\begin{aligned}\left\langle \varsigma_i(t)\right\rangle &= 0\\ \left\langle \varsigma_i(t)\varsigma_j(t')\right\rangle &= 2\delta_{ij}\delta(t-t')\end{aligned} \tag{6.13}$$

The corresponding Fokker-Planck equation that describes the probability evolution of the order parameter vector based on eq. (6.11) is

$$\frac{\partial P(\mathbf{X},t)}{\partial t} = \left[\frac{-\partial \mathrm{v}_i(\mathbf{X})}{\partial \mathrm{X}_i} + \frac{\partial^2 \mathrm{D}_{ij}(\mathbf{X})}{\partial \mathrm{X}_i \mathrm{X}_j}\right] P(\mathbf{X},t) \tag{6.14}$$

where the drift vector v_i is related to the deterministic drift and diffusivity in eq. (6.11) by the following relationship,[166]

$$\mathrm{v}_i = \mathrm{v}_i^d + g_{kj}\frac{\partial g_{ij}}{\partial X_k} \tag{6.15}$$

At steady state, eq. (6.14) reduces to

$$0 = \left[\frac{-\partial \mathrm{v}_i(\mathbf{X})}{\partial \mathrm{X}_i} + \frac{\partial^2 \mathrm{D}_{ij}(\mathbf{X})}{\partial \mathrm{X}_i \mathrm{X}_j}\right] P_{SS}(\mathbf{X}) \tag{6.16}$$

where the steady state probability distribution of **X** can be related to an effective free energy, analogous to an effective pair potential,[193]

$$P_{SS}(\mathbf{X}) = C_1 \exp\left[u_{eff}(\mathbf{X})/k_B T\right] \tag{6.17}$$

where C_1 is a normalization constant. By solving eq. (6.16), which is a first order ordinary differential equation, and substituting in eq. (6.17), we can find the effective potential as a function of drift and diffusivity,[93]

$$u_{eff}(\mathbf{X})/k_B T = \int_{\mathbf{X}} \left(D^{-1}\right)_{ij}\left(\frac{\partial D_{jk}}{\partial X_k} - v_j\right) + C_2 \tag{6.18}$$

where C_2 is a constant.

To find the effective potential, high-dimensional trajectory data is converted to the lower-dimensional order parameters. Then, the drift vector and diffusivity matrix in order parameter space are numerically calculated by linear fits to displacements and displacement variances of the order parameters, as shown by the following equations,

$$v_i(\mathbf{X}) = \lim_{\Delta t \to 0} \frac{1}{\Delta t} \left\langle \xi_i(t_0 + \Delta t) - \xi_i(t_0) \right\rangle \Big|_{\xi_k(t) = X_k} \tag{6.19}$$

$$D_{ij}(\mathbf{X}) = \lim_{\Delta t \to 0} \frac{1}{2\Delta t} \begin{Bmatrix} \left\langle \left[\xi_i(t_0 + \Delta t) - \xi_i(t_0) \right] \left[\xi_j(t_0 + \Delta t) - \xi_j(t_0) \right] \right\rangle \\ - \left\langle \xi_i(t_0 + \Delta t) - \xi_i(t_0) \right\rangle \left\langle \xi_j(t_0 + \Delta t) - \xi_j(t_0) \right\rangle \end{Bmatrix} \Big|_{\xi_k(t) = X_k}$$

(6.20)

The gradient of the effective potential, from eq. (6.18), and the diffusivity matrix, eq. (6.20), can then be inserted into a Langevin dynamics equation, similar to the construction of eqs. (6.3)-(6.4), which characterizes the trajectory of the system in order-parameter space (analogous to the equilibrium version[70]),

$$\mathbf{X}(t + \Delta t) = \mathbf{X}(t) - \frac{\mathbf{D}}{k_B T} \cdot \nabla u_{eff} \Delta t + \nabla \cdot \mathbf{D} \Delta t + \sqrt{2\mathbf{D}\Delta t}\,\xi \tag{6.21}$$

where ξ is a stochastic variable with mean zero and variance one. The diffusivity matrix in eq. (6.20)-(6.21) is a 2x2 matrix with the following elements,

$$\mathbf{D}(\mathbf{X}) = \begin{bmatrix} D_{RgRg} & D_{RgA} \\ D_{ARg} & D_{AA} \end{bmatrix} \tag{6.22}$$

where $D_{RgA} = D_{ARg}$. The above eqs. (6.11)-(6.21) are introduced where $\mathbf{X}$ is a two-element vector, but they could easily be simplified to the one-dimensional (1D) cases: $X = Rg / a$ and $X = A$.

6.3. Materials and Methods

6.3.1. Experimental

M-270 carboxylic acid-coated microparticles composed of iron oxide nanoparticles embedded in a polystyrene matrix with nominal diameter 2.8um were used as received (Dynabeads, Life Technologies). Experiments were conducted on glass coverslips (Gold Seal, Corning). To prepare the coverslips, they were first sonicated in Acetone (Sigma-Aldrich Company) and then Isopropanol (Sigma-Aldrich Company), and soaked in Nochromix (Godax Laboratories) for 1-24 hours, rinsed in deionized water, sonicated in 0.1M KOH for 35 minutes to charge the surface, rinsed with deionized (DI) water, and dried with nitrogen gas. Sample cells containing dilute particles in 0.1mM NaCl were prepared by dispensing the dispersion into Viton o-rings (McMaster Carr) coated with vacuum grease on coverslips/slides and sealed using epoxy quickset glue (Loctite) and a top coverslip.

The particles were visualized under a 100x oil objective (Nikon) with either a 1.5x or 1.0x magnification. A Photron PCI-512 camera was used to record video at 60 frames per second (fps) of the field of view of the microscope. Coverslips with the colloidal particles were placed on a stage in the center of a magnetic field set-up that has 8 solenoids stacked in a quadrupole configuration.[101] A LabView code interfaces with the solenoids to control the current through each solenoid, creating a directional but uniform field in the

center of the quadrupole. The applied current is calibrated with the field strength in Gauss using a gauss meter.

Groups of 4, 7 and 13 particles were identified and isolated from other neighboring particles by allowing them to diffuse away or by applying an out-of-plane field in the z-direction that causes the particles to repel. Initially, an applied field is set in a constant,

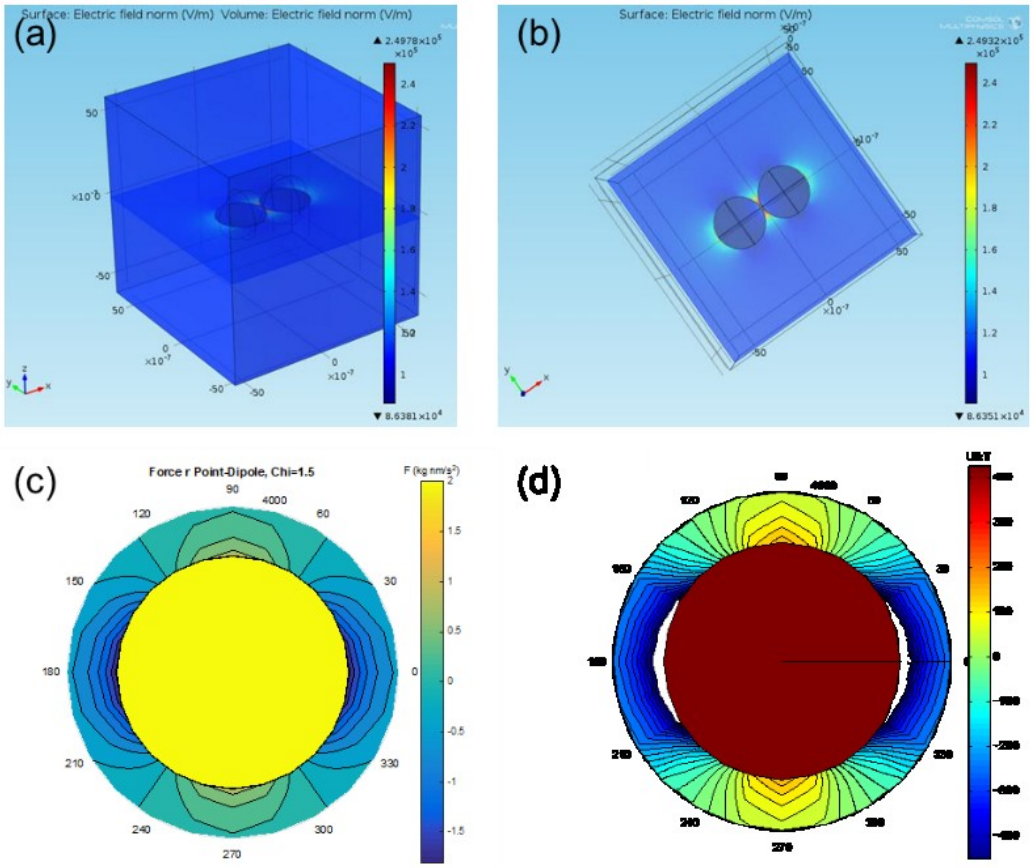

Figure 6.1: COMSOL simulation results used to calculate the exact particle-particle interactions as a function of distance and angle. (a) Example of one simulation where the spherical particles are situated in the middle of a box, and the electric field (analogous to a magnetic field through a simple conversion) is plotted throughout the box, showing that in this particular case, the applied field is aligned with the center-to-center vector **r**. (b) a top-down view of the same results shown in (a). (c) A polar plot showing the force, calculated via the Maxwell stress tensor, up to a distance of r=4000nm (where $2a$=2800nm) on a single particle as a function of distance and angle of a second particle (not shown) where the dipole is parallel to the x-axis. (d) The force plot converted to energy, showing that the lowest energy position is for a second particle to form a chain with the first particle along the x-axis.

non-rotating mode to cause the group of particles to form a chain. Then, the rotating magnetic field is applied and the video is recorded. The recording is stopped when the particles appear to be stable in one configuration or when their sampling of several configurations does not significantly change. Trials included applied rotating fields of 6 Gauss 0.8 Hz, 6 Gauss 50 Hz, 4 Gauss 0.4 Hz and 4 Gauss 50 Hz. At least 20 trials were conducted for each of the three system sizes and at all four field conditions. Videos were analyzed using particle tracking codes written in FORTRAN, adapted from the classic particle tracking strategy.[102] The x and y trajectories of the particles were then used to calculate the order parameters Rg and A, defined in eqs. (6.8)-(6.10). To show particle orientation as well as position, some videos were captured of particles that had a non-magnetic, asymmetric coating (called "optical janus" particles[1]) to generate qualitative data of individual particles rotating as part of a rotating chain.

6.3.2. Particle Interaction Modeling in COMSOL

COMSOL was used to solve the three-dimensional Laplace equation for the force between two superparamagnetic particles in an external field as a function of orientation of the field with respect to the center-to-center vector, **r**, and the magnitude of the inter-particle distance, r. The electrostatics package in COMSOL was used, but the equations are analogous to magneto-statics via a simple conversion. Figure 6.1a-b shows a representative graphic from COMSOL with two spheres in the simulation box.

Two spherical particles are situated in the center of a box while boundary conditions on the box define the applied electric field. The particle electric permittivity, analogous to the magnetic permeability, used in the simulation represents an effective magnetic static susceptibility of χ_o=1.5. Static simulations were systematically conducted by changing the

distance between particles, *r,* as well as the angle of **r** with respect to the field direction. Then, the force that particle one experiences due to the presence of particle two is calculated by integrating the Maxwell surface stress tensor over the surface of particle one, which is a built-in calculation in COMSOL. Note that for paramagnetic particles in static fields, the field direction is the same as the dipole direction, hence this angle is later used in SD simulations as the angle between **r** and the average dipole (the average being over the Néel and Brownian dipoles[1] over both particles).

A two-dimensional (distance and angle) look-up table was developed from the calculated forces between the particles from the COMSOL results (see the forces and energies in Figure 6.1b-c). Although a simple scaling factor can be used to adjust the forces with change in field magnitude, there is no direct dependence on how to scale for χ_o.[87] However, the susceptibilities used in this study are close to 1.5, and thus a rough scaling of χ^2_o was used to extrapolate from the look-up table. The point-dipole model and the COMSOL solution converge as the distance between particles increases. As such, in the SD simulations (details below), the forces between particles are calculated via interpolation from the look-up table only when the distance between particles is less than 2.86*a*. When $r>2.86a$, the point-dipole equation is used instead.

6.3.3. Stokesian Dynamics Simulations

Stokesian Dynamics simulations were conducted in FORTRAN to solve eqs. (6.3)-(6.4) with a time step size of 0.01ms. To model the experiments, 50 simulations were conducted of 4, 7 and 13 particles, with initial configurations of a straight chain. Initial distances between particles was 2.165*a*, an approximation of the potential energy minimum

for all conditions.[193] Initial dipole orientations were always parallel to the chain axis. The 4 particle simulations recorded particle positions for a time period of 200s, while the 7 and 13 particle simulations ended after 260s.

The particle magnetic properties used in the simulation were based on the same general model for dynamic magnetic susceptibility that was previously implemented for single particle and doublet simulations.[1] However, two parameters were fine-tuned to better fit the experimental data to take into account the different particle-particle interaction as compared to our previous paper (exact solution in COMSOL vs. dipole-dipole) as well as magnetic multi-body affects. A superposition of pair interactions is inherently not accurate due to the long-range nature of the interactions, however, the particle parameters can be fit in the simulations to better reflect the experimental data within the constraints of the pair-wise modeling. Specifically, the dynamic Néel susceptibility, χ_N, and the Néel dipole phase lag, $\theta_{lag,\mathrm{N}}\left(\omega_f\right)$, unique for each field condition, were determined by comparing mean first passage times in *Rg* and *A* of the 20+ experiments per system to those of "trial" simulation sets (50 simulations in each set). The parameters (χ_N and $\theta_{lag,\mathrm{N}}$) used in the trial simulation sets that had the best agreement across all three system sizes were then used in the SD simulations presented throughout the paper. To take into account variation in magnetic particle properties across individual particles, pair interactions were adjusted by sampling χ_N and $\theta_{lag,\mathrm{N}}$ from gaussian distributions with the best fit parameters as the means and with normalized standard deviations of ~0.08. Additional (+~50) SD simulations were conducted for each case at different starting configurations to generate enough statistics to accurately calculate energy landscapes.

Table 6.1: The resolutions or binnings used to numerically calculate drift, diffusivity and effective free energy for the two different order parameters, following eqs. (6.18)-(6.20).

N	***ΔRg/a***	***ΔA***
4	0.04	0.8
7	0.05	0.8
13	0.1	0.8

6.3.4. Low Dimensional Langevin Dynamics

Low-dimensional Langevin dynamics (LDLD) simulations, eq. (6.21), were conducted in FORTRAN using the diffusivity matrix and the scalar effective potential calculated from simulation trajectory data (eq. (6.18)-(6.20)). Specifically, the drifts and diffusivities were determined by linear fitting the average displacement and displacement variances with time of *Rg* and *A* from the SD simulations at specific grid values of the order parameters. The temporal resolution (Δt) used in the linear fitting, which are numerical approximations to eq. (6.19)-(6.20), was 1ms. The spatial resolutions used to bin/grid the two order parameters were unique to each system size, and are displayed in Table 6.1. Because the spatial and temporal resolutions are much higher than what is possible in experiment, the experimental data was not used to calculate the drifts, diffusivities, and hence effective potential energies, although they were fit to simulations beforehand, similar to our previous strategy for determining effective pair potentials from simulations.[193]

6.4. Results and Discussion

6.4.1. Modeling Chain Folding and Assembly

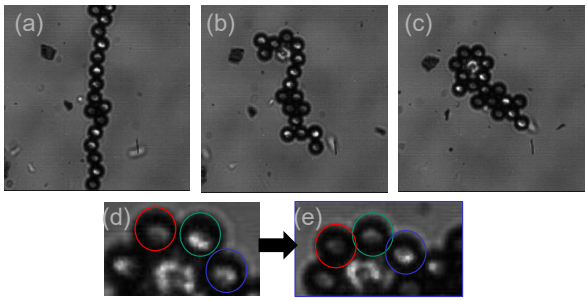

Figure 6.2: Snapshots of an example experimental video of optical janus particles folding into a condensed structure, showing that as the particles assemble, the individual particles within the chain, in addition to the cluster itself, are rotating. The conditions in this video are 10 Gauss, 50 Hz.

Qualitative results of optical janus particles in a rotating cluster are shown in Figure 6.2. Although quantitative data cannot be generated from these types of experiments, they do provide a key insight into this problem, similar to the doublet rotation problem: the individual particles are still rotating while the many-body system is curling and forming a cluster. Therefore, it would follow that the hydrodynamic effects from this rotation would be crucial to modeling the experiments.

Experimental data was also collected quantitatively to track the Dynabead assembly. Representative experimental and simulation snapshots (Fig. 6.2) and one-dimensional order parameter trajectories (Fig. 6.3) are shown for select cases that represent the three system sizes and field conditions. The lower frequencies of 0.4 Hz and 0.8 Hz are in the critical frequency range for rotating doublets at 4 and 6 Gauss, respectively, and in this range, the effective pair potentials have a different shape and well-depth than they do in the high frequency (50Hz) field cases.[193] The chain break-up observed in the snapshots of 13 particles at 4 Gauss and 0.4 Hz is due to the intermittent repulsion experienced by particles in the critical frequency regime.[1] The one-dimensional order parameter trajectories of the experiments and simulations show that the simulations are capturing key

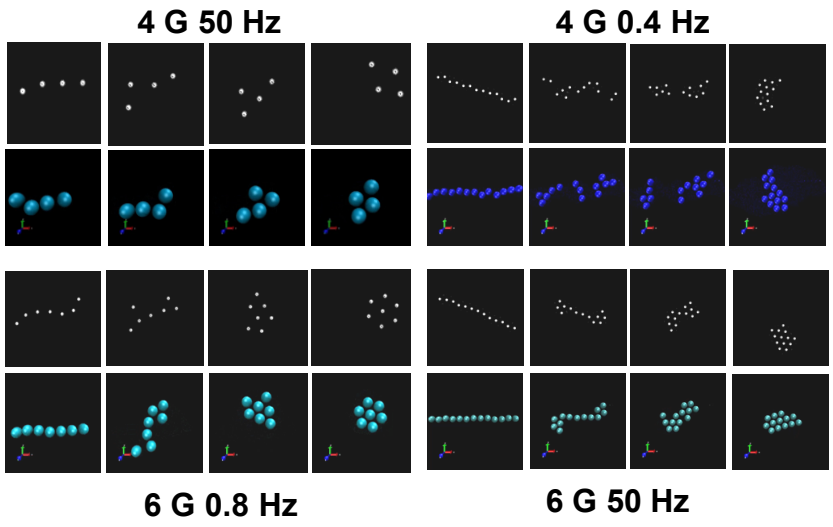

Figure 6.3: Snapshots of example experimental videos and simulation renderings of the four system sizes and four field conditions.

parts of the experimental behavior, within some uncertainty due to the stochastic nature of the process.

In order to compare the simulations and experiments more quantitatively, we report mean first passage times in order parameter space. The key parameters that were tuned in the SD simulations to match the experiments were dynamic susceptibility χ_N and phase lag $\theta_{lag,\mathrm{N}}$. The dynamic susceptibility would affect particle-particle interactions and would therefore impact the rate at which *Rg* decreases and the compactness of the final structures. In addition, susceptibility affects particle-field interactions and thus how fast the particles rotate, which would impact the chain curling, evident in the evolution of order parameter *A*. Phase lag would likely only affect the rotation rate of the particles, and would therefore

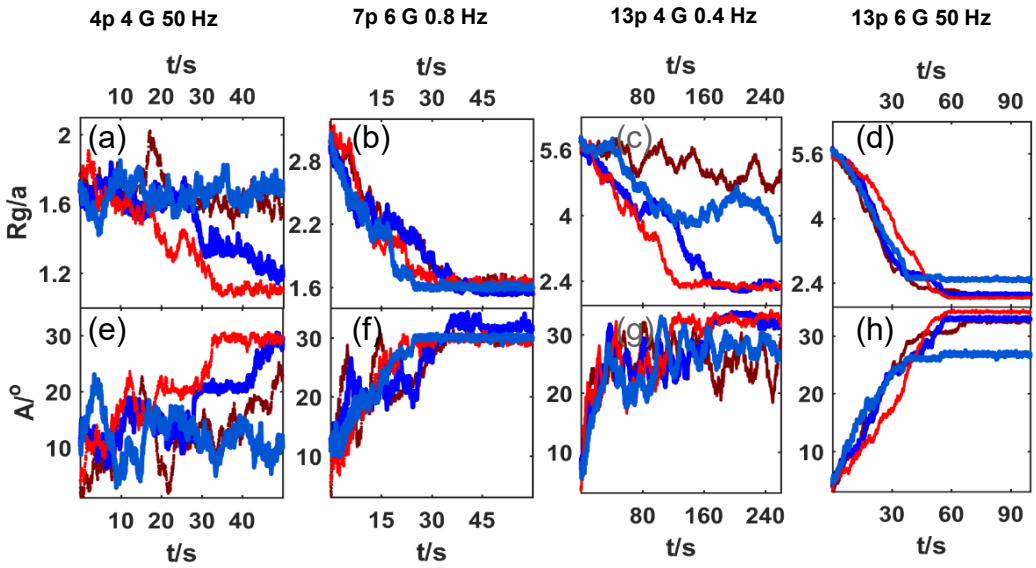

Figure 6.4: Representative one-dimensional trajectories of 2 experiments (red and dark red) and 2 simulations (blue and dark blue) at 4 different conditions/system sizes. Qualitatively, the trajectories show that the experiments and the simulations have the same general behavior, sampling similar configurations at similar time scales. The trajectories show how the order parameters evolve in time, for *Rg* (a-d) and *A* (e-h). At the higher field amplitude of 6 Gauss (b-f) and (d-h), the trajectories are less stochastic, and the system decreases in *Rg* to form a final condensed state. However, for the lower field cases (a-e) and (c-g), stochastic forces are more prominent, and some of the trajectories never reach the final, single cluster condensed state, as shown by the larger *Rg* values at the end of the trajectories. In the case of 13 particles at 4 Gauss, and 0.4 Hz (c-g), the example trajectories where *A* increases but *Rg* **does no**t decrease to the final state of ~2.4, the chain has broken up into 2-3 smaller clusters. Similarly, for the 4 particle trajectories, the lighter blue example shows that the four particles do not form the parallelogram structure at the end of the simulation.

only have an impact on A. Using this intuitive understanding of how the magnetic properties influence the observed experimental trajectories, specific parameters were chosen for the trial SD simulations. The final results for the parameters that had the best agreement are shown in Fig. 6.5, where mean first passage times from 50 simulations and those from 20+ experiments for all four field conditions and three system sizes are plotted. The parameters used in these most optimized simulations are reported in Table 6.2.

Table 6.2: The dynamic Néel susceptibility and the Néel phase lag parameters used in the simulations that best fit the experimental results.

Applied Field	χ_N	$\theta_{lag,\mathrm{N}}$ [rad]
4 Gauss 0.4 Hz	1.25	0.03
4 Guass 50 Hz	1.05	0.035
6 Gauss 0.8 Hz	1.2	0.03
6 Gauss 50 Hz	1.0	0.035

6.4.2. Energy and Diffusivity Landscapes and Passage Time Distributions

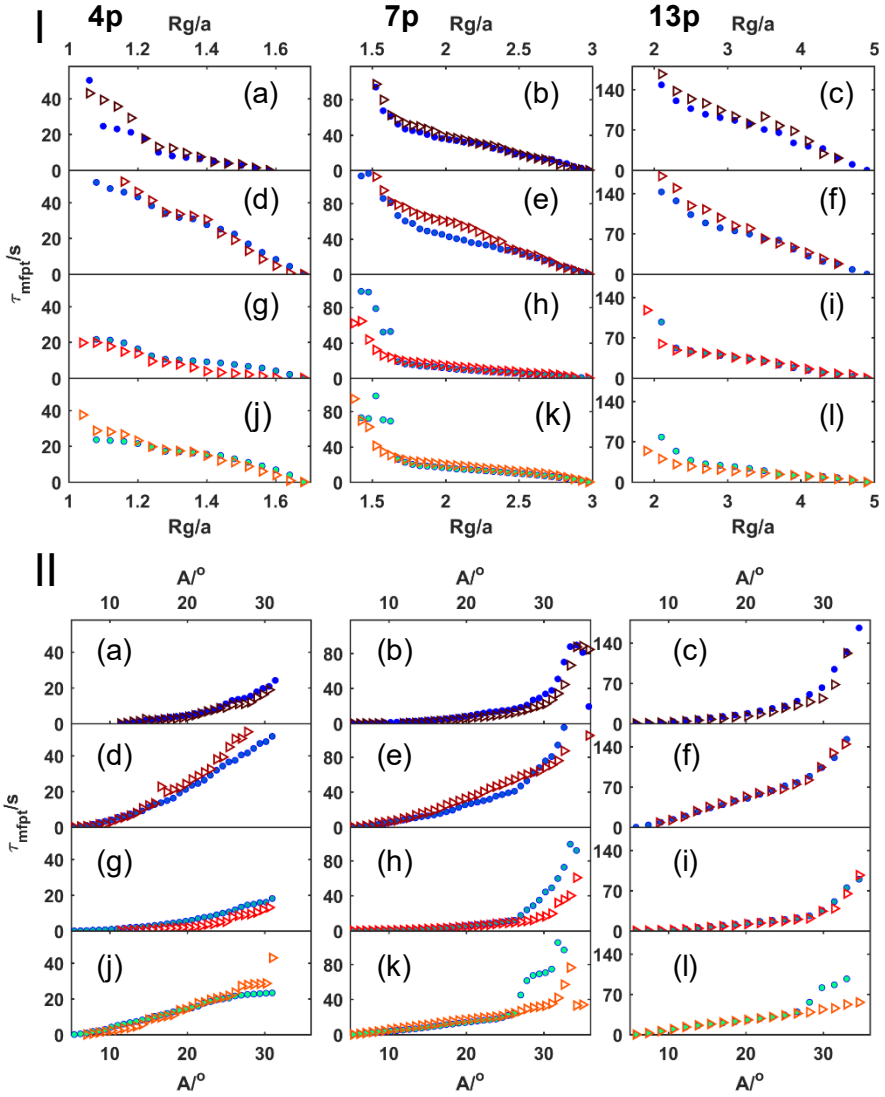

Figure 6.5: Mean first passage times of experiment (red) and simulation (blue) trajectories in Rg (I) and A (II) for 4 particles (first column), 7 particles (middle column), and 13 particles (right column). Field conditions are as follows: (a-c) 4 Gauss 0.4 Hz, (d-f) 4 Gauss, 50 Hz, (g-i) 6 Gauss, 0.8 Hz, (j-l) 6 Gauss, 50 Hz. The simulation results shown in these plots are the optimal trials that had the best agreement with the experiment mean first passage times (the parameters used are displayed in Table 6.2). All trajectories to make these plots begin as chains, or when A=0 and Rg/a is ~1.7 for 4p, ~3 for 7p and ~5 for 13p. As the particles condense and chains start to curl, the experimental and simulations clusters form the same kinds of shapes *and* also the same dynamics (time scales of assembly pathways), meaning that the model accurately depicts the main physics in the experimental systems. The disagreement that is observed for the 7p case (h-k) and to some extent the 13p case (l) is due to poor statistics of the condensed states. In other words, once the cluster forms a final condensed state, it often stays in that state, especially when the amplitude is higher (6 Gauss) and the magnetic interactions between particles is stronger. Thus, the points that trail off at the end of the A and Rg trajectories represent fewer statistics since these values are not as well sampled, compared to the lower values along the pathway towards the condensed states.

The two-dimensional (2D) energy landscape, the elements in the diffusivity matrix, and passage time distributions for the case of 4 particles in a 4 Gauss, 50 Hz field are shown in Fig. 6.6. The landscapes are calculated by solving eqs. (6.18)-(6.20) with spatial resolutions of shown in Table 6.1. An example experimental trajectory is overlaid on top of the energy landscape to illustrate the typical time period and behavior observed for this condition and to show that the simulation-created landscape represents what is observed in the experiments. Interestingly, the energy difference between the starting configuration (a chain – identified as a black dot), and the parallelogram final structure (at Rg~1.2 and A~30º) is only about 5 kT, and the gradient driving the system is very small. This would indicate that the chain configuration is in fact not unfavorable compared to other configurations and is even a metastable state for this case.

First passage time distributions characterize how a stochastic system evolves in time by calculating the time it takes to go from one configuration (defined by *Rg* or *A*) to a final configuration. We compare the high-dimensional (SD) and low-dimensional (2D LDLD and 1D LDLD) simulations (50 simulations each) to the high-dimensional experiments (20+ trials) by plotting the distributions (normalized histograms) of these passage times for

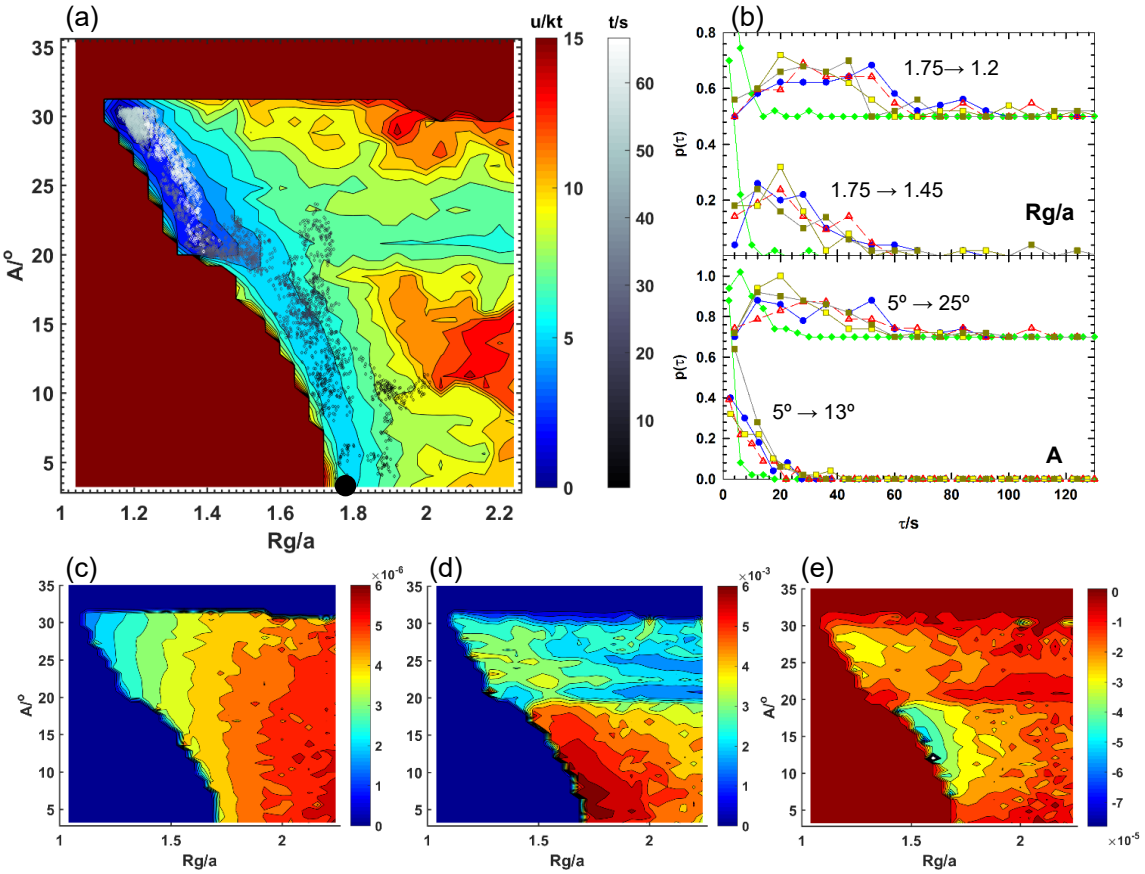

Figure 6.6: Landscapes of 4 particles in a 4 Gauss, 50 Hz field. (a) Two-dimensional effective free energy landscape in order parameter space, with a dot indicating the chain configuration. An experimental trajectory (grayscale in time) is also shown to indicate the condensation process to the final parallelogram state for 4 particles. (b) Passage time distributions for 1D LDLD (green), SD simulations (blue), 2D LDLD with the full diffusivity matrix (yellow) and with diagonal terms=0 (gold) and experiments (red). The starting configuration and ending configurations used to calculate the passage times are shown on the plots for the two order parameters. The high and low dimensional simulations agree with the experiments, while the 1D simulations do not, meaning this system cannot be represented by one dimension (or it could with a more appropriate order parameter). (c) The diffusivity landscape for Rg, D_{RgRg}, (d) for A, D_{AA}, and (e) the cross terms in the diffusivity matrix, D_{RgA}/D_{ARg} all calculated by linear fitting the displacement variances in order parameter space from the SD simulations.

two Rg values and two A values, starting from some initial values. The results indicate that the 1D LDLD simulations, where only Rg or only A is the order parameter, do not sufficiently describe the collective particle behavior as the passage time distributions do not resemble any of the higher-dimensional results. Two different 2D LDLD simulation results are shown: one with the full diffusivity matrix, eq. (6.22), and one where $D_{RgA} = D_{ARg} = 0$ to illustrate how the coupling between these two dynamical parameters plays a role in the dynamics. Both versions of the 2D LDLD agree well with experiments and SD simulations, meaning that the coupling between diffusivities is weak. The plots of the diagonal elements in the diffusivity landscape (Fig 6.6c-d) show that D_{RgRg} decreases as the particles become more condensed (which makes intuitive sense) and that as the particles go from a chain to a two-dimensional, condensed cluster, or as A increases, D_{AA} decreases as the particles are not able to re-orient around each other and change A. For large A but also large Rg (spread out clusters of particles), the diffusivity in A (D_{AA}) is even lower as translational movement of the particles does not affect the angles to the same extent as when the distances between them are smaller. Fig. 6.6e shows how the two order parameters are correlated, showing that they are most coupled during the curling process when the particles are close together and are rotating around each other to form the final parallelogram configuration.

Fig. 6.7 shows the energy landscape, passage time distributions, and diffusivity landscapes for the 7 particle, 6 Gauss 0.8 Hz case, calculated using spatial resolutions shown in Table 6.1. Again, an experimental trajectory overlaid on the landscape shows a typical path for the chain folding and assembly. Contrary to the previous 4 particle example, the pathway from the chain to a condensed structure is favorable, with a steep gradient driving the process to a lower *Rg* and higher *A*. The landscape also shows that a second pathway is also favorable (although less so): the trajectory could go to the top right,

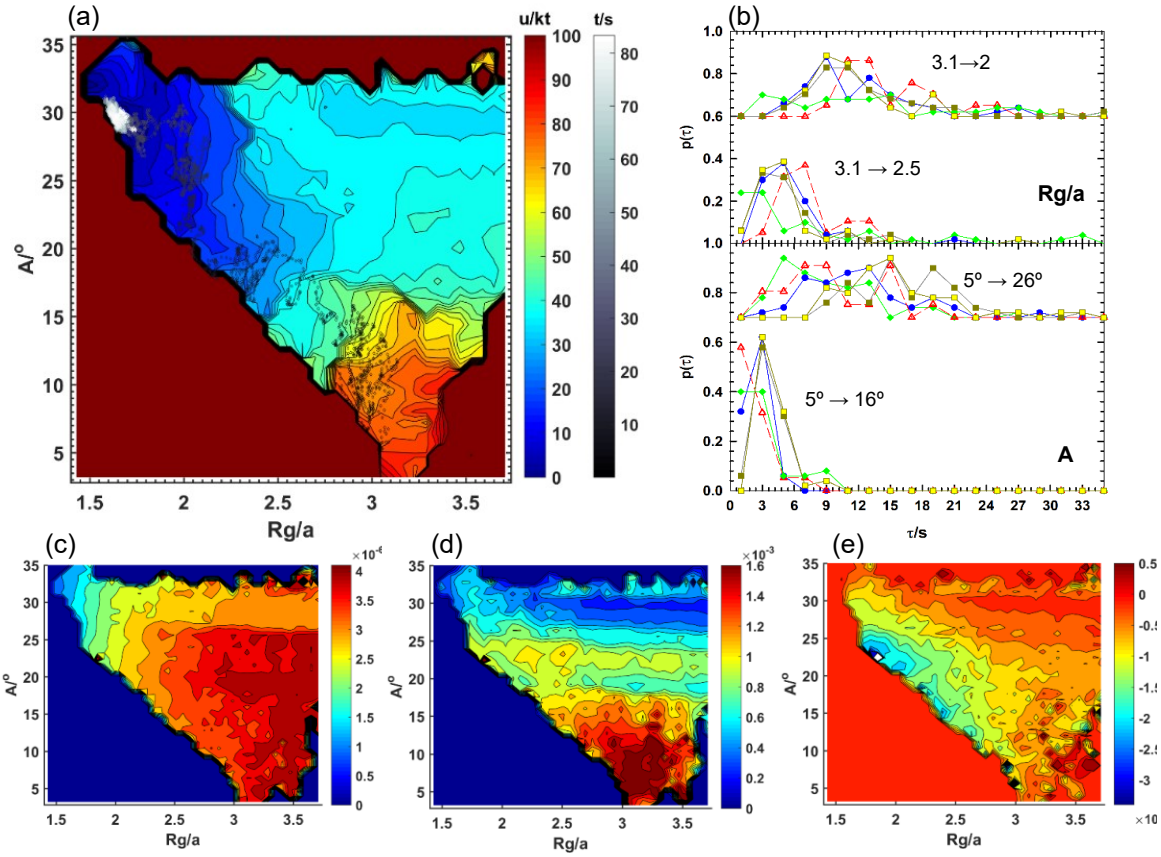

Figure 6.7: Landscapes of 7 particles in a 6 Gauss, 0.8 Hz field. (a) Two-dimensional effective free energy landscape in order parameter space. An experimental trajectory (grayscale in time) is also shown to illustrate a typical condensation process. (b) Passage time distributions follow the same color scheme as Fig. 6.5 (c) The diffusivity landscape for Rg, D_{RgRg}, (d) for A, D_{AA}, and (e) the cross terms in the diffusivity matrix, D_{RgA}/D_{ARg} all calculated by linear fitting the displacement variances in order parameter space from the SD simulations.

or high *Rg* and high *A*, which is indicative of chain break-up where the particles form two or more smaller clusters.

The passage times are faster than they were in Fig. 6.6 for 4 particles, on the order of ~10s, meaning the assembly process is quicker than the 4 particles, 4 Gauss, 50 Hz case. Agreement between 1D LDLD and the higher-dimensional passage times is better than it was for the 4-particle case as well, indicating that the one order parameter representation of this system is less inaccurate. From the plots, the experiments seem to be evolving faster in *A* and slower in *Rg* compared to the SD and 2D LDLD simulations, meaning that the chain curling occurs at a higher rate but the condensation is slower, on average. This discrepancy can be explained by the fact that the passage time distributions are a 1D projection onto an average *A* and *Rg* or an average of the types of pathways. As such, the passage times are sensitive to the number of trials that go to the lowest energy state (high *A* and low *Rg*) directly by following a diagonal path vs. the number of trials that go indirectly by first going up the landscape (increase in *A*) and then finally reaching the lowest state by going left (decrease in *Rg*). Therefore, the slight shift in the passage time distributions of the simulations compared to the experiments signifies that more of the experimental trials went the indirect route, which could merely be a consequence of limited statistics. The good agreement between the full 2D LDLD and the SD simulations means that the 2-order parameter representation accurately reflects the main dynamics of this system. The one plot that shows the least agreement is the passage time distribution for A=5º→26º, showing that even a 2D landscape does not completely capture the full dynamics of the higher-dimensional simulations. Such inconsistencies will be mentioned throughout the rest of the results as a symptom of coarse-graining. The low-dimensional

results will always be less accurate than the real system, but acceptable agreement can be achieved when appropriate order parameters are chosen.

The diffusivity landscapes are similar to the 4-particle example (Fig 6.6) in that D_{RgRg} follows a monotonic trend as the chain condenses, and D_{AA} shows a similar trend as A increases. The diffusivity in A shows a few non-monotonic features, specifically the diffusivity goes to zero at high A but also high Rg, or when the chain has broken up into two distinct clusters. These variations across just one order parameter show that the system

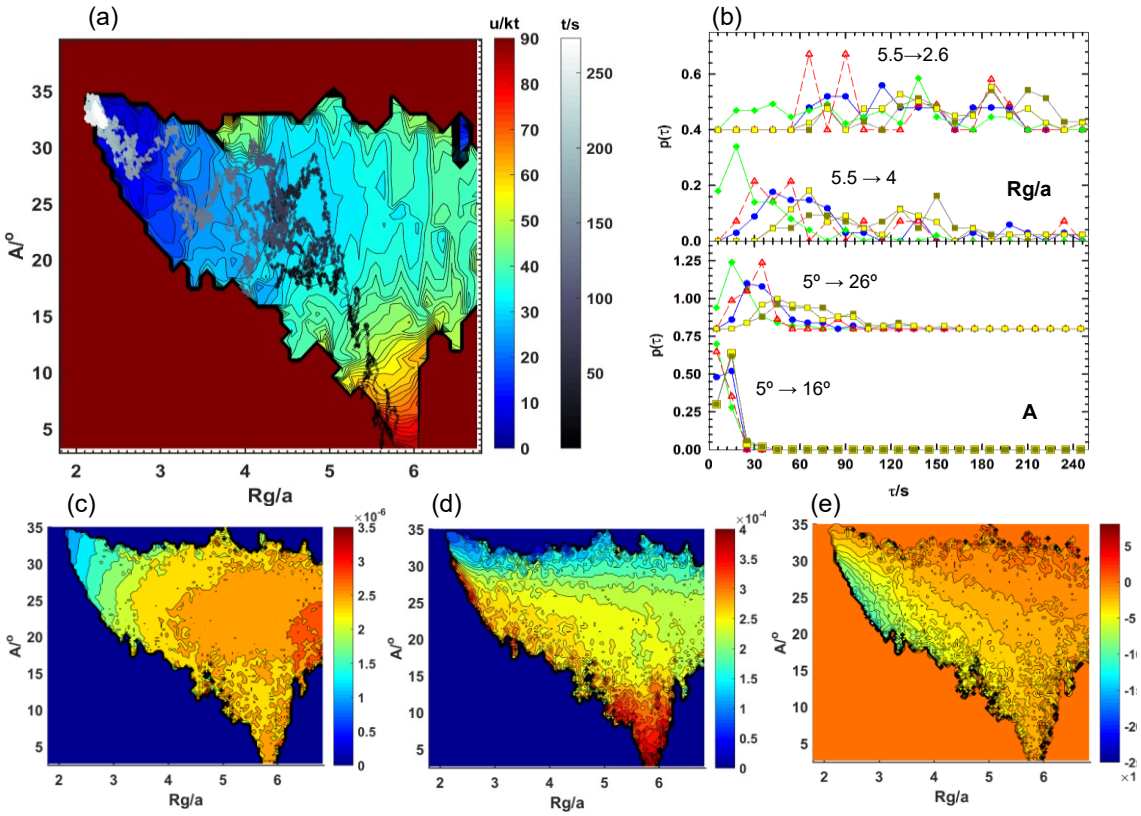

Figure 6.8: Landscapes of 13 particles in a 4 Gauss, 0.4 Hz field. (a) Two-dimensional effective free energy landscape in order parameter space. An experimental trajectory (grayscale in time) is also shown to illustrate a typical pathway, showing that the particles experience some chain break-up (increase in A before decreasing in Rg, in contrast to following the diagonal path), but then eventually form 1 final condensed structure and reach the lowest energy state. (b) Passage time distributions follow the same color scheme as Fig. 6.5 (c) The diffusivity landscape for Rg, D_{RgRg}, (d) for A, D_{AA}, and (e) the cross terms in the diffusivity matrix, D_{RgA}/D_{ARg} all calculated by linear fitting the displacement variances in order parameter space from the SD simulations.

cannot be described by *A* or *Rg* alone: a single order parameter does not accurately describe the full behavior of the system.

The energy and diffusivity landscapes as well as passage time distributions for 13 particles at 4 Gauss 0.4 Hz are shown in Fig 6.8. Since 0.4 Hz is an intermediate frequency in the critical regime, similar to the 0.8 Hz 6 Gauss example for 7 particles, the particles experience intermittent repulsion and as a result some chain break-up occurs. In addition to the frequency effect, since the amplitude of the field is weak at 4 Gauss, the particles have an overall weaker attraction than the other intermediate case at 6 Gauss 0.8 Hz. The pathways reflect this physics as the most favorable trajectory is to go up the landscape, or increasing *A* while keeping *Rg* relatively constant (chain break-up), and then over to the left, or decreasing *Rg*. This pathway is in contrast to the direct, diagonal path of decreasing *Rg* and increasing *A* simultaneously to eventually reach the lowest energy state (s). The experimental trajectory overlaid on top of the landscape is a typical example of a pathway with chain break-up and then eventual formation of one condensed structure. As can be seen by the large blue area in the middle of the energy landscape, once the chain breaks up, the gradient to the condensed state is weak, and some groups of particles remain broken into 2 or more smaller clusters and take a long time to reach the final energy state.

The overall weaker effective interactions between particles contributes to the wide range of pathways that are possible to reach the lower-energy states at 4 Gauss 0.4 Hz. When particle-particle forces are weaker, stochastic forces become increasingly significant, enabling the particles to sample many configurations and causing the broad distributions shown, where passage times are spread out over time periods of 10s of seconds to 100s of second. Statistical effects explain why there is some disagreement between the experiments and SD and 2D LDLD simulations, but despite the experimental limitations in generating large data sets and the intrinsic uncertainty with Brownian motion,

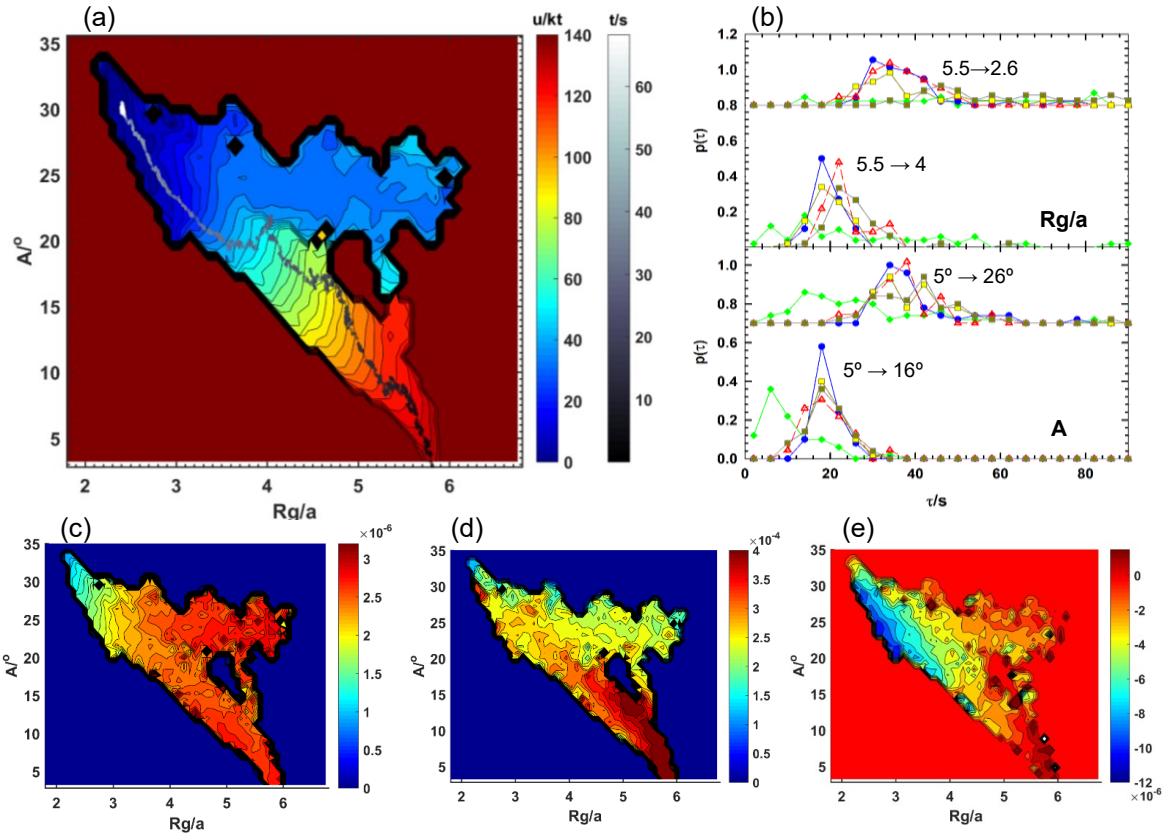

Figure 6.9: Landscapes of 13 particles in a 6 Gauss, 50 Hz field. (a) Two-dimensional effective free energy landscape in order parameter space. An experimental trajectory (grayscale in time) is also shown to illustrate a typical pathway, showing that the particles experience a strong gradient driving them to curl into a final condensed state. (b) Passage time distributions follow the same color scheme as Fig. 6.5 (c) The diffusivity landscape for Rg, D_{RgRg}, (d) for A, D_{AA}, and (e) the cross terms in the diffusivity matrix, D_{RgA}/D_{ARg} all calculated by linear fitting the displacement variances in order parameter space from the SD simulations.

the passage time distributions of the experiments and SD simulations show the same trends. On the other hand, the 2D LDLD passage times seem to be shifted, with the least agreement for A=5º→26º and Rg/a=5.5→4. These results imply that these order parameters are not sufficiently capturing the main dynamics of this particular system, and that a third or alternative order parameter may be necessary. The one-dimensional cases are even worse, however, showing faster dynamics for all of the passage times, illustrating the improvement that can be achieved by adding at least a second order parameter.

Diffusivity landscapes for D_{RgRg} and D_{AA} show similar trends to the 4 and 7 particle cases: D_{RgRg} decrease monotonically with decreasing Rg, while D_{AA} shows some monotonicity with increasing A. Interestingly, as the particles condense but do not reach the lowest energy configuration, or when Rg~2.5 and A~27º, D_{AA} increases, meaning that the particles can diffuse and reorient around each other and are not stuck in a metastable condensed structure. This is the same general region where the diagonal terms, D_{RgA} and D_{ARg}, are at their highest, meaning the friction in A and Rg are most coupled. As the particles reorient in this section of the landscape, changing A, the cluster also samples and eventually condenses into a more favorable, lower-energy state, thus decreasing Rg.

The final case shows the effective energy landscape, passage time distributions, and diffusivity landscapes for 13 particles at a higher amplitude and higher frequency condition, 6 Gauss and 50 Hz. The effective energy has a steep gradient driving the system directly along the diagonal pathway, meaning the particles always fold into a condensed

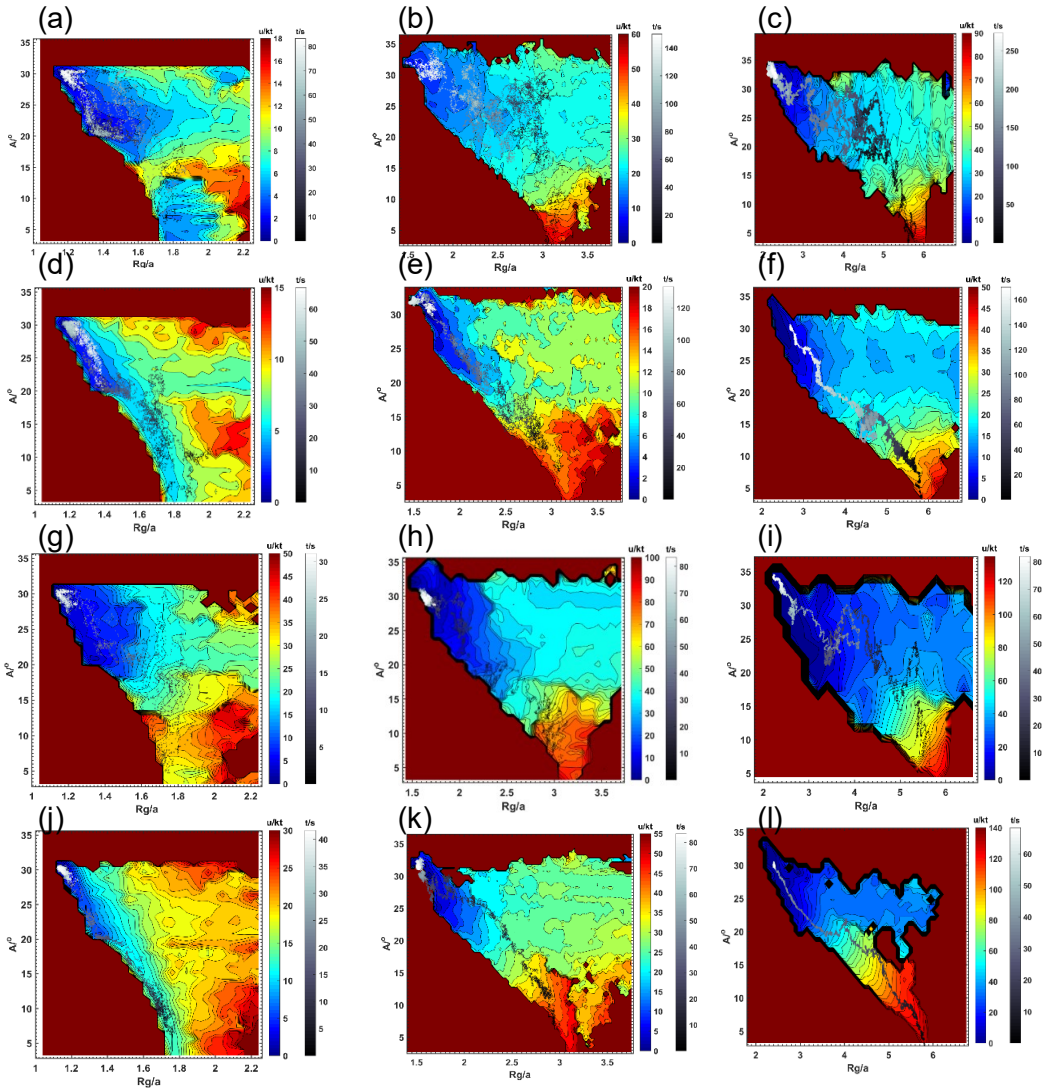

Figure 6.10: Effective energy landscapes for all four system sizes and all four field conditions. The 4 particle cases are the first column, the 7 particle cases are the middle column, and then 13 particles in the right-hand column. Field conditions are (a-c) 4 Gauss, 0.4 Hz, (d-f) 4 Gauss, 50 Hz, (g-i) 6 Gauss, 0.8 Hz, and (j-l) 6 Gauss, 50 Hz. Experimental trajectories are also overlaid on top of each simulation-generated potential energy landscape, showing that the experiments follow pathways that agree with what would be expected given the underlying field gradients. These plots summarize how multiple particle assembly and configurations can be controlled by field amplitude and frequency.

structure with minimal chain break-up due to the strong particle-particle magnetic interactions. As a consequence, stochastic forces are weak and the passage time distributions are narrower for all of the plots. Very good agreement is achieved for the experiments, SD, and the 2D LDLD simulations that include the full diffusivity matrix. The 2D LDLD with diagonal terms in the diffusivity matrix equal to zero does not match as well to the other higher-dimensional results as compared to the LDLD with the full matrix, indicating that the coupling between the parameters is key to capturing the dynamics and microstructures, particularly as the cluster reaches the lower-energy states. This conclusion is also supported by the plot of D_{RgA}/D_{ARg}, showing the same correlation that was observed for the 13 particle, 4 G 0.4 Hz example, where coupling is most prominent at Rg~2.5 and A~27º because as the particles reorient, changing A, they are also able to shift and condense, changing Rg. Regarding the other elements in the diffusivity matrix, the plot of D_{AA} shows a greater diffusivity at low Rg and low A than the previous 13 particle example. One explanation could be that the multi-body hydrodynamic effects of the individual particle rotation, or the flow fields that cause the chain to curl asymmetrically, produce an effectively greater diffusivity along reaction coordinate A, analogous to an effective temperature observed in "active" particle systems where diffusion is enhanced.[201]

6.4.3. Tuning Energy Landscapes with Frequency and Amplitude

In applications where the goal is to create a perfect crystal or a specific structure most efficiently, knowledge of the energy landscapes for several field conditions would enable an engineer to carefully tune assembly. Figure 6.10 shows the energy landscapes for all 3 system sizes and all 4 field conditions, again created by linear fitting SD simulation

trajectories to solve eqs. (6.18)-(6.20). Representative experimental trajectories are also plotted to show typical pathways for each landscape. All 12 landscapes show general trends, including that more chain break-up occurs under the application of an intermediate frequency in the critical regime. As a result, critical frequencies could be applied to melting colloidal solids without completely turning off the particle-particle interactions. In general, if the frequency is in the same regime (critical vs. high) but the field amplitude is different, the landscapes have similar features but different gradients quantitatively. On the other hand, changing frequency but not amplitude results in both qualitative and quantitative differences in the gradients and features of the landscape.

A few qualitative differences are also evident across the different system sizes. In particular, at the intermediate frequencies, a 4 particle chain must surmount an energy barrier to reach the final parallelogram state, while for 7 and 13 particles, the gradient from a chain is always negative, driving the particles to the more condensed states. Even for the high frequency cases at 50 Hz, it is less favorable for 4 particles to form the parallelogram compared to the 7 and 13 particle assemblies, as can be seen by the stripe of blue along the diagonal in Fig. 6.10(d),(j) showing a weak gradient. It is also evident that chain break-up is more common for the 13 particle case compared to 7 particles, indicative of entropic effects on the effective free energy since there are more ways that 13 particles can form multiple smaller clusters than there are for 7 particles.

6.5. Conclusions

The above results demonstrate how low-dimensional modeling can be used to describe the dynamics and microstructures of nonequilibrium colloidal assembly for several system sizes and field conditions. Effective energy and diffusivity landscapes capture the

thermodynamics and the kinetics of nonequilibrium colloidal assembly from a chain to condensed structures, or in some cases, to two or more smaller clusters. Order parameters *Rg* and *A* accurately describe the high-dimensional assembly process for most systems and fields, as can be seen by the agreement in the passage time distributions for SD and 2D LDLD. Experimental passage time distributions also show similar behaviors to the simulations, meaning that both the high dimensional and low dimensional models characterize the main behaviors observed in the real system. Our results elucidate the key physics of superparamagnetic particle clusters in rotating magnetic fields, particularly how both susceptibility and phase lag affect particle interactions, hydrodynamics, and the resulting structures and time scales. The effective landscapes demonstrate how both frequency and amplitude can be used to control particle rearrangements. In addition, the methodology presented in this work is general, and can be applied to other nonequilibrium and "active" colloidal systems to study phase behavior, assembly, and coupling between main dynamical modes.

7. MEASUREMENTS OF KT-SCALE MICROCAPSULE-SURFACE INTERACTIONS AND DEPOSITION LIFETIMES AS A FUNCTION OF FORMULATION CONCENTRATION

The interactions between buckled fragrance microcapsules and a substrate are measured by Total Internal Reflection Micrscopy (TIRM) to determine at which concentration ranges of an amphiphilic surfactant, sodium laureth sulfate (SLES) and a cationic polymer, Salcare SC60, the particles irreversibly deposit. Theoretical potentials for these anisotropic particles have yet to be developed, thus to augment the TIRM data, a trajectory analysis was implemented to quantify the degree of particle deposition as a function of the additive concentrations. The results show that the particles are stable at low

concentrations of SLES, but deposit at intermediate concentrations due to depletion attraction. At higher concentrations, the particles start to stabilize again, which is indicative of depletion repulsion that occurs when volume fractions of the depletant (*i.e.* micelle) is ~10%. In SC60 concentrations, the particles all deposit due to tethering between the polymer and the surfaces, although the interaction potential created by the tether differs depending on the concentration, showing a non-monotonic trend.

7.1. Introduction

Designing core-shell microcapsules that are stable and slowly release their contents at a controlled rate is highly desirable for drug delivery,[202, 203] food products[204] and cosmetics.[205] Strides have been made in the literature to carefully engineer particles with unique chemistries[206, 207] and shape anisotropies and features[208-210] to meet these above goals. However, engineering deposition of the carrier microcapsule onto a preferred substrate is a remaining challenge in many applications to ensure efficient delivery of cargo.[211, 212] Utilizing non-spherical geometries to improve targeted microcapsule-substrate interactions has been of interest with the advent of more advanced particle synthesis methods.[213-215] Shape and orientation of particles influence their internalization by macrophages,[216] an immune response of the human body. Buckled fragrance capsules deposit onto human hair and skin at higher rates than spherical particles.[30]

In addition to the properties of the microcapsule itself, capsule binding to a substrate in solution is influenced by the presence of other components. Crowded cellular environments have been identified as a factor influencing drug delivery efficacy.[217] It was shown that polyethylene glycol (PEG), a common additive used to mimic macromolecules in the cell, induces a depletion attraction between DNA-coated gold nanoparticles, while particles

with different surface functionalities are stable in PEG solutions.[218] For personal care products specifically, fragrance microcapsules exist in complex formulations of surfactants and polymers that cleanse and condition surfaces.[219, 220] While surfactants aid in removing dust molecules from human hair and skin, the objective is to simultaneously ensure the deposition of the fragrance microcapsules to these same surfaces during the washing process. Hence, determining microcapsule interactions with a substrate as a function of common additives will guide the development of efficient fragrance delivery systems in shampoos, conditioners, and shower gels.

Several phenomena influence surface interaction potentials in the presence of surfactants and polymers, depending on surface chemistries and concentrations. For example, amphiphilic surfactants stabilize hydrophobic particles by adsorbing onto their surfaces,[5] or when not adsorbed, cause concentration-dependent depletion attraction or repulsion via the formation of micelles.[221, 222] Likewise, oppositely-charged polymers may coat particle surfaces, leading to steric stabilization,[73] or can be depleted in regions either near the two surfaces or in the bulk, causing osmotic-pressure driven attraction[223] or repulsion,[90] respectively (the same effect as the above colloid-micelle behavior). Polymers can also induce tethering between surfaces,[224] leading to reversible or irreversible deposition. A classic theoretical study showed that all of the above phenomena can occur in colloid-polymer solutions, depending on polymer concentration and the extent of polymer adsorption to the surfaces.[225] The relative sizes of the colloid and the additive also influence the length-scales of stabilization.[226]

The effects of both surfactants and polymers in a formulation could lead to additional phenomena beyond a mere superposition of the separate forces. It was shown that the

sequence of addition to the solution could lead to either steric repulsion or depletion attraction between particles due different adsorption chemistries and morphologies.[227] The interactions between the additives themselves and their relative concentrations also influences their adsorption onto surfaces,[228] which would change the surface chemistries of both particle and substrate. Force measurements showed that two additives formed complexes in the bulk, leading to a unique depletion attraction[229] not explained by a simple summation of interactions. A recent review of combined effects shows that depletion interactions are enhanced in surfactant/polymer mixtures.[230]

Total internal reflection microscopy (TIRM) is the preferred technique to quantitatively measure microcapsule-surface interactions as it is non-intrusive in contrast to AFM, which could potentially rupture microcapsules,[231] and TIRM is more sensitive to weak depletion forces.[78] However, the particles of interest for this report are buckled ("suction cap") core-shell microcapsules[99] that presumably have orientation and position dependent interaction potentials with a surface. TIRM captures equilibrium statistics of particle height above/below a glass slide, hence a one-dimensional (along the z-axis) interaction potential by inversion of the Boltzmann equation would be an average over unknown sampled orientations. Nevertheless, TIRM offers the advantage of being a real-time imaging technique of particle diffusion in x, y and z, such that particle association to the surface can also be determined by analyzing trajectories.[232, 233]

In this work, microcapsule-surface interactions with a negatively charged glass slide (to mimic human hair) of two unique anionic particles are studied as a function of sodium laureth sulfate (SLES) and salcare SC-60 concentrations. The first particles are called PDA, and the second particles are named PGA. Both microcapsules show promise as fragrance

carriers due to their stability, controlled perfume release, and increased deposition onto human hair under shampooing conditions.[99] Particle diffusion and extent of deposition is characterized by a non-dimensional deposition lifetime calculated from trajectory data in the x-y plane. Trajectories and potential energy profiles in z are quantified by the scattering of an evanescent wave, which are qualitatively studied to back out mechanisms. Both PDA and PGA are stable in low concentrations of SLES, then depletion attraction and hence deposition occurs at intermediate concentrations to varying degrees depending on the particle chemistry. At higher concentrations, some PGA and PDA particles experience depletion repulsion and are more stable than the intermediate case. Regarding the effect of SC-60, the polymer causes single chain tethering at low concentrations and the particles irreversibly deposit. At intermediate concentrations, flexible multiple chain tethers enable the particles to diffuse short distances in x, y and z, while at higher concentrations, tighter tethering and depletion causes complete binding. The results elucidate the key interactions governing SLES and SC-60 mediated microcapsule-substrate binding and lay the foundation for future work studying the influence of both additives.

7.2. Theory

7.2.1. Total Internal Reflection Microscopy

In the TIRM experiment (see Fig. 3.3), the scattering intensity of a spherical single colloid in an evanescent wave can be used to determine the instantaneous particle-wall separation, h, (below a wall for a particle less dense than the medium) using the following expression,[234, 235]

$$I(h) = I_0 \exp(-\beta h) \tag{7.1}$$

where I is the scattered intensity, I_0 is the intensity at particle-wall contact, $h=0$, and β is the evanescent wave decay length given by,

$$\beta = \frac{4\pi}{\lambda}\sqrt{\left(n_1 \sin\theta_1\right)^2 - n_2^2} \tag{7.2}$$

where n_1 and n_2 are the refractive indices of the incident and transmitted media, and θ_1 is the incident angle. Using eq. (7.1), measurements of scattering intensity from single particles can be used to monitor their height fluctuations due to Brownian excursions normal to the wall. The probability of sampling each height below the surface (for particles less dense than water, height is the distance *below* the surface) is related to the potential energy of each height by Boltzmann's equation,[235]

$$p(h) = A\exp\left[-\frac{u(h)}{k_B T}\right] \tag{7.3}$$

where $p(h)$ is the probability density of heights sampled by a single particle, $u(h)$ is the particle-wall potential energy profile, and A is a normalization constant related to the total number of height observations. By measuring the number of times a particle samples each height during an experiment, a particle height histogram, $n(h)$, can be measured from time dependent height as,

$$h(t) \;\rightarrow\; n(h) \tag{7.4}$$

With a large enough number of observations, $n(h)$ can be considered a good approximation of the probability density of heights, $p(h)$. The potential energy relative to a reference state can be determined by measuring $n(h)$, substituting for $p(h)$ in eq. (7.3), and then rearranging as,

$$\frac{u(h)-u(h_0)}{k_B T} = \ln\left[\frac{n(h_0)}{n(h)}\right] \tag{7.5}$$

where h_0 often chosen as the most probable height in *n(h)*. This relative separation scale is generally referenced to particle-wall contact at *h=0*.

7.2.2. Colloid-Surface Interaction Potentials

The anisotropic colloidal microcapsules interact with a negatively charged glass slide by a three-dimensional surface force with the wall, u^{pw}, and one-dimensional body forces from external fields, u^{f}, leading to a net interaction potential given as,

$$u(h,\psi) = u^{pw}(h,\psi) + u^{pf}(h) \tag{7.6}$$

where h is the distance between the particle and the surface and ψ is the particle-coordinate polar angle (due to symmetry, there is no dependence on azimuthal angle). The specific interaction potentials include the contributions from Derjaguin Landau Vervey and Overbeek (DLVO) theory,[236, 237] depletion,[23] steric and tethering,[75] and a gravitational field, as shown

$$u(h,\psi) = \left[u_E(h,\psi) + u_V(h,\psi) + u_D(h,\psi) + u_S(h,\psi) + u_T(h,\psi)\right] + u_g(h) \tag{7.7}$$

where u_E is electrostatics, u_V is van der Waals, u_D is depletion, u_S is steric and u_T is tethering. and u_g is gravity.

For spherical microcapsules, there is no polar angle dependence in the potentials in eq. (7.7) and electrostatic interactions are,

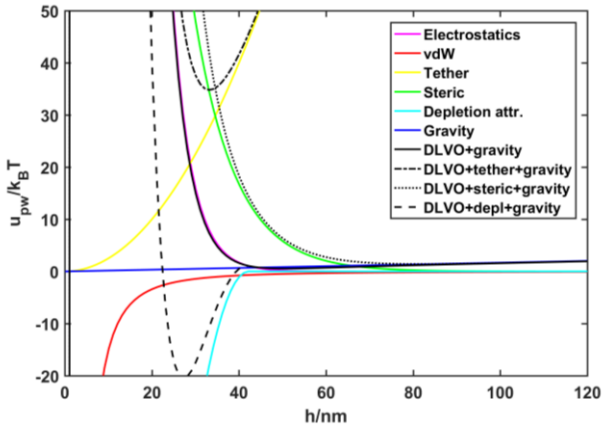

Figure 7.1: Example interaction potentials between a sphere and a wall in a 30mM solution of SLES. The plots show the qualitative features of various spherical particle-surface interactions that can be measured in TIRM. Since the exact theory for anisotropic buckled particles is unknown for most of these potentials, the shapes and ranges of the sphere potentials shown in this figure can be used to analyze anisotropic-particle substrate interaction potentials to deduce mechanisms that contribute to deposition or stabilization. The particle parameters used to calculate the potentials are estimates of the real parameters of the PDA and PGA particles: a=15μm, $\psi_{p/w}$=-30mV and ρ_p=0.966 g/cm^3.

$$u_E(h) = B\exp(-\kappa h) \tag{7.8}$$

$$B = 64\pi\varepsilon a\left(\frac{k_B T}{e}\right)^2 \tanh\left(\frac{e\Psi_p}{4kT}\right)\tanh\left(\frac{e\Psi_w}{4kT}\right) \tag{7.9}$$

$$\kappa = \left(\frac{2CN_A e^2}{\varepsilon k_B T}\right)^{0.5} \tag{7.10}$$

where a is particle radius, ε is the permittivity of water, k_B is Boltzmann's constant, T is absolute temperature, e is the elemental charge, ψ_p and ψ_w are the surface potentials of the particle and the wall, κ^{-1} is the Debye length, C is the bulk electrolyte concentration, and N_A is Avogadro's number. For surfactant solutions, the Debye length is modified to take

into consideration the critical micelle concentration, C_{CMC} as shown

$$\kappa = \left(e^2 N_A / \varepsilon kT\right)^{1/2} \begin{cases} \left[\sum z_i^2 C_i\right]^{1/2}, & C < C_{CMC} \\ \left[\sum z_i^2 C_{CMC} + \left(C - C_{CMC}\right)\omega\right]^{1/2}, & C \geq C_{CMC} \end{cases} \tag{7.11}$$

where z_i and C_i are the valence and concentration of surfactant anions and counterions, and we include a term to account for some fraction, ω, of dissociated counterions (estimated to be 0.25).[23]

Lifshits' rigorous van der Waals theory for flat plates[238] can be approximated by the Hamaker function A(l)[239] and has been simplified to a power-law relationship for particle-flat plate interactions via the Derjaguin approximation[84] and is given as

$$u_V(h) = -aA\left[h + \delta_V\right]^{-p} \tag{7.12}$$

where A and p can be fit to sphere-glass slide measurements and δ_V is a correction factor for surface roughness.[75]

The depletion attraction between a sphere and a flat surface can be described by an osmotic pressure term, $\Delta\Pi$, and an excluded volume, V_{EV}, the latter of which depends on the geometry of the particle and the surface.[23, 240] For dilute concentrations of the depletant (additive), the interaction is nonzero when the distance between the colloid and the surface is less than the size of the depletant as shown

$$u_D(h) = \begin{cases} -\Delta\Pi V_{EV}(h) & h \leq L \\ 0 & h > L \end{cases} \tag{7.13}$$

where L is the diameter of the depletant, and the osmotic pressure is found from

compressibility factors for the depletant, outside (Z_o) and inside (Z_i) the excluded volume region,[23]

$$\Delta\Pi = \rho_o k_B T\left[Z_o - Z_i K\right] \tag{7.14}$$

where ρ_o is the depletant number density outside the region, $K = \rho_i / \rho_o$ and ρ_i is the number density inside the excluded volume. Compressibility factors can be calculated form either the Carnahan-Starling equation of state for effective hard spheres, which applies for micelle depletants, or renormalization group theory in the case of polymer depletants.[241]

At higher concentrations of the depletant, eq. (7.13) may not apply as the depletants no longer behave as an ideal gas and their concentration profile around colloidal particles becomes oscillatory.[242] As a result, above certain volume fractions of the depletant, the potential of mean force between colloids is also oscillatory.[243] In this case, the depletion interaction depends on the depletant distribution profile,[74, 244] one version of which uses adsorption theory,[91]

$$u_D(h) = -k_B T\left[\Gamma(h) - \Gamma(\infty)\right] \tag{7.15}$$

where $\Gamma(h)$ is the adsorbed amount of depletant per area and is a function of the height-dependent depletant number density. In surfactant solutions, the point at which depletion stabilization becomes significant can be qualitatively estimated by calculating the volume fraction of micelles from the following equation,

$$N_{agg} = \left\{[C] - CMC\right\} / [M] \tag{7.16}$$

where N_{agg} is aggregation number, equal to ~42 for SLES,[245] and C and M are the surfactant

and micelle molar concentrations, respectively. Concentration M can be converted to volume fraction by assuming the SLES micelles have an approximate radius of 3nm.[246]

When macromolecules adsorb to a spherical particle and a flat surface with the same thickness, referred to as a brush layer, the system is considered symmetric and the repulsive steric interaction is[75]

$$u_S(h) = 16\pi a f_0 \delta_0 \left(\frac{\Gamma}{\gamma}\right) \exp\left(\frac{-h\gamma}{2\delta_0}\right) \tag{7.17}$$

where f_0 and δ_0 are the free energy and thickness of the uncompressed brush, and Γ and γ are dimensionless constants used to fit unique brush architectures with varying density profiles normal to the surface.

The macromolecules could also bridge a tether between the particle and substrate surfaces, causing an attractive interaction that is modeled as a Hookean spring,

$$u_T(h) = \frac{3Nk_BT}{4PL_T} h^2 \tag{7.18}$$

where N is the number of tethers, assumed to be the same contour length L_T, and P is the persistence length of the macromolecule.

Given the orientation dependence of eq. (7.7), the form of the anisotropic-particle surface interactions will not be the same as it is for spheres. A recent theory solves the DLVO interactions between an anisotropic particle and a surface as a function of Gaussian curvature.[247] Steric interactions would also be valid given the assumptions of this anisotropic theory if the layer thickness is uniform laterally over the microcapsule surface. However, the tethering interaction would be dependent on colloidal geometry if the number

of tethers in eq. (7.18) depends on the orientation of the particle with respect to the surface. Similarly, the development of a theoretical form for orientation-dependent depletion interactions[248] between a particle and a surface is an ongoing area of research.

The gravitational potential for a spherical particle, which can also be approximated for buckled particles using an effective *a*, is

$$u_g(h) = (4/3)\pi a^3(\rho_p - \rho_f)gh \tag{7.19}$$

where ρ_p is particle density, ρ_f is fluid density, and *g* is the gravitational constant.

A summary plot depicting example theoretical spherical particle-surface interactions is shown in Fig 7.1. This plot will serve as a guide for deducing mechanisms of particle deposition. As noted, although the particles in this study are anisotropic and may not obey the theory for spheres, the well-depths, shapes and ranges of the interactions are unique to specific potentials, thus anisotropic particle-surface interactions can be analyzed qualitatively and compared to the theory for spheres.

7.2.3. Deposition Lifetime

The amount of time that a particle is stuck to a surface is quantitatively related to the depth of the particle-surface interaction energy well, $u_{\min}$, as an application of Kramer's escape-rate theory[232, 249, 250] as shown

$$t_D \approx t_{ND} \exp\left(|u_{\min}| / k_B T\right) \tag{7.20}$$

where $t_{ND} = l^2 / \langle D_{\parallel} \rangle$ is the amount of time, on average, it would take for a non-deposited, free particle to diffuse a characteristic length l^2 given an average lateral diffusion

coefficient $\langle D_{\parallel} \rangle$.[250] When particles diffuse in a plane parallel to a nearby substrate, the diffusion coefficient changes as a function of the distance between the particle surface and that substrate, which can be approximated by a scaling factor adjustment of ~0.3 to the Stokes-Einstein diffusion[98, 251] as,

$$\langle D_{\parallel} \rangle \approx 0.3 \frac{k_B T}{6\pi\eta a} \tag{7.21}$$

where η is the viscosity of the fluid. The characteristic length can be set as the pixel length of the experimental videos to ensure we are within the limitations of the video resolution. As such, when the lateral movement of a particle over a time interval of t_{ND} is less than it would be for a non-deposited (stable) particle, the particle is considered to be deposited, as shown

$$\begin{cases} \sqrt{\left(x_i\left(t_{ND}\right)-x_{i,0}\right)^2+\left(y_i\left(t_{ND}\right)-y_{i,0}\right)^2} < \sqrt{2\left(l\right)^2} & deposited \\ \sqrt{\left(x_i\left(t_{ND}\right)-x_{i,0}\right)^2+\left(y_i\left(t_{ND}\right)-y_{i,0}\right)^2} \geq \sqrt{2\left(l\right)^2} & non-deposited \end{cases} \tag{7.22}$$

where $x_i\left(t_{ND}\right), \mathrm{y}_i\left(t_{ND}\right)$ and $x_{i,0}, \mathrm{y}_{i,0}$ are the final and initial particle positions over the characteristic time period t_{ND}. Eq. (7.22) can be applied to calculate the total amount of (consecutive) time particles are stuck to the surface. It should be noted that calculating binding from diffusion normal to the surface from TIRM scattering[232] would not be feasible in our system as the anisotropy makes scattering dependent on height and orientation.

A deposition lifetime is developed by rendering the time a particle is deposited non-dimensional and normalizing by the maximum deposition time (the full length of the

experimental video, t_{VL}), as shown,

$$d_{LT} = \frac{\ln\left(t_D / t_{ND}\right)}{\ln\left(t_{VL} / t_{ND}\right)} \tag{7.23}$$

7.3. Materials and Methods

7.3.1. Materials

The particles are coded as PDA and PGA and were used as received from Firmenich, Inc. (Plainsboro Township, NJ). The density of these particles is roughly ρ_p =0.996 g/ml. In each experiment, particles were diluted in aqueous solutions of deionized water (DI) with additives. Ionic strength was controlled using analytical grade NaCl (Aldrich) without further purification. Texapon N 70 sodium laureth sulfate surfactant (BASF) and salcare SC-60 Acrylamidopropyltrimonium (BASF) were used as received from Firmenich, Inc. Microscope glass slides from Corning (Corning, NY) were used as surfaces in all experiments reported in this work. Glass surfaces were initially sonicated for 30 minutes each in acetone and isopropanol. Then, they were soaked for 1-24 hours in Nochromix (Godax Laboratories, Takoma Park, MD). After washing with deionized water and drying with high purity nitrogen, a 10mm ID x 12 mm OD Viton O-ring (McMaster Carr, Los Angeles, CA) was attached to the glass slide using vacuum grease and epoxy, and sealed with a glass coverslip. When the epoxy was almost dry (2-5 minutes) and the cell sealed, the slides were flipped over to ensure the particles (which cream to the top) are interacting with the glass slide. Prior to use in each experiment, slides were allowed to sit on an air table next to the microscope for equilibration, which took from between 1 hour to 24 hours depending on the viscosities of the various solutions.

7.3.2. Methods

An optical microscope (Axioplan 2, Zeiss, Germany) and CCD camera setup for dynamically tracking and monitoring evanescent wave scattering from levitated particle ensembles was used (see Fig. 2). An o-ring/cover glass batch sedimentation cell is optically coupled to a 68^0 dovetail prism (Reynard Corp., CA) using index matching oil (n=1.515). For inverse TIRM in which the particles cream to the top, the prism is mounted on top of the slide, which is on a three-point leveling stage. In each experiment, a 40X objective (NA=0.65) was used in conjunction with a 12 bit CCD camera (ORCA-ER, Hamamatsu, Japan) operated with 4x binning to produce a capture rate of 28 frames/sec with 336 x 256 resolution (pixel=607nm). Experiments were conducted for 20 minutes for the salt solution cases, 1 hour for SLES solutions to generate enough statistics of deposition lifetimes, and 2 hours for the SC60 solutions (due to the increase in viscosity). The evanescent wave was generated using a 15 mW, 632.8 nm Helium-Neon laser (Melles Griot, Carlsbad, CA) to produce an evanescent wave decay length of 113 nm. A neutral density filter (between 0.5-2.5 depending on the condition) was also used to reduce the intensity of the particle scattering, since scattering should be in the range of the grayscale of the image (0→256) in order for accurate height data to be recorded. In other words, very bright particles that max out the intensity measurement would all appear to be stuck or deposited on the slide.

Because particles freely diffuse below the glass surface, image analysis algorithms coded in FORTRAN were used to track the lateral motion and integrate the evanescent wave scattering intensity for each particle. Standard video microscopy algorithms were used to locate and track centers of the evanescent wave scattering signal on each particle.[252, 253] The total scattering intensity from each particle was obtained by integrating all pixels within a specified radius of the scattering signal center pixel. A separate image analysis algorithm was developed in MATLAB to size the particles from standard transmitted light microscopy images. A bandpass filter algorithm[102] is first used to increase contrast levels, then the function *bwboundaries* is applied to identify the particle outlines. Particle center is found by the average of all outline coordinates, then the radius is calculated from the average distance between the center and outline coordinates. The particles identified and

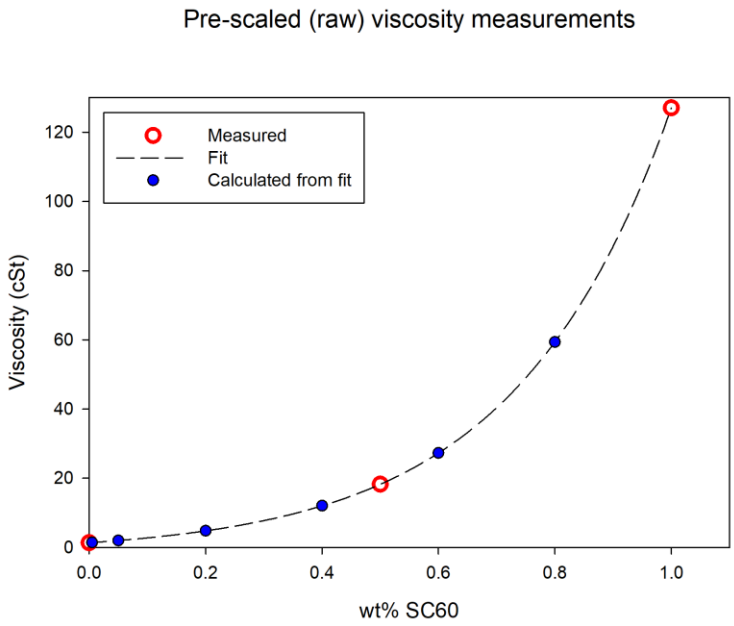

Figure 7.2: Viscometer measurements and fit of viscosity as a function of wt% SC60 polymer. The viscosity of DI water, 0.5wt% SC60, and 1wt% SC60 were measured using a viscometer. The data were fit to an exponential function of the form f = y0+a*exp(b*x), where y0=-1.732, a=3.10, b=3.726. The viscosities of other intermediate concentration solutions were then determined from this fit. To adjust for instrument measurement error, the viscosities shown in this plot were then rescaled/calibrated to the known viscosity of water, 0.9 cSt (the raw measurement for DI water was 1.37 cSt), for calculation of $\langle D_{\parallel}^{\backslash} \rangle$.

tracked in the TIRM scattering videos are then matched to the particles identified in the light microscopy images.

Deposition lifetimes, d_{LT}, are calculated using eqs. (7.21)-(7.23) by setting the characteristic length *l=607nm*, which is the pixel size of the videos with a binning of 4 in the recording software Streampix. The lateral diffusion coefficient in eq. (7.21) is approximated by using the average microcapsule size of 2a=15μm. The viscosity as a function of SC60 concentration was measured using a viscometer, the results of which are shown in Fig. 7.2, and these values are directly used to calculated $\langle D_{\|}^{\setminus} \rangle$ by re-scaling based on the viscosity of water, 0.9 cSt, by the appropriate factor. For SLES, the viscosity of a 12wt% SLES solution was measured to be twice that of water, and all other intermediate concentrations were linearly interpolated to calculate $\langle D_{\|}^{\setminus} \rangle$. It should be noted, however, that although $\langle D_{\|}^{\setminus} \rangle$ is sensitive to particle size and viscosity, the deposition lifetimes calculated from the experimental trajectories are only sensitive to the order of magnitude of $\langle D_{\|}^{\setminus} \rangle$, hence they are sensitive to the order of magnitude of the particle size and viscosity only (see the Results and Discussion for further exploration of particle size effects in the dynamical analysis).

7.4. Results and Discussion

7.4.1. Base Case A: Potential Energy Profiles of Spherical Capsules with Salt

TIRM of particles less dense than water had not previously been conducted in the Bevan laboratory. In addition, it was unclear whether the core-shell microcapsule scattering

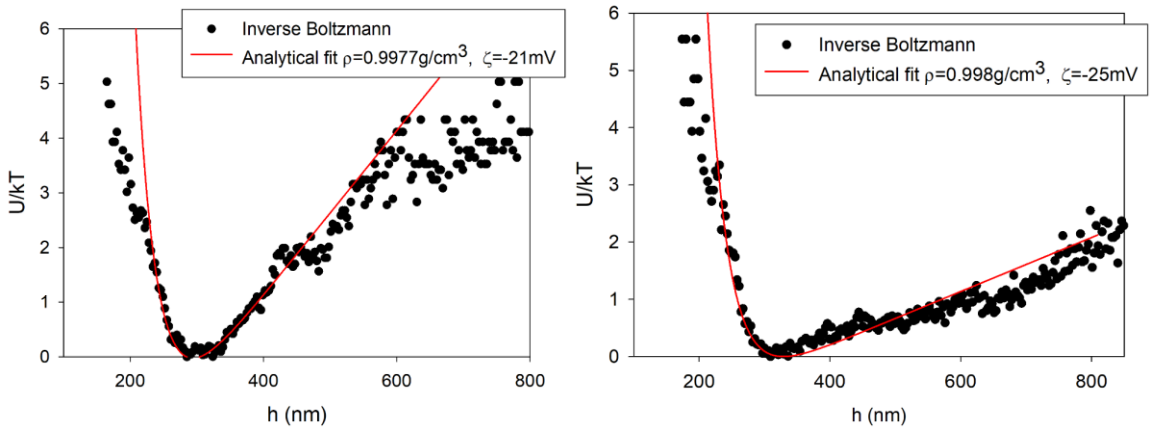

Figure 7.3: Potential Energy Plots of Spherical Microcapsules Interacting with a Charged Glass Slide. Theoretical potentials that include electrostatic repulsion and the gravitational body force are fit to experimental measurements of two different spherical particles in a 0.1mM NaCl solution interacting with a wall. The only fitting parameters are zeta potential and particle density as the size was estimated by analyzing light microscopy images in ImageJ, where the particle sizes are (a) 2a=16.7 μm and (b) 2a=12.3μm.

of the evanescent wave would follow the same theory used for silica and polystyrene, *i.e.* would be proportional to height, given that it is a composite material. Therefore, it was necessary to test the new inverted TIRM set-up on anionic polyurethane spherical microcapsules,[30] which are similar to the PDA and PGA particles, to ensure that the potential energies agreed with exact theory before exploring anisotropic surface interactions, for which exact theories have yet to be developed.

Fig. 7.3 shows example potential energy plots for two different spherical particles. The particle sizes were estimated by manually analyzing light microscopy images in ImageJ such that the only fitting parameters were particle density and zeta potential, which are displayed on the plots. Both fits produced similar theoretical parameters, indicating that the particles have similar properties even if there is some size polydispersity. The plots also

illustrate that the TIRM measurements are reliable since the fitting parameters are reasonable given previous knowledge and characterization of these particles. The potential energy results are also consistent over several particles and trials.

7.4.2. Base Case B: Potential Energy Profiles of Buckled Capsules with Salt

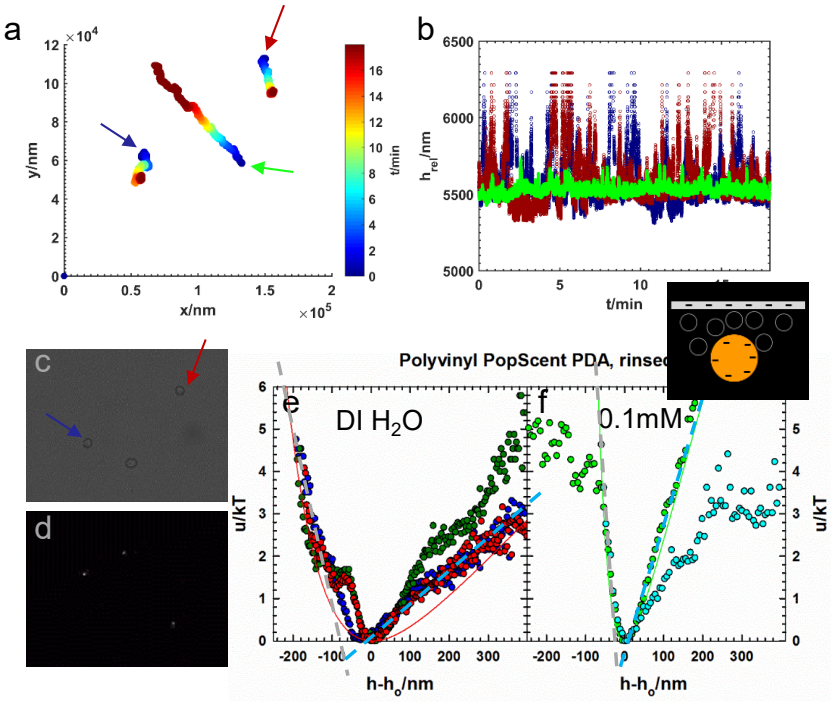

Fig. 7.4. PDA particles are stable in low salt solutions due to electrostatic repulsion. (a) Trajectories of representative PDA particles during TIRM experiments in DI water (red, blue) and in a 0.1 mM NaCl aqueous solution (green). (b) Trajectories in z for the same particles, plotted as relative height, or distance, below the above glass surface, over a period of approximately 20 minutes. (c) A still image of the DI water experiment, showing two of the representative particles, and the (d) corresponding scattering image of the same particles when the backlight is turned off. The intensity of the particles is only due to scattering of the evanescent wave. The symbols in (e) and (f) are the potentials for various individual particles. It is shown that the particles in the low salt solution display very broad electrostatics, although a theoretical potential for spheres that is the sum of electrostatics and gravity does not capture the whole experimental curves, most likely due to shape-effects. (f) A potential profile is fit to one of the experiments at 0.1 mM, for a diameter of 2a=19um, showing that at these conditions, the experiments do obey the theory for spheres. The grey and blue dotted lines in (e-f) are shown as visual guides, and approximately represent how to interpret the repulsive and attractive sections of the potential energy plots. The slope of the grey line should increase with increasing salt, as is observed, while the attraction should increase for larger particles, also what is observed.

In this next section, we continue to build up in complexity by reporting results for the buckled microcapsules in salt solutions. Before conducting experiments of the buckled microcapsules in the solutions of interest, it is imperative to first create a foundation from which to build by measuring particle-surface interactions in the presence of salt only, where only electrostatics and van der Waals interactions apply. Since the interaction potentials are relatively simple and the parameters in the theoretical equations for spheres are known and have already been fit to experimental data, these base case experiments in salt also provide a basis for understanding how anisotropic effects impact the measured interactions as well as particle scattering.

Fig. 7.4 shows results for PDA particles interacting with an above glass slide in aqueous media of DI water and 0.1 mM NaCl. Representative trajectories are plotted in the *x*-*y* plane (parallel to the slide) color-coded in time, and in *z* (normal to the slide) throughout the duration of the experiments, approximately 20 minutes. The trajectories correspond to the potential energy profiles, plotted on the scale of thermal energy, kT and normalized so that the most probable height h_0 is at $u(h_0)/kT=0$. These profiles are calculated using the electrostatic and gravitational interactions and are equilibrium measurements, meaning they represent the average interaction between each particle and the portion of the glass surface sampled by the particle due to lateral diffusion. An image of the particles in a PDA DI water experiment with the backlight on is shown in Fig. 7.4c, along with the corresponding evanescent wave scattering image for the same particles in Fig. 73.d.

The particles in Fig. 7.4 are stable as is shown by the lateral diffusion in x and y. The particles in DI water fluctuate in z much more than the particle at 0.1 mM (bright green), as is most evident in Fig4b. This particle at 0.1 mM is larger (confirmed via image analysis)

and experiences a strong gravitational force towards the surface, and also has a steeper electrostatic repulsion since higher salt concentration shortens the Debye length (eq. (7.10)), which is further illustrated in the narrower potential plot in Fig. 4f for that particle. The experimental potentials, shown as symbols in Fig. 7.4e and Fig. 7.4f, represent the superposition of energies, with the repulsion generally corresponding to the left-hand side and the attraction on the right-hand side. The solid lines are theoretical fits using electrostatics and gravity where the surface potentials for the particles and the slide are assumed to be -60mV and the gravity is fit by finding the approximate size of the particle with a particle density of ρ_p =0.996 g/ml.

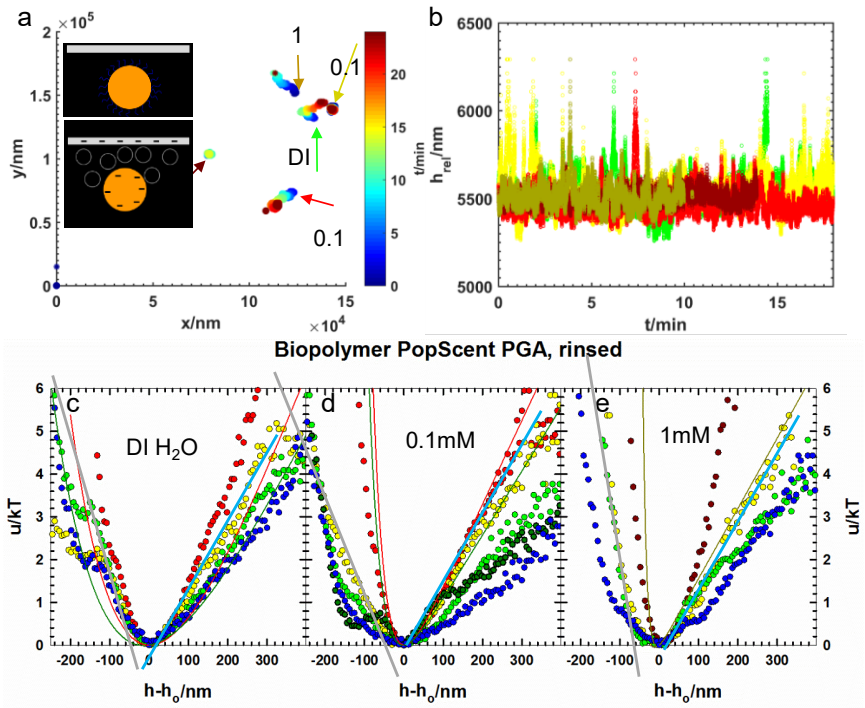

Fig. 7.5. PGA particles are stable in low salt solutions due to electrostatic repulsion and possibly also due to steric repulsion from the polymer layer on the surface of the particle. (a) Representative trajectories in the x-y plane for a particle in DI water (green), particles in a 0.1 mM NaCl solution (red and yellow) and particles in a 1 mM NaCl solution (dark red and dark yellow). Some particles appear to be stable at all three concentrations, while one particle each at 0.1 mM (yellow) and 1 mM (dark red) are not diffusing laterally. Nevertheless, all of the particles are diffusing in z (b), although the dark red particle does appear to be deposited, and apparent fluctuations in z may be due to orientational diffusion instead. (c) Potential profiles of several unique particles from TIRM experiments in DI water, showing broad distributions, which is to be expected at low salt, although the solid theoretical lines (electrostatics + gravity) cannot capture the behavior, due to shape-effects. (d) The particles also show broad potentials at 0.1 mM, and only one of the curves is close to the theoretical prediction from electrostatics (red line), which should get steeper with increasing salt, indicating the current theory is inadequate. (e) Potentials at 1 mM, at which the electrostatic repulsion should be very steep. Theory for spheres matches gravity (solid dark yellow line), but does not predict the repulsion. The narrow dark red curve in (c) that corresponds to the dark red trajectories in (a-b) is indicative of a deposited particle. The grey and blue lines in (c-e) are shown as visual guides, and approximately represent how to interpret the repulsive and attractive sections of the potential energy plots. The slope of the grey line should increase with increasing salt, which is *not* observed on average, while the attraction should increase for larger particles, which *is* observed.

Theory does not fit as well to the DI water experiments, most likely due to shape-effects as the particles are farther from the slide and can diffuse rotationally, sampling different

orientations. As a result, the relation between intensity and position (eq. (7.1)) is more complex since orientation as well as height will affect intensity. On the other hand, the particles closer to the slide in 0.1 mM solutions have limited rotational mobility, and therefore most likely remain in one orientation. Thus, eq. (7.1) is valid and one can fit theoretical potentials derived for spheres, as shown by agreement between the solid green line and the green points in Fig. 7.4f. It should be noted that at 1 mM NaCl, the PDA particles all deposit and are deposited to the glass slide (not shown).

Fig. 7.5 shows trajectories and potentials for PGA particles in DI water, 0.1 mM and 1 mM NaCl. PGA particles are mostly stable at 1 mM, in contrast to PDA particles. One of the particles (color-coded as dark red) in 1 mM appears to be deposited laterally, but still diffuses in z. As a result of this trajectory, this particle has the narrowest potential energy profile, shown in Fig. 7.5e. Similar to the DI water plots in Fig 7.4e, theoretical curves that include electrostatics and gravity (derived for spheres) do not fit to the experimental potentials shown in Fig. 7.5c because of the anisotropic nature of the particles. Interestingly, potentials at 0.1 mM and 1 mM also show broad distributions, indicating that the theory for electrostatic repulsion does not apply for PGA particles, since the repulsion should be steeper at higher salt concentrations, a part of the theory that was appropriate for the PDA particles in Fig. 7.4. Only one of the experiments at 0.1 mM (bright red in Fig. 7.5d) seems to be close to the spherical theoretical potential for both gravity and electrostatics (eq.(7.8)). The solid line in Fig. 7.5e shows that the particle can be fit for gravity, but not electrostatics, indicating an additional interaction such as steric repulsion.

7.4.3. Case I: Trajectories and Energies of Non-Depositing Buckled Particles

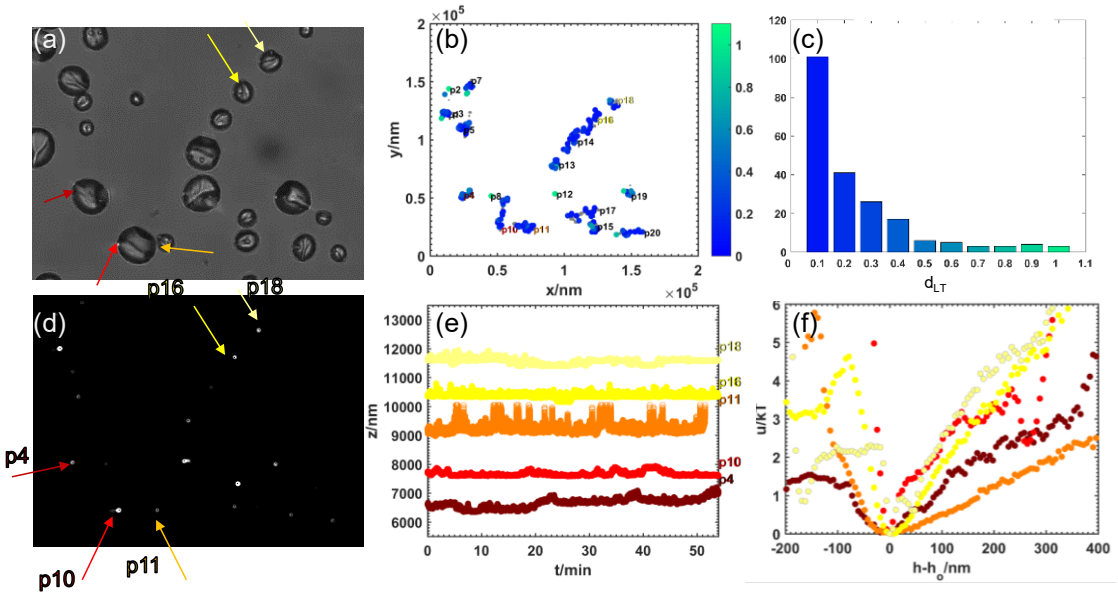

Fig. 7.6: Example case of an experiment where most of the particles do not deposit, PDA particles in 0.12wt% SLES. (a) A light microscopy image, (b) trajectories in the x-y plane color-coded by the dimensionless deposition lifetime parameter (eq. (7.23)) where 0 is stable and 1 is desposited throughout the whole video. (c) Histogram of the deposition lifetimes recorded for this particular experiment, which is biased toward the left side – meaning most particles are stable. (d) Example snapshot of the TIRM video of the particle scattering, where specific particles are labeled. (e) The trajectories in z of the labeled particles, and (f) the corresponding potential energy from the statistics from the z trajectories for the specific particles, showing broad sampling indicative of electrostatic stabilization observed for the spherical microcapsule interactions in salt.

Fig. 7.6 displays an optical microscopy image of PDA microcapsules, a snapshot of the corresponding scattering video, trajectories in *x, y* and *z,* deposition lifetimes, and potential energy profiles for an example case where most of the particles are stable in solution and do not deposit onto the surface of the glass slide. In this particular experiment, the particles are in an aqueous solution that is 0.12wt% SLES, which is just above the critical micelle concentration (CMC) of 0.8mM (~0.03wt%) for SLES.[245] The planar trajectories are shown in grey while the color-coding on top of the trajectories are deposition lifetimes, calculated from eq. (7.22)-(7.23). As can be seen, most particles are freely diffusing, sampling positions in *x* and *y* on the order of the diffusion coefficient for stable particles, eq. (7.21). The deposition lifetimes (eq. (7.23)) can be plotted as a histogram as a method

to characterize the degree of binding and stability for all of the particles in a particular experiment. Fig. 6c shows a histogram skewed to the left, meaning most particles have a deposition lifetime close to zero.

Example trajectories of relative height, or relative particle sampling in *z*, are calculated from eq. (7.1) and are shown for five representative particles in Fig 7.6e, demonstrating that most of the particles are moving freely normal to the wall and are not deposited. The smallest particle (particle 11) exhibits the most fluctuations in *z* while the larger particles sample fewer heights due to stronger gravitational forces. Movement in *z* (note – all *z* trajectories are *relative* and are shifted for easy viewing) appears to be related to the *x*-*y* diffusion, as shown by particle 18 that deposits on the surface for a short time, and also has fewer fluctuations in z due to this temporary, reversible deposition.

The potential energy profiles can be calculated from the height trajectories via eq. (7.3) , although this application of the theory for spherical particles to buckled particles may include some inaccuracies due to possible orientation-dependence of the scattering. Nonetheless, the potential profiles displayed in Fig. 7.6 can be qualitatively analyzed and in general show that the particles experience a gravitational force pulling them towards the glass surface as well as an electrostatic repulsion as they approach the slide. Particle size is evident by the depth of the potential, as can be seen by a steep or shallow gradient driving

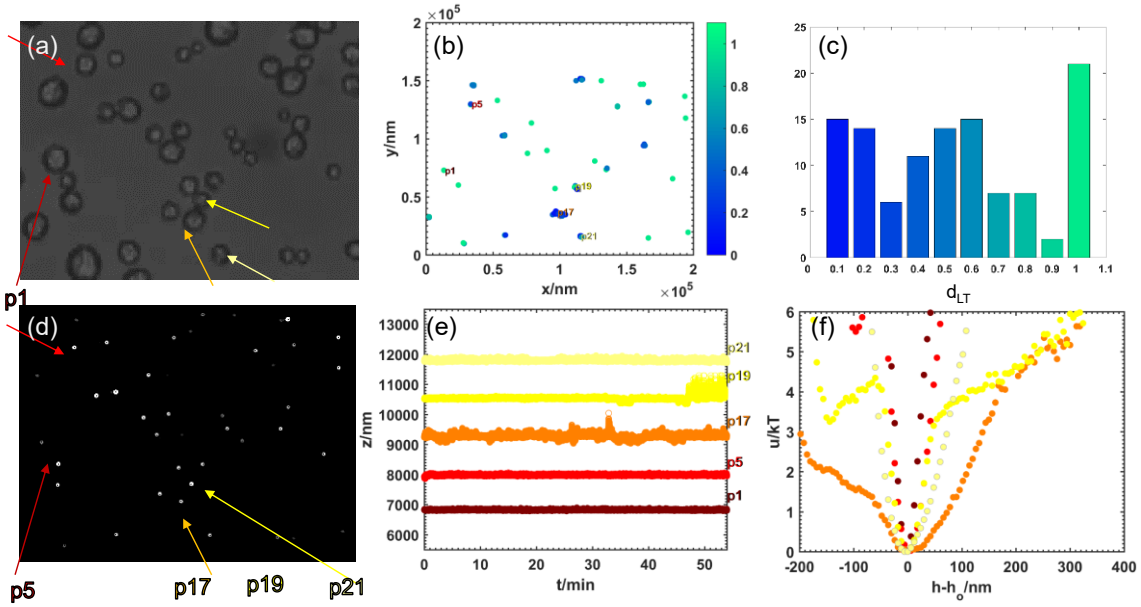

Figure 7.7: Example experiment where both irreversible and irreversible deposition occurs, PGA particles in 1.2wt% SLES. (a) Light microscopy image of the particles, (b) Planar trajectories color-coded by the deposition lifetime parameter (eq. (7.23)) showing that most of the particles are deposited throughout the length of the video by the turquois dots indicating the dimensionless deposition lifetime is 1. (c) A histogram of the measured deposition lifetimes, showing a wide range in behaviors as this concentration is a transition point for PGA stability in SLES. (d) A snapshot of the TIRM scattering video with specific particles labeled, and then the (e) corresponding trajectories normal to the surface for those particular particles and (f) their potential energy profiles, showing that some of the particles are completely stuck and therefore have narrow profiles, while others show slightly broader profiles indicating that they were stuck for part of the video (p19) but came off for certain time periods, hence experience reversible deposition. The potential energy for p17 is broader than most, meaning it is the most stable, but still experiences some association to the surface, as the profile is still narrower compared to the previous case, Fig. 7.6.

the particles towards the surface. For example, particles 11 and 16 both have linear attractive sections of the curves (right-hand side), due to the linear gravitational force with height, eq. (7.19), and it is evident that particle 11 is smaller than particle 16 by the smaller slope. The unusual features in the potential energy plots, such as electrostatic repulsion that appears to decrease as the distance between the capsules and surface decreases, are a result of the anisotropy of the buckled particles. Since the potential energies have both an orientation and a height dependence, the height potential energy profiles can be thought of as a projection down to a 1D characterization of the system, dependent upon which orientations were sampled throughout the length of the video. Overall, the energies in Fig 7.6 are all broad and indicate that the particles are stable and sample many heights.

7.4.4. Case II: Trajectories and Energies of Reversible and Irreversible Deposition of Buckled Particles

Fig 7.7 shows experimental images, trajectories, and potential energies for an intermediate case (PGA in a 1.2wt% SLES solution) where some of the particles are deposited throughout the whole length of the video and some experience reversible deposition. The *x* and *y* trajectories and deposition lifetimes and histogram illustrate that most of the particles are deposited, while some bind to the surface of the slide for a period of time, but then come off. The histogram is relatively flat, showing the distribution in deposition behaviors for this particular experiment. Height excursions reflect this variation in behavior, as several of the *z* trajectories are completely flat, or the particles are stuck on the surface of the slide, while others show some sampling in *z*. Particle 19 is deposited for most of the video, but breaks off from the slide surface and samples different heights for specific intervals, and remains stable in solution towards the end of the trajectory. This

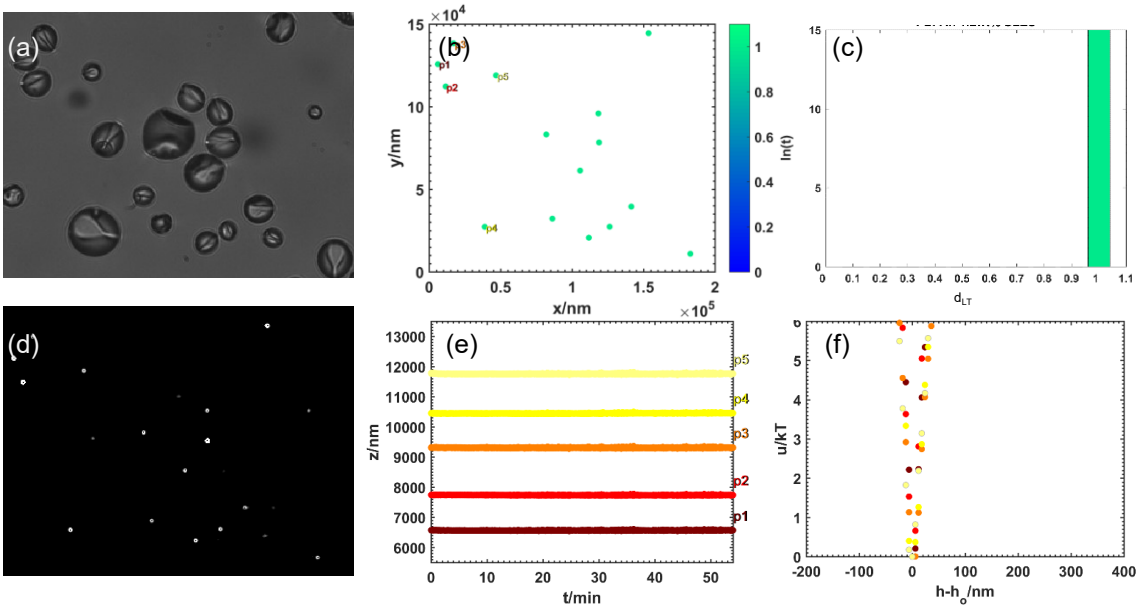

Figure 7.8: Trivial result where all of the particles are completely deposited on the slide, for PDA particles in 1.2wt% SLES. (a) Light microscopy image of the particles, (b) stuck trjaectories, (c) histogram with a single bar =1, or complete deposition, (d) snapshot of the scattering video where the intensity is the the same for all particles throughout the whole video, indicating that (e) the trajectory in z is flat with time and (f) the potential energy profiles are extremely narrow and would be a delta function if there were no noise in the intensity measurements.

behavior is also evident in the *x-y* trajectory of particle 19 by the different colors overlaid on its trajectory (blue and turquois), signifying the different deposition lifetimes experienced by this unique particle. The potential energy for particle 19 is an average representation of the *z* coordinates: there is a deep energy well driving the particle towards the surface as well as a linear region with increasing *h,* indicative of the gravitational potential experienced by the particle when it's stable. Particle 17 is the most stable, and diffuses in *x, y* and *z* throughout the whole video.

7.4.5. Case III: Trajectories and Energies of Irreversible Deposition of Buckled Particles

Particles that are irreversibly deposited remain immobilized on the surface of the glass slide, displaying no movement in the *x*-*y* plane, and subsequently the height trajectory is flat as a function of time. An example of the trajectories and energies for this case is shown in Fig 7.8, for an experiment of PDA particles in a 1.2wt% solution of SLES. The histogram of deposition lifetimes displays a single bar at 1, meaning all particles are deposited. The

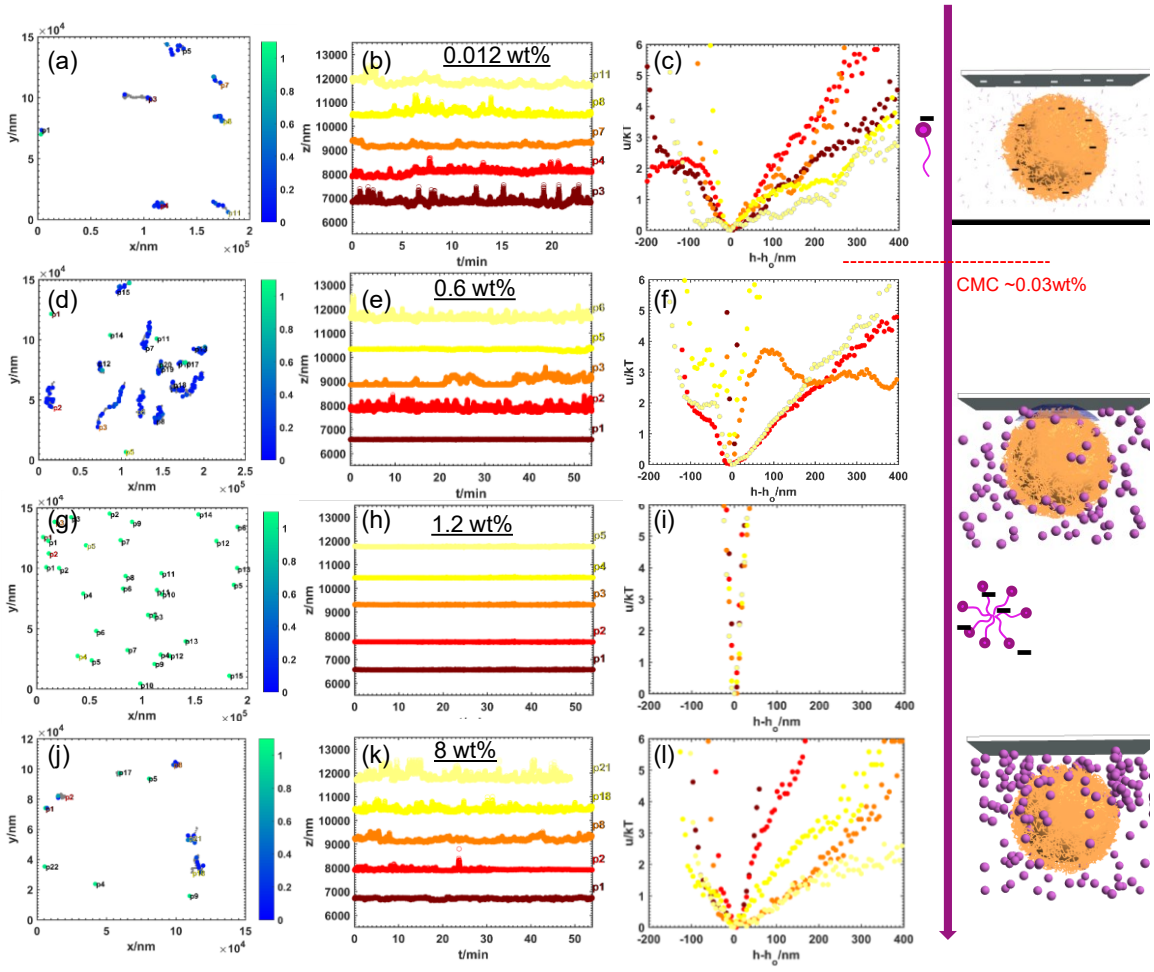

Figure 7.9: Trajectories and potential energies of several trials of PDA particles at four different SLES concentrations representing the four main regimes. Particle trajectories in the x-y plane are color-coded by the deposition lifetime parameter, and representative trajectories in height are shown along with the corresponding potential energy profiles for (a-c) 0.012wt% SLES, (d-f) 0.6wt% SLES, (g-i) 1.2wt% SLES and (j-l) 8wt% SLES. At the lowest concentration below the CMC, the particles are stable due to electrostatic repulsion. Above the CMC, the particles begin to deposit due to the formation of micelles that causes a depletion attraction, and then at the even higher concentrations, the depletants start to pack around the microcapsule, causing oscillatory concentration profiles of the micelle and a barrier that causes kinetic depletion-induced stabilization.

potential energy profiles are narrow and would be theoretically equal to the delta function (*i.e*. only one height is sampled) in an experiment with zero noise (even completely stuck particles display apparent fluctuations in height due to experimental limitations such as fluctuations in the laser intensity[254]).

7.4.6. Buckled Particle Deposition and Mechanisms as a Function of SLES

TIRM experiments were conducted at specific SLES concentrations ranging from 0.0012wt% to 12wt% for both the PDA and PGA microcapsules and the trajectory and energy analyses introduced in the earlier sections were applied to quantify deposition and decipher mechanisms. The 12wt% case is the maximum concentration for shampoo formulations, and is below the concentration where SLES amphiphiles start forming non-spherical structures.[255] Example experimental results that represent typical behaviors and regimes for SLES are shown in Figs 7.9-7.10. Below the CMC (~0.03wt%), the trajectories and potential energy profiles indicate that the capsules are electrostatically stabilized and do not deposit (see the Debye length plot, Fig. 7.11c). Then, as SLES is increased to concentrations an order of magnitude above the CMC, particles start to deposit onto the surface as the surfactants form micelles and the depletion attraction, eq. (7.13), contributes to the particle-surface interaction. As the surfactant concentration increases further (1.2wt%), all of the PDA particles deposit and most of the PGA particles deposit, also due to the increased depletion attraction. PGA is more stable than PDA because it is more negatively charged, as shown by zeta potential measurements, and therefore PGA has greater electrostatic repulsion. This is also supported by the PDA and PGA energy plots as a function of salt: PGA particles remain stable in 1mM NaCl, while PDA particles all deposit. In addition, the polymer surface groups on the PGA particles may form a thick

layer (molecular weight on the order of 1E5 g/mole), leading to effectively larger particles and greater steric repulsion, eq. (7.17), compared to the polymer surface groups on PDA, which has a molecular weight on the order of 1E4 g/mole.

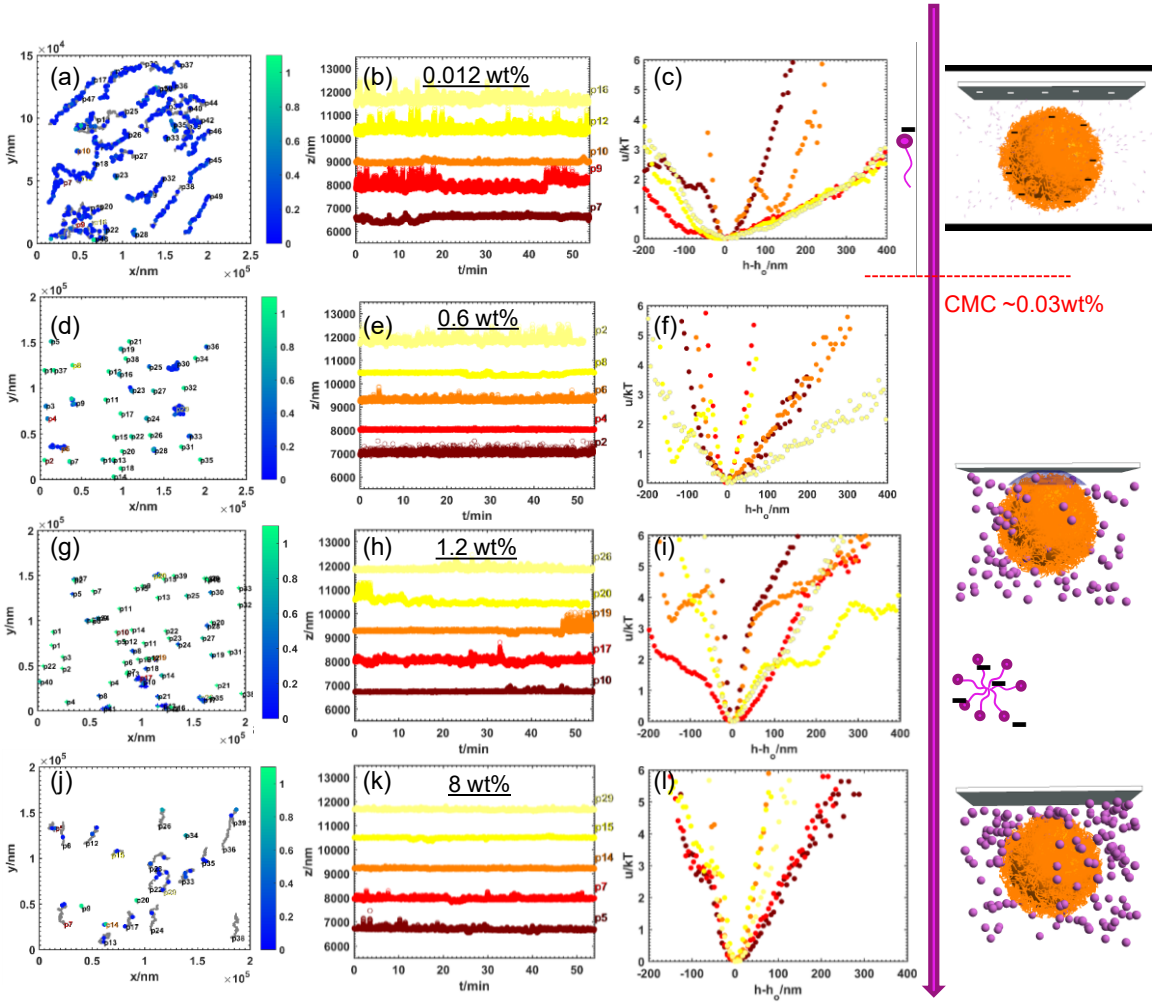

Figure 7.10: Trajectories and potential energies of several trials of PGA particles at four different SLES concentrations representing the four main regimes. Particle trajectories in the x-y plane are color-coded by the deposition lifetime parameter, and representative trajectories in height are shown along with the corresponding potential energy profiles for (a-c) 0.012wt% SLES, (d-f) 0.6wt% SLES, (g-i) 1.2wt% SLES and (j-l) 8wt% SLES. At the lowest concentration below the CMC, the particles are stable due to electrostatic repulsion. Above the CMC, the particles begin to deposit due to the formation of micelles that causes a depletion attraction, and then at the even higher concentrations, the depletants start to pack around the microcapsule, causing oscillatory concentration profiles of the micelle and a barrier that causes kinetic depletion-induced stabilization. Compared to the PDA particles, the PGA particles are more stable, even at 1.2wt% of the SLES, indicating that they have more electrostatic repulsion or possibly steric repulsion due to the polymer-functionalized surface.

As the concentration of SLES increases further, both PDA and PGA particles become more stable and fewer deposit onto the surface of the slide. This behavior is most likely due to depletion stabilization, eq. (7.15), as the micelles pack between the microcapsule and the surface, creating a potential energy barrier.[221] Supporting this theory is a plot of the volume fraction of micelles as a function of SLES, calculated using eq. (7.16), illustrating that above 4wt% SLES, the micelle volume fraction increases to 0.1, about the same concentration where repulsion appears in other systems.[223]

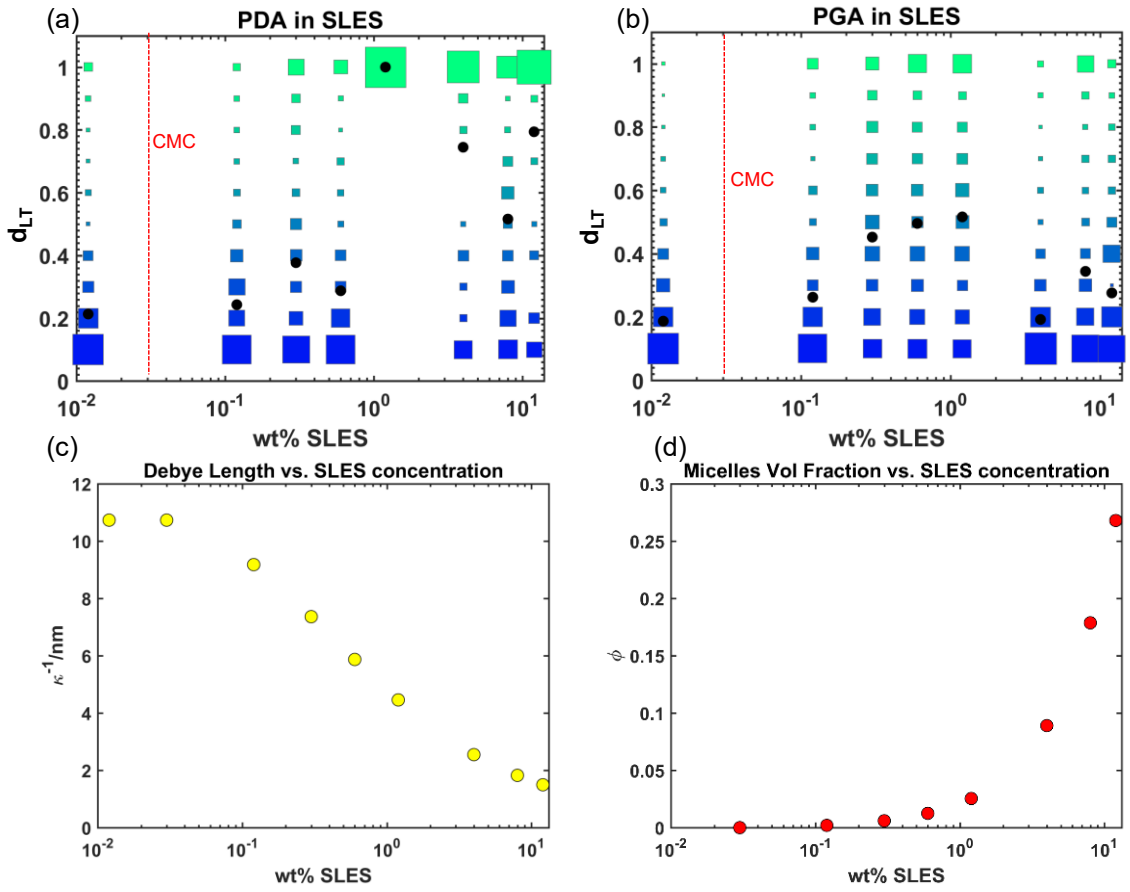

Figure 7.11: Summary results for all of the experiments of (a) PDA and (b) PGA particles across a range of SLES concentrations. The areas of the squares correspond to the deposition lifetime histograms of all of the trials at each concentration, showing that the particles are stable at low concentrations (blue squares) but deposit due to the depletion attraction as the concentration increases (turquois squares). At higher concentrations, the particles are more stable due to depletion repulsion. The black dots are the average of the deposition lifetime measurements of several trials for each concentration. Also shown are (c) the Debye length calculated from eq. (7.11) and (d) the volume fraction of micelles calculated from eq. (7.16).

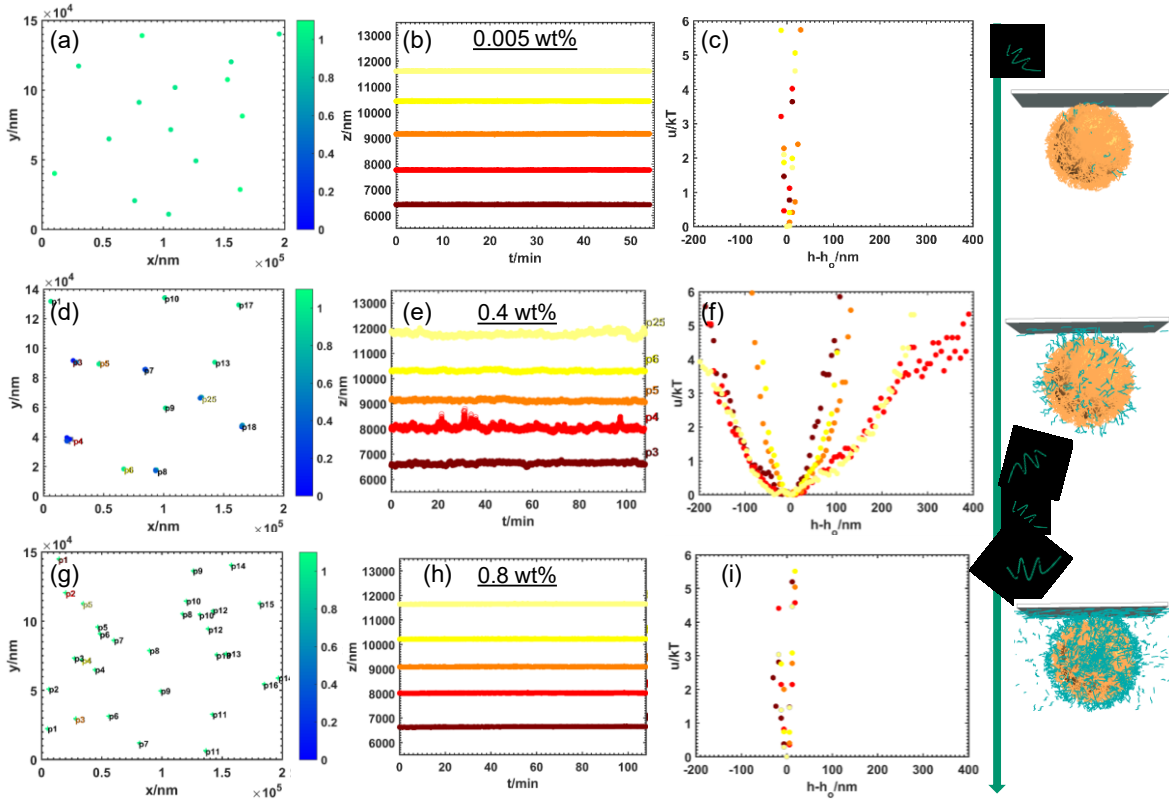

Figure 7.12: PDA particles with SC60, representing the three main regimes. The planar trajectories, trajectories in z, and the corresponding potential energy profiles for (a-c) 0.005wt% SC60, (d-f) 0.4wt% SC 60 and (g-i) 0.8wt% SC60, showing that tethering occurs in all three regimes, but that the flexible, multiple chain tethers at 0.4wt% enable the particles to diffuse in x, y and z. At the higher concentration, excess polymer in the bulk may also contribute to a depletion attraction in addition to the tight potential binding the particles to the surface due to the tethers.

Fig 7.11 shows summary plots of all of the experimental data for PDA and PGA particles in solutions with varying SLES concentrations. Deposition lifetime histograms are combined for all experiments and are plotted as squares where the area of the square is proportional to the number of times that particular lifetime was observed. The average deposition lifetime for each SLES concentration is also shown. These plots illustrate the key trends observed as SLES concentration is increased: electrostatic stabilization, then depletion attraction, and then depletion attraction and stabilization. Again, PDA and PGA display similar deposition behavior, except that the stronger electrostatic repulsion makes the PGA particles slightly more stable, which counteracts the depletion attraction. The

PGA particles would also be further from the surface; hence the depletion stabilization effect would be enhanced as the micelles pack between the particle and the substrate.

7.4.7. Buckled Particle Deposition and Mechanisms as a Function of SC60

Representative trajectory and energy plots are shown for the three observed regimes for buckled particles PDA and PGA interacting with a glass slide in the presence of SC60 in Fig 7.12-13. The plots show that PDA and PGA have very similar behavior. With the addition of a small amount of SC60 (0.005wt%-0.05wt%), all of the particles deposit, as can be seen by the turquois dots on the *x-y* plot indicating the particles are stuck throughout the length of the video. The trajectory in *z* is flat and the potential energy profiles are narrow and deep, and would be delta functions in the absence of noise, characteristic of irreversible deposition (Case III). Since SC60 is positively charged and both the microcapsules and substrate are anionic, it is favorable for the SC60 to be adsorbed as much as possible to both surfaces. As a consequence, a flat, single chain SC60 molecule tethers the microcapsule tightly to the glass slide, leading to multiple attachment locations and an effectively larger N, or number of tethers, and smaller contour length, L_T in eq. (7.18).

When the concentration of SC60 is increased, the microcapsules show some movement in *x* and *y* (although limited) and also appear to fluctuate in *z*. The resulting potential energy plots are U-shaped, indicative of the harmonic well observed for flexible tethered particle-surface systems.[75] The mechanism in this case can be explained as follows: as more SC60 molecules coat the surface of the slide and the microcapsule, steric interactions between the molecules cause them to space out and they can no longer lie parallel on the surfaces, as was the case for the molecules in much lower concentrations, <~0.05wt%. Hence, multiple SC60 molecules form longer, flexible tethers between the microcapsules and slide,

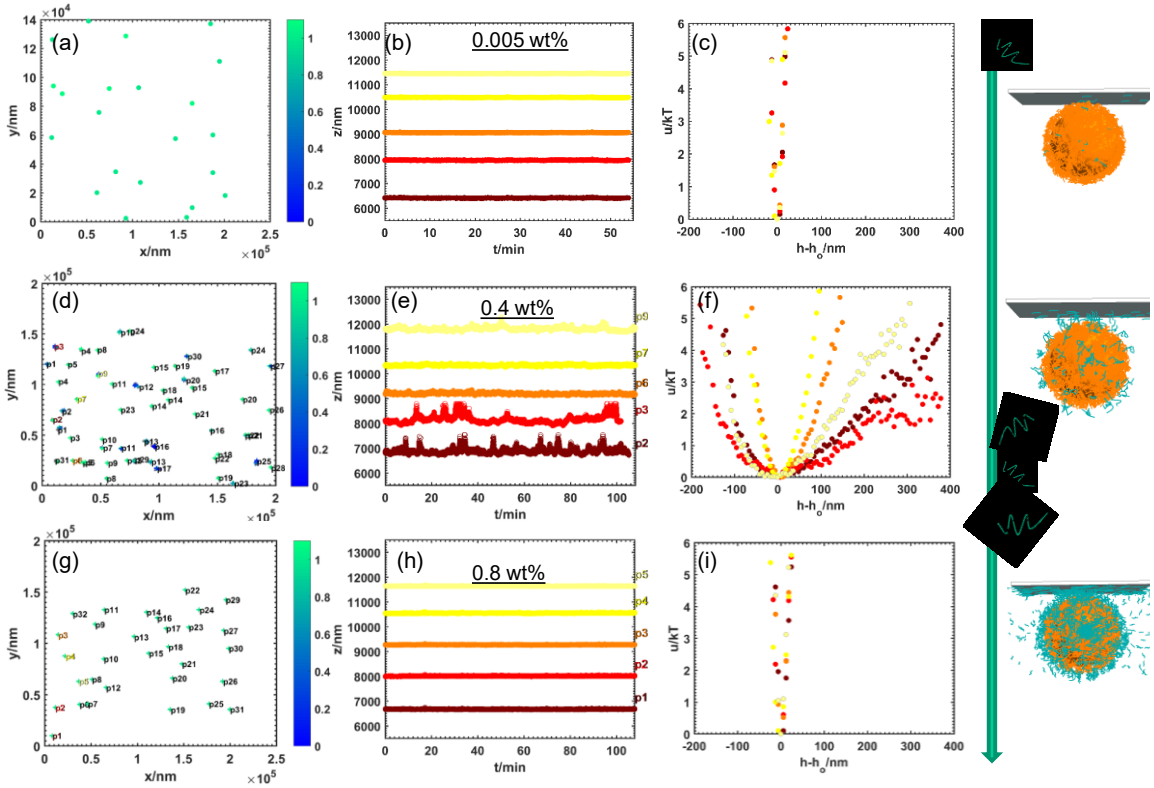

Figure 7.13: PGA particles with SC60, representing the three main regimes. The planar trajectories, trajectories in z, and the corresponding potential energy profiles for (a-c) 0.005wt% SC60, (d-f) 0.4wt% SC 60 and (g-i) 0.8wt% SC60, showing that tethering occurs in all three regimes, but that the flexible, multiple chain tethers at 0.4wt% enable the particles to diffuse in x, y and z. At the higher concentration, excess polymer in the bulk may also contribute to a depletion attraction in addition to the tight potential binding the particles to the surface due to the tethers. The plots indicate that the mechanisms are almost identical to the PDA particles.

enabling the capsules to sample limited coordinates in all three dimensions. However, as the SC60 concentration increases even more, the particles all deposit again. Here, the addition of more molecules/tethers would increase the interaction strength with an increase in N (eq. (7.18)). In addition, at higher polymer concentrations, depletion attraction would have an impact as the microcapsule and slide surfaces become saturated with SC60 and there is a significant unabsorbed polymer concentration in the bulk.[76]

Fig 7.14. summarizes the deposition results for buckled particles PGA and PDA as a function of SC60 concentration from 0.005wt% to 1wt% (common shampoo and conditioner formulations are ~0.5wt% cationic polymer). No deposition at 0wt% (DI water) is also plotted as a reference.

7.4.8. Size Effects on Buckled Particle Deposition

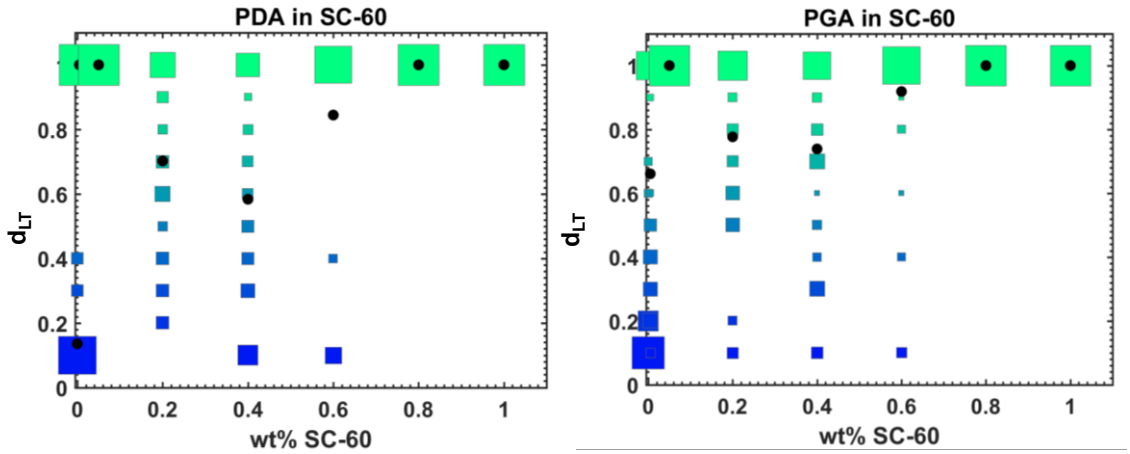

Figure 7.14: Summary results for all of the experiments of PDA and PGA particles across a range of SC60 concentrations. The areas of the squares correspond to the deposition lifetime histograms of all of the trials at each concentration, with blue squares at 0wt% (DI water) as a reference, meaning the particles are stable until a small wt% of SC60 is added (tight chain tethering). Then, with increasing concentration of SC60, flexible tethers, due to the steric interactions between the polymer tethers, enable the particles to sample several different positions. At higher concentrations, the capsules are completely deposited to the glass slide. The black dots are the average deposition lifetime for each concentration of SC60.

All of the previous deposition plots ignore size effects in the calculation of deposition lifetimes and it is assumed that the radius of the particle does not influence the observed tren for both SLES and SC60, at least for the size distribution of tl e particles (~10-20μm). However, it is evident by the theoretical particle-surface potential energies, specifically electrostatics, van der Waals, depletion attraction, s : repulsion, and tethering that the particle radius a either directly or indirectly af s the interaction strength. Following the procedure for sizing particles from optical m scopy images (as detailed in *Methods*), deposition lifetimes were calculated for representative experiments where each particle's trajectory was analyzed using a unique $\langle D_{\parallel} \rangle$ as determined by the particle size. Specific experiments were chosen for this analysis that represent intermediate regimes where some degree of both deposition and stability is observed to determine if deposition depends on particle size. Fig. 7.15 shows plots of deposition lifetimes as a function of particle size for 3 SLES concentrations and 1 SC 60 concentration, showing little correlation with microcapsule radius.

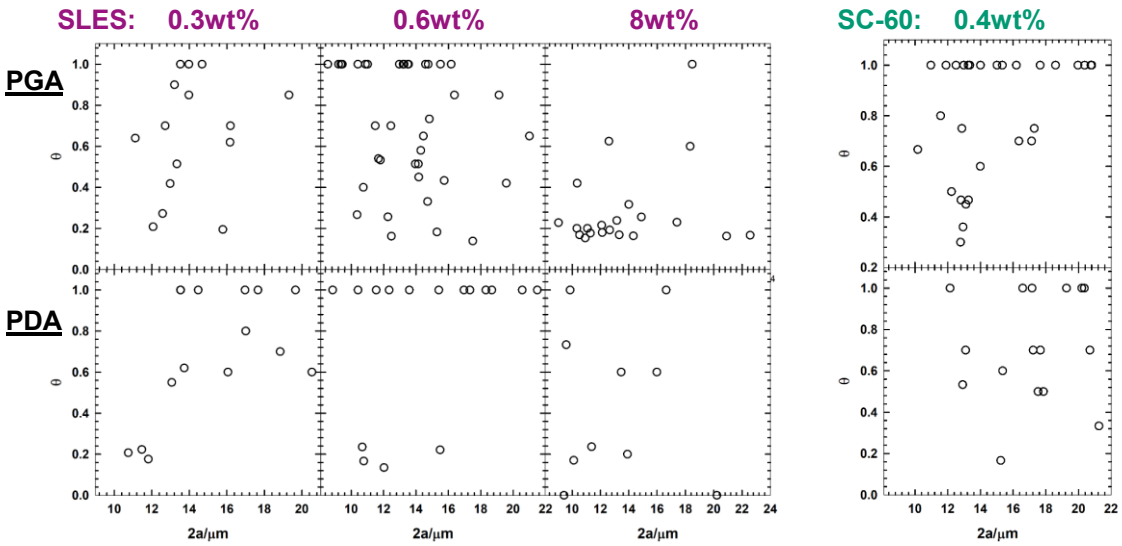

Figure 7.15: Plots of the average deposition lifetimes measured for individual particles, plotted against the sizes of the particles, as determined by image analysis (see methods). The concentrations shown are for intermediate cases where *both* deposition and stabilization occurred to see if size affected deposition. The results show that there is no obvious dependence on size, at least for this size range

7.5. Conclusions

Anisotropic capsule-surface interactions are measured and characterized using TIRM and a trajectory analysis to determine the mechanisms that lead to deposition in solutions of the surfactant SLES and the cationic polymer SC60. Although the exact theory for this system is still in development due to the shape anisotropy, the deposition results and potential energy profiles indicate that the microcapsules experience depletion-mediated deposition in the SLES solutions and polymer tethering in the SC60 solutions. These results provide an understanding of how fragrance microcapsules interact with the individual components found in a shampoo formulation. It is predicted that combining SLES and SC60 in solution would produce unique interactions that are not a sum of the individual interactions, and a combination of depletion, tethering, or steric repulsion may occur. Fragrance particle deposition in realistic formulations may be complicated, but our

foundational results presented in this study can be a guide for interpreting future experimental measurements. The mechanisms of deposition can then be exploited to improve the consumer olfactory experience as well as improve the cost-efficiency of product development.

8. CONCLUSIONS

In this dissertation, the goal was to determine the physical phenomena influencing particle dynamics, interactions and assembly in a rotating magnetic field to exploit these physics to make colloidal crystals and to understand nonequilibrium state behavior to advance the field of "active" colloidal science and engineering. Models were built that agreed with the experiments of single particles up to small clusters, enabling many high-resolution data sets to be generated to further study the dynamic modes of the systems. Using the Fokker-Planck equation, diffusivity and energy landscapes were constructed to characterize effective pair potentials and to describe assembly pathways in low-dimensional space. The secondary goal of this thesis was to characterize and measure perfume microcapsule-surface interactions as a function of common additives in shampoo, specifically a surfactant and a polymer. The following section summarizes the results and conclusions from the main topics of study in this dissertation.

First, the particle-field and particle-particle interactions were fully explained and characterized in the rotating magnetic field system. The rotation rates of doublets were observed in a rotating magnetic field quadrupole set-up, and it was unclear why the doublets continued to rotate at high field frequencies. To investigate this problem, single particles were coated on one side with a non-magnetic metal to characterize single particle-field interactions, and it was discovered that the single particles also rotate at high field

frequencies. The dynamic magnetic susceptibility describes how the two different dipoles, the Brownian and the Néel dipole, relax to orient with the field. It was determined that the particles in this study had both a Brownian and Néel dipole, and that the relaxation behavior, specifically the Néel dipole phase lag, caused the particles to continue rotating at high frequencies. It was also observed that the individual particles rotated while in rotating doublets. Brownian Dynamic simulations were conducted of the system, and showed conclusively that without the translation-rotation coupling, the doublet would not be rotating at the high frequencies. In conclusion, the hydrodynamic interactions and particle properties significantly contribute to single and doublet rotation and dynamics.

Utilizing the model generated in the first part of this thesis, simulation trajectories of two particles interacting as a function of field frequency and amplitude were generated. Unlike the experiments, the simulation data could be output at high resolutions and many statistics could be created. A blinking protocol was developed to make the simulations more efficient and to force the pairs of particles to sample many separation distances to capture their full interaction potentials. The system was reduced to a single variable, the center-to-center separation distance, to solve for the effective pair potentials via the moments of the one-dimensional Fokker-Planck equation. Results showed that the interaction well-depth and range could be controlled not only by tuning amplitude but also frequency. The pair potentials were correlated to the doublet rotation results to separate the interactions into three regimes: high frequency, critical frequency, and low frequency.

Experiments and simulations were then generated of many-particle assembly at four different field conditions to study both amplitude and frequency effects, starting from a chain. System sizes of 4, 7 and 13 particles were characterized, and simulations that

included many-body hydrodynamics accurately captured both the kinetics (time-scales) and thermodynamics (energy landscapes) of the experiments. To quantify assembly and to more simply describe the observed behaviors, low-dimensional order parameters were used and the high-dimensional data was recast as a two and one dimensional Fokker-Planck (FP) equation. The diffusivity and effective energy landscapes were then numerically calculated form trajectory data and from the solution of the FP equation. The dynamics of the experiments and simulations agreed with the dynamics of the low-dimensional Langevin dynamics, indicating that the order parameters reasonably capture most of the physics of the colloidal chain folding and assembly.

TIRM was used to measure the interactions between anisotropic buckled particles and a negatively charged glass surface to investigate the mechanisms that could promote deposition of perfume particles onto human hair. Due to the shape effects, the potentials could not be fit to any analytical theories, but the results were qualitatively compared to potentials for spherical particles to guide the analysis. In addition, a deposition lifetime parameter was created and the planar trajectories were quantified by the extent to which the particles deposited onto the surface. Based on the TIRM potentials and the binding lifetime data, it was determined that the microcapsules deposit at specific concentrations of the surfactant due to depletion attraction, while they may experience depletion kinetic stabilization at higher concentrations. In SC60, polymer tethers formed between the microcapsules and the surface, and the physics of these tethers were dependent upon the concentration of the polymer.

In conclusion, in this thesis novel experimental data was generated of two diverse particle systems, and dynamic analyses were pioneered to characterize and model the

magnetic field and the perfume microcapsule experiments. The results will guide the use of rotating magnetic fields to create ordered structures and to model unique nonequilibrium phase behaviors and systems. This is the first report of coarse-graining of a nonequilibrium colloidal system and the low-dimensional modeling technique would be useful to apply in the future to other active systems. The particle-surface results provide a foundation to designing high-depositing perfume capsules for personal care products.

9. FUTURE RESEARCH

9.1. Diffusion mapping of colloidal assembly in rotating magnetic fields

In *Chapter 6*, the potential of diffusion mapping to aid in coarse-graining was briefly discussed. Diffusion mapping reveals the 1) main dynamic modes of the high-dimensional system via an eigenvalue spectrum of the Markov probability matrix, and 2) reports eigenvectors of this matrix that can be correlated to candidate order parameters, which guides the researcher towards appropriate low-dimensional parameters. Although this technique was not used in the main body of this thesis, preliminary diffusion mapping of colloidal chain folding for 6 and 13 particles at 10 Gauss 2 Hz were conducted in collaboration with Dr. Yuguang Yang. Dr. Yang details the diffusion mapping calculation in a recent publication, in which a Hausdorff distance matrix and orientation matrix are used to build the Markov probability matrix of high-dimensional experiments and simulations.[70]

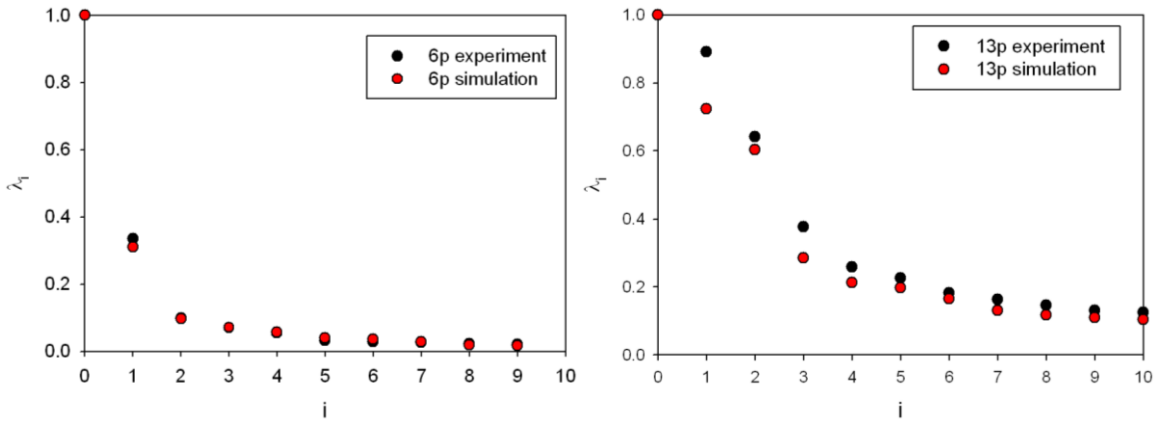

Figure 9.1: Eigenvalue spectrums for 6p and 13p Experiments and Simulations at 10 Gauss, 2 Hz. Three trajectories of each case were used to construct the Markov probability matrix. The eigenvalue spectrum can be used to determine the number of dimensions necessary to characterize the system by counting the most significant, nonzero eigenvalues. The results show that perhaps 1 order parameter is appropriate for this case for 6p, while 2-3 would be necessary for coarse-graining 13p. The fact that the spectrums look similar for the experiments vs. simulations also shows that the simulations accurately characterize the physics in the real system.

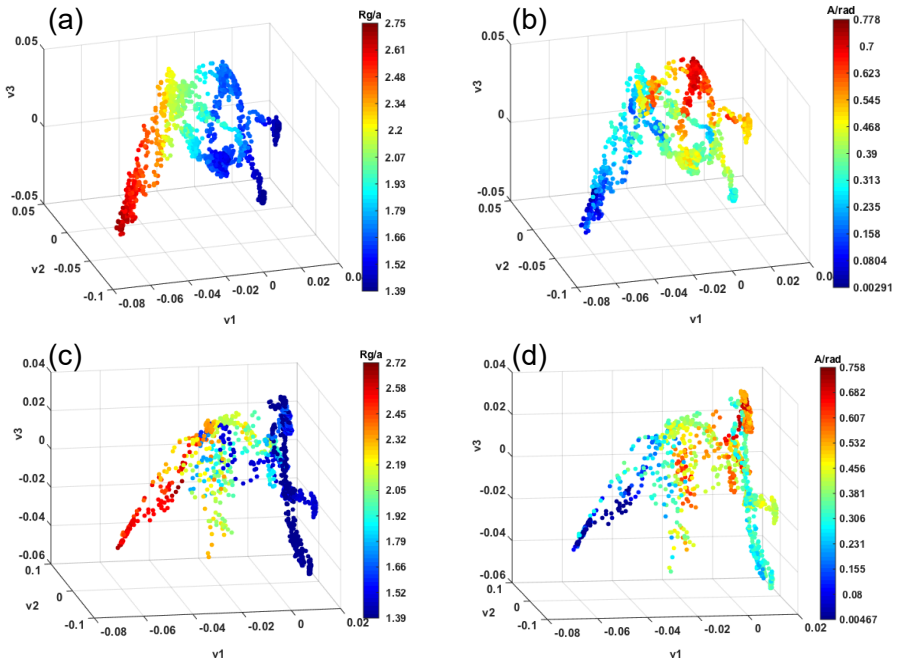

Figure 9.2: Eigenvector trajectories in time, color-coded by candidate order parameters for 6 particles at 10 Gauss, 2 Hz. The first three eigenvectors that correspond to the greatest nonzero eigenvalues are plotted in time (starting from a chain, ending in a condensed state) and color-coded according to the candidate order parameters *Rg* and *A* for the 6 particle system, again determined from 3 example trajectories from simulations (a-b) and experiments (c-d). The eigenvectors show similar behaviors for experiments vs. simulations. The colors are unique for different parts of the trajectories, indicating that the order parameters capture unique features and morphologies.

The eigenvalue spectrums from the Markov probability matrix, calculated from 3 experimental and 3 simulation trajectories each for 6 particles and 13 particles are shown in Fig 9.1. Qualitatively, the eigenvalue spectrums look similar for experiments and simulations, meaning that these preliminary simulations capture the experimental behavior well. As a note, eigenvalue spectrums can also be used in the future for fitting models to real data, providing an additional tool to supplement the previous strategy used in the *Chapter 6* where simulations were fit via first passage times. The number of nonzero eigenvalues indicates the number of dimensions needed to describe the dynamics.[68] Therefore, the spectrums show that one order parameter may be sufficient in the 6 particle case, but that 2-3 would be necessary in the 13 particle case, at least at this field condition.

The three main eigenvectors that correspond to the 3 largest, nonzero eigenvalues can also be plotted in time as the systems evolve. Shown in Fig 9.2-9.3 are the eigenvector spectrums in time color-coded with candidate order parameters *Rg* and *A* (note that in these plots, *A* is in radians). The order parameter *A* in these plots is a slightly different version that was previously presented, and the calculation is as shown,

$$A = N^{-1}\left[\sum_{i}^{N}\left(A_i - \min\left[\mathbf{A}\right]\right)^2\right]^{0.5} \tag{9.1}$$

where **A** is the same vector as before, eq. (6.9), or the average angle between all other particles for each particle.

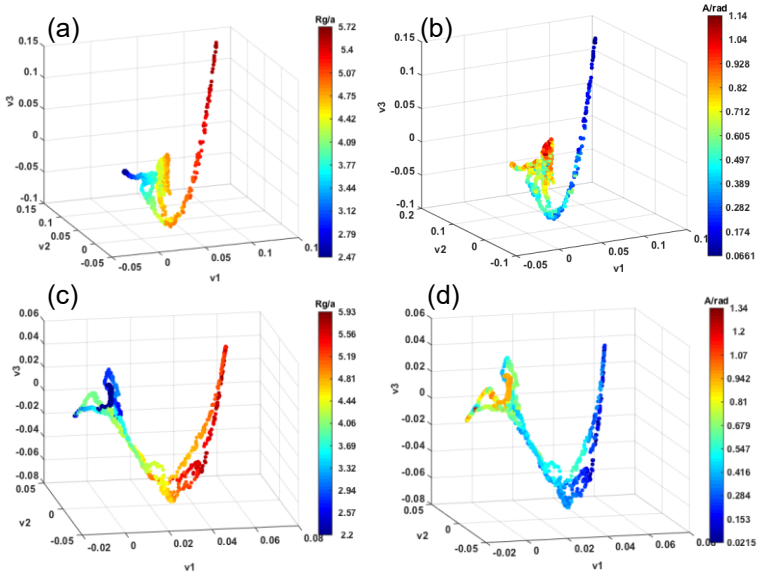

Figure 9.3: Eigenvector trajectories in time, color-coded by candidate order parameters for 13 particles at 10 Gauss, 2 Hz. The first three eigenvectors that correspond to the greatest nonzero eigenvalues are plotted in time (starting from a chain, ending in a condensed state) and color-coded according to the candidate order parameters *Rg* and *A* for the 13 particle system, again determined from 3 example trajectories from simulations (a-b) and experiments (c-d). The eigenvectors show similar behaviors for experiments vs. simulations.

These kinds of plots can be interpreted as follows: if the order parameter color-scheme follows the trajectory of the eigenvectors, then they are highly correlated to the eigenvectors and may be appropriate physical parameters to characterize the dynamics and structures. If the experiments and simulation plots look similar, this technique shows whether a model accurately reproduces real laboratory observations as well. The preliminary diffusion mapping results indicate that *Rg* and *A* are good order parameters and may be utilized in the future to improve upon the results presented in *Chapter 6*. It may be determined that different order parameters or different combinations of parameters more accurately capture passage times and energies for small cluster assembly for a range of rotating magnetic field conditions.

9.2. Colloidal chain folding and assembly in rotating magnetic fields with depletion attraction

Rotating magnetic fields are a promising tool to create colloidal crystals and to study assembly and phase behavior. However, one drawback is that the structures melt when the magnetic field is turned off. In addition, the magnetic interactions are long-range, and therefore the inclusion of a tunable, short-range interaction such as depletion[77] could be beneficial for engineering efficient assembly pathways. It was determined that the polystyrene Dynabeads presented in the main body of this thesis do not experience a depletion attraction, most likely because the manufacturer stabilizes them with surface groups that prevent them from approaching each other at the distance where depletion attraction has an effect. As a result, different superparamagnetic particles, silica iron-oxide embedded particles (Si-MAG-COOH, Microparticles Gmbh, Berlin, Germany) were used to study the affect that a short-range depletion interaction has on chain folding and assembly in rotating magnetic fields.

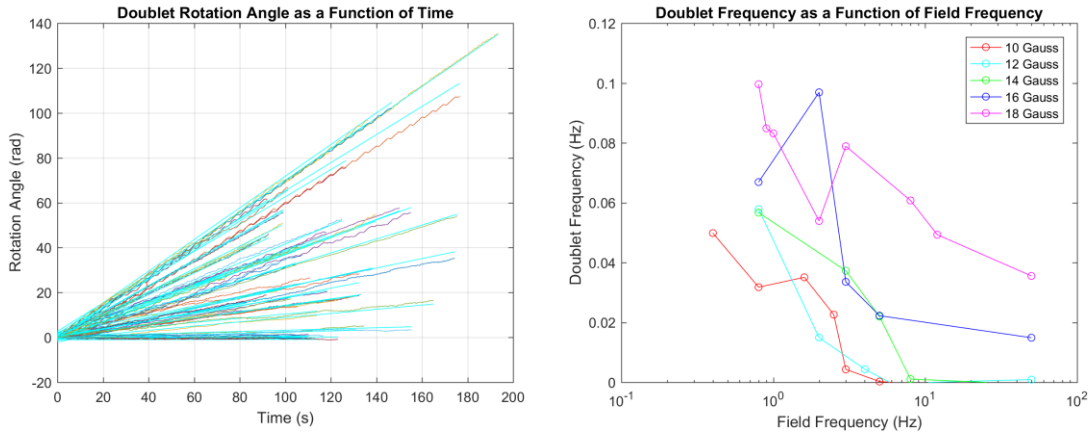

Figure 9.4: (a) Doublet rotation trajectories (b) and rotation rates as a function of field frequency at different field magnitudes for Si-MAG-COOH particles. Doublet rotation is correlated to the particle pair interactions and assembly, which was determined for Dynabeads in *Chapters 4-6*. Thus, if different magnetic beads are to be used in the future, characterization by doublet rotation is a useful and fundamental first step.

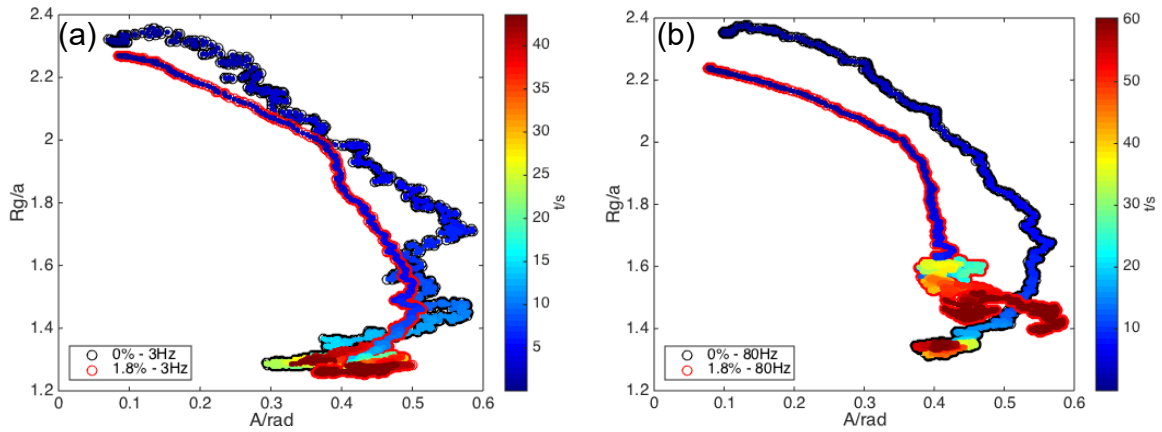

Figure 9.5: Average trajectories of experiments of a 6 particle chain forming a small cluster with and without depletants. (a) Assembly at 16 Gauss, 3 Hz, which is an intermediate frequency, with no silica depletants and with 1.8% volume depletants, where the color scale is time and the red outlined trajectory is the depletant average. (b) Assembly at 16 Gauss, 80 Hz, which is the high frequency regime, again where the color is time and the outline color (red or black) indicates with or without depletants. It can be seen that with depletants for both cases, the trajectory appears to be less stochastic, due to the added attraction keeping the particles together. At the intermediate frequency, the assembly process appears to be faster as an optimal balance exists between the depletion attraction and the intermittent attraction-repulsion due to the dipole-dipole interactions between particles. However, at the high frequency, the assembly with added depletion leads to dynamical arrest, and on average the trajectories do not reach the final state.

The Si-MAG particles are 2.4μm and preliminary doublet rotation results show that these particles have smaller magnetic moments than the Dynabeads, but display analogous relaxation behaviors and thus can be modeled in a similar manner. A preliminary doublet rotation vs. field frequency plot for several field magnitudes is shown in Fig 9.4, indicating that higher field strengths are needed for the particles to rotate at the same frequencies as observed for Dynabeads. At the lower field strengths, the particle-field interaction is weak the particles don't rotate in the high frequency regime. But as the field amplitude increases, high frequency rotation is observed.

Preliminary assembly results are shown (Figure 9.5) for experiments of Si-MAG particles in a field of 16 Gauss at 3 Hz and 80 Hz. These frequencies are chosen as they represent the critical and high frequency regimes for these particles at 16 Gauss. Solutions

are made with the Si-MAG and with either 0% volume or 1.8% volume silica nanoparticles of radius 6nm (Ludox AM 30, used in a previous study[23]). Average trajectory plots in order parameter space are shown in Fig 9.5, showing that the depletion attraction causes the particles to stay closer together, or the clusters are tighter, *i.e.* smaller *Rg,* and the dynamics are slower to reach the condensed state. The intermittent dipolar repulsion in the critical regime (3 Hz) counteracts the depletion attraction and enables the particles to sample several configurations and the clusters eventually form the final structure. But for the high frequency regime (80 Hz), the particles get stuck in a metastable intermediate state and on average they are not able to reach the final, lowest energy configuration. These results show how frequency can be used to overcome kinetic bottlenecks when attraction is added to the particles. When the field is turned off, the clusters remain in their current states due to the depletion attraction.

9.3. Multi-field, multi-component colloidal assembly

There exists a diverse array of tools and strategies that can be explored to control colloidal assembly, such as multiple fields or multiple particle systems. Although much work needs to be done to study how particles interact in both an electric quadrupole[256] set-up and in rotating magnetic fields, preliminary results provide a proof-of-concept that these techniques can be applied in parallel. In addition, previous studies have showed how unique behaviors can arise when both "active" and passive particles are together in solution,[257, 258] hence the effect that a few rotating magnetic particles have on structures of non-magnetic particles is of interest.

9.3.1. Magnetic and Electric fields

In an AC electric field applied in a quadrupolar geometry, dielectric particles move to the center of the quadrupole due to negative dielectrophoresis,[259, 260] while in a magnetic

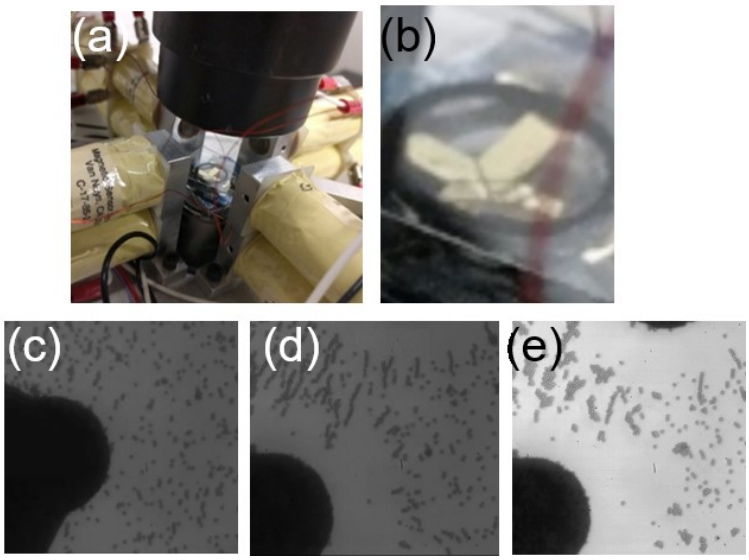

Figure 9.6: Particle Assembly In an Electric Quadrupole and in a Rotating Magnetic Field (a) An image of the quadrupolar electrode set on a stage in the middle of the solenoid set-up, and (b) a close-up of the gold-plated electrode slide. Experimental snapshots of the Si-MAG particles on the slide (c) with no applied field, (d) with the application of an AC electric field at 10V, 2kHz that causes the particles to experience negative dielectrophoresis and migrate and form chains in the center, and (e) the simultaneous application of a rotating magnetic field (18 Gauss 80 Hz) with a 8V, 2kHz electric field, that drives the particles to form crystalline structures in the center of the quadrupole.

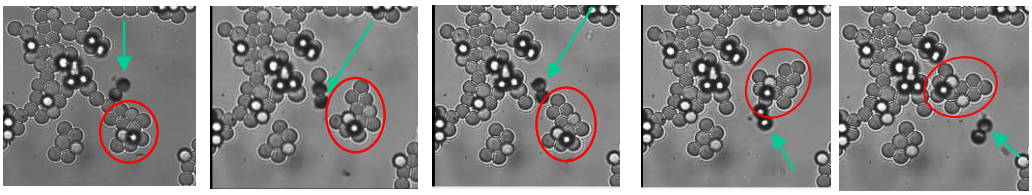

Figure 9.7: Depletion attraction in a mixture of magnetic particles and nonmagnetic particles. This series of snapshots shows a rotating doublet, indicated by the green arrow, breaking a cluster of silica particles (red circle), bound via the depletion attraction, off from a larger agglomerate. The rotating spinner then redirects the smaller cluster back on the agglomerate and it eventually merges at a different location.

field, the translational positions of the particles cannot be controlled. Thus, electric fields can be used to condense clusters in a particular space, and then magnetic fields can be used to fine-tune their assembly into hexagonally closed packed structures. Fig. 9.6 shows an image of a electric quadrupole plated onto a microscope slide, and then this slide is set on a stage in the center of the magnetic solenoid set-up. The electric field is then applied to center the particles between the electrodes. Then, the rotating magnetic field causes the particles to form quasi-two-dimensional clusters.

9.3.2. Magnetic and Non-magnetic particles

Fig 9.7 shows a preliminary result of silica particles (3μm, Bangs) in solution with 30mM SDS, which causes the particles to form crystals due to the depletion attraction. A small volume fraction of the Dynabeads are also mixed in with the silica particles. In an applied field of 5 Gauss, 50 Hz, the spinning Dynabead doublet causes a part of the silica cluster to break-off, and this cluster is then redirected by the Dynabeads and eventually merges at a different location with the larger agglomerate. This result illustrates how a few "active" particles can be used to aid in crystallization processes and could possibly break up arrested gel or glassy states at higher concentrations of the depletant.

9.4. Hierarchical assembly of magnetic particles in drops on patterned surfaces

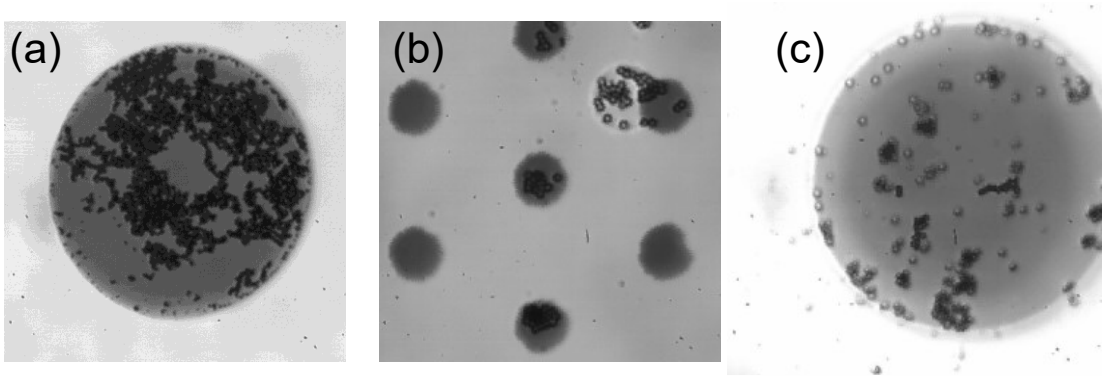

Figure 9.8: Magnetic particles in silicone oil drops on hydrophobic patterned surfaces. (a) Iron oxide paint nanoparticles, (b-c) Dynabeads.

Materials that have periodic ordered structures, and/or structures and patterns at multiple length-scales, control wavelengths along the electromagnetic spectrum in unique ways, creating photonic crystals and other novel effects. As an example, butterflies[261] and other insects[262] have intricate three-dimensional patterns on their bodies, creating brilliant colors as well as enabling camouflage. Creating hierarchical ordered structures from colloids following the bottom-up paradigm would require several layers of physics localize the particles on a macroscopic scale, and then control them on a micron scale. This strategy was employed using Si-MAG particles in silicone oil droplets in an aqueous solution. The solution is shaken vigorously to create emulsions, and then small volumes can be pipetted onto a patterned surface with hydrophobic gold patches. Fig 9.8. shows preliminary results of the magnetic particles distributed onto the patches. Future work needs to be conducted to ensure that the droplets all form on the patches, and that the magnetic particles are stable and can then be further manipulated on the small patch areas.

9.5. Microcapsule-surface interactions with surfactants and polymers and in nonequilibrium

Shampoo formulations typically contain one or more kinds of surfactants as well as polymers and thus the study of how fragrance microcapsules interact with multiple

components would be useful for designing high-depositing particles. In addition, during the shampooing process, perfume capsules are agitated and experience shears and flows, which would impact the degree to which they stick to human hair.

Fig. 9.9 displays preliminary deposition lifetime results for PDA particles in three concentrations of SLES and SC60. The most concentrated case is 12wt% SLES and 0.5wt% SC60, which are the most relevant concentrations, while the other two cases represent a 10-fold and 100-fold dilution. The results show that some of the particles are completely deposited, while others experience reversible deposition at all three cases. Future work would explore the mechanisms displayed in these plots, and would also include measurements for PGA particles. In addition, the kinetics of how the particles deposit by possibly flowing the particles through a microfluidic device would illustrate effects beyond the equilibrium measurements presented in this thesis.

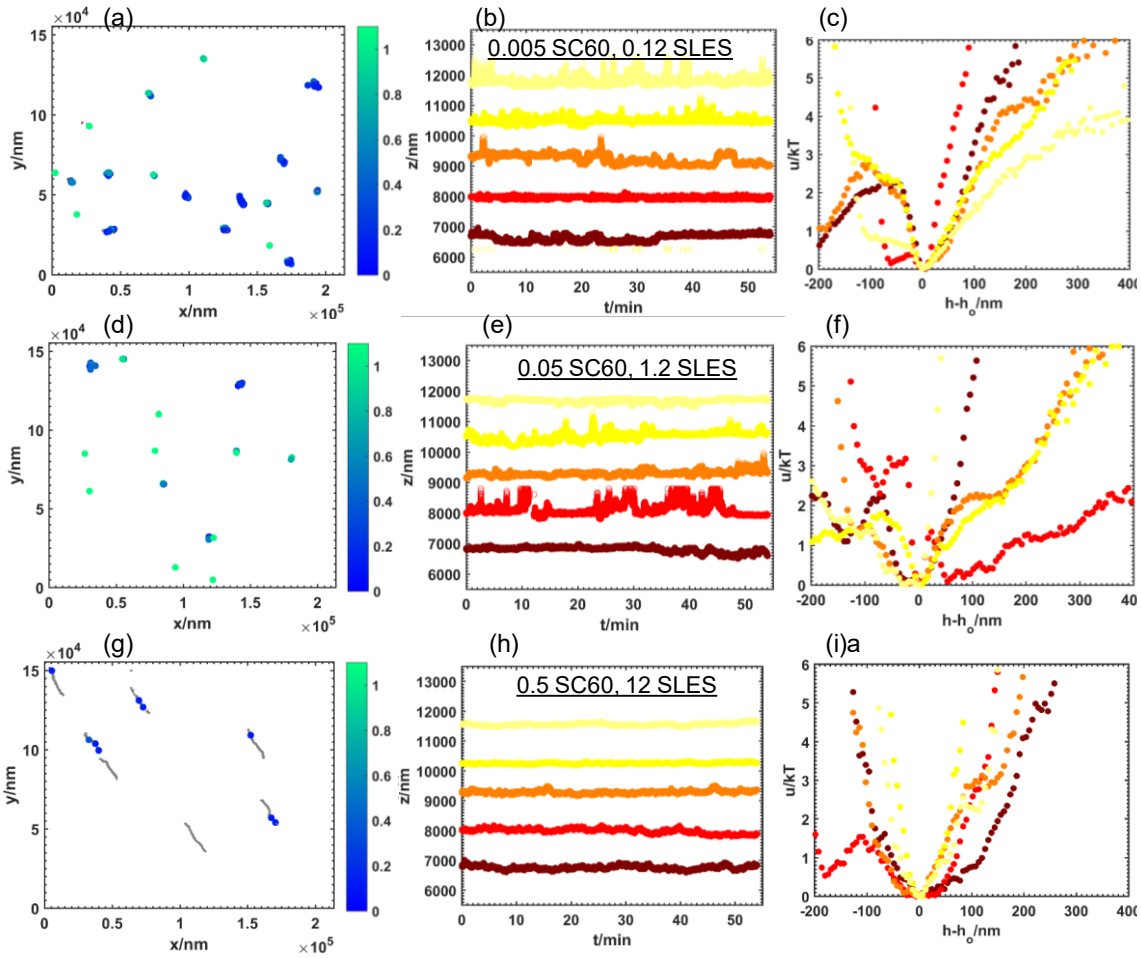

Figure 9.9. Trajectories and potential energy profiles of PDA particles interacting with a glass surface in various dilutions of both SLES and SC60. (a-c) a 100-fold dilution from the standard formulation, (d-f) a 10-fold dilution, and (g-i) the standard formulation concentrations at 0.5wt% SC60 and 12wt% SLES. The plots show that various degrees of stability occurs at all of these formulation concentrations, indicating that the deposition mechanisms are more complicated than a simple sum of the parts for the individual component cases, as was described in *Chapter 7*.

REFERENCES

1. A. C. H. Coughlan and M. A. Bevan, Physical Review E **94** (4), 042613 (2016).

2. T. Fujitani, Progress in Organic Coatings **29** (1), 97-105 (1996).

3. H. Rudolf, D. Silvio, M. Robert and Z. Matthias, Journal of Physics: Condensed Matter **18** (38), S2919 (2006).

4. J. H. Lee, Q. Wu and W. Park, Opt. Lett. **34** (4), 443-445 (2009).

5. T. Dederichs, M. Möller and O. Weichold, Langmuir **25** (4), 2007-2012 (2009).

6. K. P. Velikov and E. Pelan, Soft Matter **4** (10), 1964-1980 (2008).

7. E. A. Nance, G. F. Woodworth, K. A. Sailor, T.-Y. Shih, Q. Xu, G. Swaminathan, D. Xiang, C. Eberhart and J. Hanes, Science Translational Medicine **4** (149), 149ra119-149ra119 (2012).

8. L. O. Mair and R. Superfine, Soft Matter **10** (23), 4118-4125 (2014).

9. B. Mishra, B. B. Patel and S. Tiwari, Nanomedicine: Nanotechnology, Biology and Medicine **6** (1), 9-24 (2010).

10. K. A. Günay, D. Benczédi, A. Herrmann and H.-A. Klok, Advanced Functional Materials **27** (2), 1603843-n/a (2017).

11. M.-A. Bolzinger, S. Briançon and Y. Chevalier, Wiley Interdisciplinary Reviews: Nanomedicine and Nanobiotechnology **3** (5), 463-478 (2011).

12. F. Romano and F. Sciortino, Nat Mater **10** (3), 171-173 (2011).

13. F. Li, D. P. Josephson and A. Stein, Angewandte Chemie International Edition **50** (2), 360-388 (2011).

14. T. Ding, K. Song, K. Clays and C.-H. Tung, Langmuir **26** (6), 4535-4539 (2010).

15. K. A. Arpin, A. Mihi, H. T. Johnson, A. J. Baca, J. A. Rogers, J. A. Lewis and P. V. Braun, Advanced Materials **22** (10), 1084-1101 (2010).

16. E. R. Weeks, J. C. Crocker, A. C. Levitt, A. Schofield and D. A. Weitz, Science **287** (5453), 627-631 (2000).

17. A. Yethiraj and A. van Blaaderen, Nature **421** (6922), 513 (2003).

18. G. M. Whitesides and B. Grzybowski, Science **295** (5564), 2418-2421 (2002).

19. A. T. Pham, Y. Zhuang, P. Detwiler, J. E. S. Socolar, P. Charbonneau and B. B. Yellen, Physical Review E **95** (5), 052607 (2017).

20. T. D. Edwards, D. J. Beltran-Villegas and M. A. Bevan, Soft Matter **9** (38), 9208-9218 (2013).

21. E. M. James and S. Alexey, Reports on Progress in Physics **76** (12), 126601 (2013).

22. L. Jan, C. Punckt, B. Khusid and I. A. Aksay, Langmuir **29** (8), 2498-2505 (2013).

23. T. D. Edwards and M. A. Bevan, Langmuir **28** (39), 13816-13823 (2012).

24. J. W. Swan, J. L. Bauer, Y. Liu and E. M. Furst, Soft Matter **10** (8), 1102-1109 (2014).

25. D. Du, D. Li, M. Thakur and S. L. Biswal, Soft Matter **9** (29), 6867-6875 (2013).

26. A. Nacev, I. N. Weinberg, P. Y. Stepanov, S. Kupfer, L. O. Mair, M. G. Urdaneta, M. Shimoji, S. T. Fricke and B. Shapiro, Nano Letters **15** (1), 359-364 (2015).

27. R. Patel and B. Chudasama, Physical Review E **80** (1), 012401 (2009).

28. D. L. Ermak and J. A. McCammon, J. Chem. Phys. **69** (4), 1352-1360 (1978).

29. a. J F Brady and G. Bossis, Annual Review of Fluid Mechanics **20** (1), 111-157 (1988).

30. H. A. Jerri, M. Jacquemond, C. Hansen, L. Ouali and P. Erni, Advanced Functional Materials **26** (34), 6224-6237 (2016).

31. S. B. Trisnanto and Y. Kitamoto, Phys. Rev. E **90** (3), 032306 (2014).

32. W. F. Brown, Jr., J. Appl. Phys. **130** (5), 1677-1686 (1963).

33. P. C. Fannin, B. K. P. Scaife and S. W. Charles, J. Magn. Magn. Mater. **72** (1), 95-108 (1988).

34. P. C. Fannin, L. Cohen-Tannoudji, E. Bertrand, A. T. Giannitsis, C. Mac Oireachtaigh and J. Bibette, Journal of Magnetism and Magnetic Materials **303** (1), 147-152 (2006).

35. B. H. Erné, M. Claesson, S. Sacanna, M. Klokkenburg, E. Bakelaar and B. W. M. Kuipers, J. Magn. Magn. Mater. **311** (1), 145-149 (2007).

36. M. M. van Oene, L. E. Dickinson, F. Pedaci, M. Köber, D. Dulin, J. Lipfert and N. H. Dekker, Phys. Rev. Lett. **114** (21), 218301 (2015).

37. X. J. A. Janssen, A. J. Schellekens, K. van Ommering, L. J. van Ijzendoorn and M. W. J. Prins, Biosens. Bioelectron. **24** (7), 1937-1941 (2009).

38. J. Yan, M. Bloom, S. C. Bae, E. Luijten and S. Granick, Nature **491** (7425), 578-581 (2012).

39. S. K. Smoukov, S. Gangwal, M. Marquez and O. D. Velev, Soft Matter **5** (6), 1285-1292 (2009).

40. I. Sinn, P. Kinnunen, S. N. Pei, R. Clarke, B. H. McNaughton and R. Kopelman, Applied Physics Letters **98** (2), 024101 (2011).

41. E. C. Crittenden and R. W. Hoffman, Reviews of Modern Physics **25** (1), 310-315 (1953).

42. B. Shapiro, S. Kulkarni, A. Nacev, S. Muro, P. Y. Stepanov and I. N. Weinberg, Wiley interdisciplinary reviews. Nanomedicine and nanobiotechnology **7** (3), 446-457 (2015).

43. J. Lim, C. Lanni, E. R. Evarts, F. Lanni, R. D. Tilton and S. A. Majetich, ACS Nano **5** (1), 217-226 (2011).

44. S. L. Biswal and A. P. Gast, Physical Review E **69** (4), 041406 (2004).

45. D. Du, E. Hilou and S. L. Biswal, Physical Review E **93** (6), 062603 (2016).

46. S. Melle, G. G. Fuller and M. A. Rubio, Phys. Rev. E **61** (4), 4111-4117 (2000).

47. S. Melle, O. G. Calderón, G. G. Fuller and M. A. Rubio, J. Colloid Interface Sci. **247** (1), 200-209 (2002).

48. R. Soheilian, Y. S. Choi, A. E. David, H. Abdi, C. E. Maloney and R. M. Erb, Langmuir **31** (30), 8267-8274 (2015).

49. P. Dominguez-Garcia, S. Melle, O. Calderon and M. A. Rubio, Colloids Surf., A **270-271**, 270-276 (2005).

50. Y. Gao, M. A. Hulsen, T. G. Kang and J. M. J. den Toonder, Phys. Rev. E **86** (4), 041503 (2012).

51. N. Casic, S. Schreiber, P. Tierno, W. Zimmermann and T. M. Fischer, EPL (Europhysics Letters) **90** (5), 58001 (2010).

52. S. Krishnamurthy, A. Yadav, P. E. Phelan, R. Calhoun, A. K. Vuppu, A. A. Garcia and M. A. Hayes, Microfluidics and Nanofluidics **5** (1), 33-41 (2008).

53. K. Müller, N. Osterman, D. Babič, C. N. Likos, J. Dobnikar and A. Nikoubashman, Langmuir **30** (18), 5088-5096 (2014).

54. T. Mohorič, G. Kokot, N. Osterman, A. Snezhko, A. Vilfan, D. Babič and J. Dobnikar, Langmuir **32** (20), 5094-5101 (2016).

55. J. Yan, S. C. Bae and S. Granick, Soft Matter **11** (1), 147-153 (2015).

56. P. Tierno, R. Muruganathan and T. M. Fischer, Phys. Rev. Lett. **98** (2), 028301 (2007).

57. S. Jäger, H. Stark and S. H. L. Klapp, J. Phys.: Condens. Matter **25** (19), 195104 (2013).

58. X. Tang, B. Rupp, Y. Yang, T. D. Edwards, M. A. Grover and M. A. Bevan, ACS Nano **10** (7), 6791-6798 (2016).

59. S. Kim and S. J. Karrila, *Microhydrodynamics: Principles and Selected Applications*. (Dover Publications, 2005).

60. T. Geyer and U. Winter, The Journal of Chemical Physics **130** (11), 114905 (2009).

61. Z. Varga, G. Wang and J. Swan, Soft Matter **11** (46), 9009-9019 (2015).

62. J. J. Gray and R. T. Bonnecaze, The Journal of Chemical Physics **114** (3), 1366-1381 (2001).

63. T. Ando, E. Chow and J. Skolnick, The Journal of Chemical Physics **139** (12), 121922 (2013).

64. A. R. Dinner, A. Šali, L. J. Smith, C. M. Dobson and M. Karplus, Trends in Biochemical Sciences **25** (7), 331-339 (2000).

65. D. I. Kopelevich, A. Z. Panagiotopoulos and I. G. Kevrekidis, The Journal of Chemical Physics **122** (4), 044908 (2005).

66. G. Porte, J.-F. Berret and J. L. Harden, Journal de Physique II **7** (3), 459-472 (1997).

67. D. J. Beltran-Villegas, R. M. Sehgal, D. Maroudas, D. M. Ford and M. A. Bevan, The Journal of Chemical Physics **135** (15), 154506 (2011).

68. R. R. Coifman, I. G. Kevrekidis, S. Lafon, M. Maggioni and B. Nadler, Multiscale Modeling & Simulation **7** (2), 842-864 (2008).

69. A. L. Ferguson, A. Z. Panagiotopoulos, P. G. Debenedetti and I. G. Kevrekidis, The Journal of Chemical Physics **134** (13), 135103 (2011).

70. Y. Yang, R. Thyagarajan, D. M. Ford and M. A. Bevan, The Journal of Chemical Physics **144** (20), 204904 (2016).

71. B. V. Derjaguin and L. Landau, Acta Phys. Chim. URSS **14**, 633-662 (1941).

72. E. J. W. Verwey, J. T. G. Overbeek and K. van Nes, *Theory of the Stability of Lyophobic Colloids: The Interaction of Sol Particles Having an Electric Double Layer*. (Elsevier Publishing Company, 1948).

73. D. H. Napper, Journal of Colloid and Interface Science **58** (2), 390-407 (1977).

74. J. Y. Walz and A. Sharma, Journal of Colloid and Interface Science **168** (2), 485-496 (1994).

75. S. L. Eichmann, G. Meric, J. C. Swavola and M. A. Bevan, Langmuir **29** (7), 2299-2310 (2013).

76. E. S. Pagac, R. D. Tilton and D. C. Prieve, Langmuir **14** (18), 5106-5112 (1998).

77. G. E. Fernandes, D. J. Beltran-Villegas and M. A. Bevan, Langmuir **24** (19), 10776-10785 (2008).

78. D. C. Prieve, Advances in Colloid and Interface Science **82** (1), 93-125 (1999).

79. S. G. Fronczak, J. Dong, C. A. Browne, E. C. Krenek, E. I. Franses, S. P. Beaudoin and D. S. Corti, Langmuir **33** (3), 714-725 (2017).

80. J. C. Crocker, J. A. Matteo, A. D. Dinsmore and A. G. Yodh, Physical Review Letters **82** (21), 4352-4355 (1999).

81. F. Gittes and C. F. Schmidt, European Biophysics Journal **27** (1), 75-81 (1998).

82. J. N. Israelachvili, in *Intermolecular and Surface Forces (Third Edition)* (Academic Press, San Diego, 2011), pp. 291-340.

83. J. N. Israelachvili, in *Intermolecular and Surface Forces (Third Edition)* (Academic Press, San Diego, 2011), pp. 107-132.

84. M. A. Bevan and D. C. Prieve, Langmuir **15** (23), 7925-7936 (1999).

85. H. J. Wu, W. N. Everett, S. G. Anekal and M. A. Bevan, Langmuir **22** (16), 6826-6836 (2006).

86. J. D. Jackson, *Classical Electrodynamics*, Third ed. (John Wiley & Sons, New York, NY, 1998).

87. D. Du, F. Toffoletto and S. L. Biswal, Physical Review E **89** (4), 043306 (2014).

88. S. Asakura and F. Oosawa, The Journal of Chemical Physics **22** (7), 1255-1256 (1954).

89. A. Sharma and J. Y. Walz, Journal of the Chemical Society-Faraday Transactions **92** (24), 4997-5004 (1996).

90. R. Daniel, B. Clemens and L. Paul, Journal of Physics: Condensed Matter **11** (50), 10073 (1999).

91. R. Tuinier, G. A. Vliegenthart and H. N. W. Lekkerkerker, The Journal of Chemical Physics **113** (23), 10768-10775 (2000).

92. A. Einstein, Annalen der Physik **322** (8), 549-560 (1905).

93. H. Risken, in *The Fokker-Planck Equation: Methods of Solution and Applications* (Springer Berlin Heidelberg, Berlin, Heidelberg, 1984), pp. 63-95.

94. E. Dickinson, S. A. Allison and J. A. McCammon, J. Chem. Soc., Faraday Trans. 2 **81** (4), 591-601 (1985).

95. J. Weber, Physical Review **101** (6), 1620-1626 (1956).

96. D. J. Jeffrey and Y. Onishi, J. Fluid Mech. **139**, 261-290 (1984).

97. H. Brenner, Chem. Eng. Sci. **16** (3–4), 242-251 (1961).

98. A. J. Goldman, R. G. Cox and H. Brenner, Chemical Engineering Science **22** (4), 637-651 (1967).

99. H. Jerri, V. Normand and C. Hansen, Patent, Publication Number WO2016193435 A1 (Dec 8, 2016).

100. C. P. Lapointe, Ph.D. Thesis, The Johns Hopkins University, 2008.

101. M. H. Lee, C. P. Lapointe, D. H. Reich, K. J. Stebe and R. L. Leheny, Langmuir **25** (14), 7976-7982 (2009).

102. J. C. Crocker and D. G. Grier, Journal of Colloid and Interface Science **179** (1), 298-310 (1996).

103. M. Fixman, J. Chem. Phys. **69** (4), 1527-1537 (1978).

104. C. E. Sing, L. Schmid, M. F. Schneider, T. Franke and A. Alexander-Katz, Proc. Natl. Acad. Sci. U.S.A. **107** (2), 535-540 (2010).

105. S. Y. Park, H. Handa and A. Sandhu, Nano Lett. **10** (2), 446-451 (2010).

106. S. Bleil, D. W. M. Marr and C. Bechinger, Appl. Phys. Lett. **88** (26), 263515 (2006).

107. T. O. Tasci, P. S. Herson, K. B. Neeves and D. W. M. Marr, Nat. Commun. **7** (2016).

108. J. de Vicente, D. J. Klingenberg and R. Hidalgo-Alvarez, Soft Matter **7** (8), 3701-3710 (2011).

109. A. Weddemann, F. Wittbracht, B. Eickenberg and A. Hütten, Langmuir **26** (24), 19225-19229 (2010).

110. J. Yan, M. Bloom, S. C. Bae, E. Luijten and S. Granick, Nature (London) **491** (7425), 578-581 (2012).

111. J. W. Swan, P. A. Vasquez, P. A. Whitson, E. M. Fincke, K. Wakata, S. H. Magnus, F. D. Winne, M. R. Barratt, J. H. Agui, R. D. Green, N. R. Hall, D. Y. Bohman, C. T. Bunnell, A. P. Gast and E. M. Furst, Proc. Natl. Acad. Sci. U.S.A. **109** (40), 16023-16028 (2012).

112. I. Petousis, E. Homburg, R. Derks and A. Dietzel, Lab Chip **7** (12), 1746-1751 (2007).

113. S. Krishnamurthy, A. Yadav, P. E. Phelan, R. Calhoun, A. K. Vuppu, A. A. Garcia and M. A. Hayes, Microfluid Nanofluid **5** (1), 33-41 (2008).

114. J. Dobnikar, A. Snezhko and A. Yethiraj, Soft Matter **9** (14), 3693-3704 (2013).

115. A. van Reenen, A. M. de Jong and M. W. J. Prins, Lab Chip **15** (13), 2864-2871 (2015).

116. G. Helgesen, P. Pieranski and A. T. Skjeltorp, Phys. Rev. A **42** (12), 7271-7280 (1990).

117. B. E. Kashevsky and V. A. Kuzmin, J. Phys. D **29** (10), 2579 (1996).

118. K. Takamura, H. L. Goldsmith and S. G. Mason, J. Colloid Interface Sci. **72** (3), 385-400 (1979).

119. D. Velegol, S. Catana, J. L. Anderson and S. Garoff, Phys. Rev. Lett. **83** (6), 1243-1246 (1999).

120. T. G. Kang, Y. Gao, M. A. Hulsen, J. M. J. den Toonder and P. D. Anderson, Comput. Fluids **86**, 569-581 (2013).

121. A. Ranzoni, X. J. A. Janssen, M. Ovsyanko, L. J. van Ijzendoorn and M. W. J. Prins, Lab Chip **10** (2), 179-188 (2010).

122. D. J. Jeffrey and Y. Onishi, J. Fluid Mech. **139** (FEB), 261-290 (1984).

123. D. J. Beltran-Villegas, B. A. Schultz, N. H. P. Nguyen, S. C. Glotzer and R. G. Larson, Soft Matter **10** (26), 4593-4602 (2014).

124. W. B. Russel, D. A. Saville and W. R. Schowalter, *Colloidal Dispersions*. (Cambridge University Press, New York, 1989).

125. K. S. Cole and R. H. Cole, J. Chem. Phys. **9** (4), 341-351 (1941).

126. J. Liu and R. G. Larson, J. Chem. Phys. **138** (17), 174904 (2013).

127. J. W. Swan and J. F. Brady, Phys. Fluids **19** (11), 113306 (2007).

128. J. C. Crocker and D. G. Grier, J. Colloid Interface Sci. **179** (1), 298-310 (1996).

129. M. Fixman, J. Chem. Phys. **69** (4), 1527-1537 (1978).

130. P. S. Grassia, E. J. Hinch and L. C. Nitsche, J. Fluid Mech. **282**, 373-403 (1995).

131. S. Anekal and M. A. Bevan, J. Chem. Phys. **122**, 034903 (2005).

132. S. Anekal and M. A. Bevan, J. Chem. Phys. **125**, 034906 (2006).

133. D. Du, F. Toffoletto and S. L. Biswal, Phys. Rev. E **89** (4), 043306 (2014).

134. G. Fonnum, C. Johansson, A. Molteberg, S. Mørup and E. Aksnes, J. Magn. Magn. Mater. **293** (1), 41-47 (2005).

135. D. Fleisch, *A Student's Guide to Maxwell's Equations*. (Cambridge University Press, 2008).

136. A. J. Goldman, R. G. Cox and H. Brenner, Chem. Engr. Sci. **22**, 637-651 (1967).

137. D. C. Prieve, S. G. Bike and N. A. Frej, Farad. Discuss. **90** (0), 209-222 (1990).

138. O. D. Velev and K. H. Bhatt, Soft Matter **2** (9), 738-750 (2006).

139. C. E. Owens, C. W. Shields, D. F. Cruz, P. Charbonneau and G. P. Lopez, Soft Matter **12** (3), 717-728 (2016).

140. B. Ren, A. Ruditskiy, J. H. Song and I. Kretzschmar, Langmuir **28** (2), 1149-1156 (2012).

141. C. Rinaldi, A. Chaves, S. Elborai, X. He and M. Zahn, Current Opinion in Colloid & Interface Science **10** (3–4), 141-157 (2005).

142. C. Balan, D. Broboana, E. Gheorghiu and L. Vékás, Journal of Non-Newtonian Fluid Mechanics **154** (1), 22-30 (2008).

143. W. D. Ristenpart, I. A. Aksay and D. A. Saville, Physical Review E **69** (2), 021405 (2004).

144. J. J. Crassous and A. F. Demirors, Soft Matter (2016).

145. P. Tierno, R. Golestanian, I. Pagonabarraga and F. Sagués, Physical Review Letters **101** (21), 218304 (2008).

146. R. Sijie, G. Allon and F. Gary, New Journal of Physics **18** (12), 123008 (2016).

147. T. O. Tasci, P. S. Herson, K. B. Neeves and D. W. M. Marr, Nature Communications **7**, 10225 (2016).

148. B. A. Grzybowski, H. A. Stone and G. M. Whitesides, Nature **405** (6790), 1033-1036 (2000).

149. N. H. P. Nguyen, D. Klotsa, M. Engel and S. C. Glotzer, Physical Review Letters **112** (7), 075701 (2014).

150. J. Schwarz-Linek, C. Valeriani, A. Cacciuto, M. E. Cates, D. Marenduzzo, A. N. Morozov and W. C. K. Poon, Proceedings of the National Academy of Sciences **109** (11), 4052-4057 (2012).

151. F. Ginot, I. Theurkauff, D. Levis, C. Ybert, L. Bocquet, L. Berthier and C. Cottin-Bizonne, Physical Review X **5** (1), 011004 (2015).

152. Z. M. Sherman and J. W. Swan, ACS Nano **10** (5), 5260-5271 (2016).

153. T. D. Edwards, Y. Yang, W. N. Everett and M. A. Bevan, Scientific Reports **5**, 13612 (2015).

154. H. W. Moyses, R. O. Bauer, A. Y. Grosberg and D. G. Grier, Physical Review E **91** (6), 062144 (2015).

155. J. Wang, L. Xu and E. Wang, Proceedings of the National Academy of Sciences **105** (34), 12271-12276 (2008).

156. J. C. Crocker and D. G. Grier, Physical Review Letters **73** (2), 352-355 (1994).

157. A. E. Larsen and D. G. Grier, Nature **385** (6613), 230-233 (1997).

158. S. H. Behrens, J. Plewa and D. G. Grier, The European Physical Journal E **10** (2), 115-121 (2003).

159. G. A. Duncan and M. A. Bevan, Soft Matter **10** (42), 8524-8532 (2014).

160. S. K. Sainis, V. Germain and E. R. Dufresne, Physical Review Letters **99** (1), 018303 (2007).

161. T. M. Squires, J. Fluid Mech. **443**, 403-412 (2001).

162. D. J. Beltran-Villegas, R. M. Sehgal, D. Maroudas, D. M. Ford and M. A. Bevan, The Journal of Chemical Physics **132** (4), 044707 (2010).

163. C. W. Gardiner, *Handbook of stochastic methods for physics, chemistry, and the natural sciences*. (Springer-Verlag, 1985).

164. R. Kubo, M. Toda and N. Hashitsume, *Statistical Physics II: Nonequilibrium Statistical Mechanics*. (Springer, 2012).

165. R. Graham, Zeitschrift für Physik B Condensed Matter **26** (4), 397-405 (1977).

166. H. Hasegawa, Progress of Theoretical Physics **57** (5), 1523-1537 (1977).

167. J. L. Bauer, Y. Liu, M. J. Kurian, J. W. Swan and E. M. Furst, The Journal of Chemical Physics **143** (7), 074901 (2015).

168. J. K. Hamilton, P. G. Petrov, C. P. Winlove, A. D. Gilbert, M. T. Bryan and F. Y. Ogrin, **7**, 44142 (2017).

169. A. Boymelgreen, G. Yossifon and T. Miloh, Langmuir **32** (37), 9540-9547 (2016).

170. J. Yan, M. Han, J. Zhang, C. Xu, E. Luijten and S. Granick, Nat Mater **15** (10), 1095-1099 (2016).

171. D. Du, M. Doxastakis, E. Hilou and S. L. Biswal, Soft Matter **13** (8), 1548-1553 (2017).

172. R. Ni, M. A. C. Stuart and M. Dijkstra, **4**, 2704 (2013).

173. A. van Reenen, A. M. de Jong, J. M. J. den Toonder and M. W. J. Prins, Lab on a Chip **14** (12), 1966-1986 (2014).

174. R. Singh and R. Adhikari, Physical Review Letters **117** (22), 228002 (2016).

175. J. Sebastian, S. Holger and H. L. K. Sabine, Journal of Physics: Condensed Matter **25** (19), 195104 (2013).

176. M. Cieplak and S. Niewieczerzał, The Journal of Chemical Physics **130** (12), 124906 (2009).

177. T. M. Squires, Journal of Fluid Mechanics **443**, 403-412 (2001).

178. M. Tagliazucchi, E. A. Weiss and I. Szleifer, Proceedings of the National Academy of Sciences **111** (27), 9751-9756 (2014).

179. Y. Gao, J. Beerens, A. van Reenen, M. A. Hulsen, A. M. de Jong, M. W. J. Prins and J. M. J. den Toonder, Lab on a Chip **15** (1), 351-360 (2015).

180. S. Y. Park, H. Handa and A. Sandhu, Nano Letters **10** (2), 446-451 (2010).

181. J. Zhang, J. Yan and S. Granick, Angewandte Chemie International Edition **55** (17), 5166-5169 (2016).

182. F. Ma, S. Wang, D. T. Wu and N. Wu, Proceedings of the National Academy of Sciences **112** (20), 6307-6312 (2015).

183. R. W. Perry, M. C. Holmes-Cerfon, M. P. Brenner and V. N. Manoharan, Physical Review Letters **114** (22), 228301 (2015).

184. T. D. Edwards, Y. Yang, D. J. Beltran-Villegas and M. A. Bevan, **4**, 6132 (2014).

185. A. W. Long and A. L. Ferguson, The Journal of Physical Chemistry B **118** (15), 4228-4244 (2014).

186. D. Levis and L. Berthier, Physical Review E **89** (6), 062301 (2014).

187. M. Spellings, M. Engel, D. Klotsa, S. Sabrina, A. M. Drews, N. H. P. Nguyen, K. J. M. Bishop and S. C. Glotzer, Proceedings of the National Academy of Sciences **112** (34), E4642-E4650 (2015).

188. G. Kokot, D. Piet, G. M. Whitesides, I. S. Aranson and A. Snezhko, **5**, 9528 (2015).

189. W. B. Russel and A. P. Gast, The Journal of Chemical Physics **84** (3), 1815-1826 (1986).

190. H. Kumiko and S. Shin-ichi, Journal of Physics: Condensed Matter **18** (10), 2825 (2006).

191. J. Dzubiella, H. Löwen and C. N. Likos, Physical Review Letters **91** (24), 248301 (2003).

192. M. Gleiser and R. O. Ramos, Physical Review D **50** (4), 2441-2455 (1994).

193. A. C. H. Coughlan and M. A. Bevan, Manuscript submitted for publication (2017).

194. H. B. Callen and T. A. Welton, Physical Review **83** (1), 34-40 (1951).

195. J. W. Swan and J. F. Brady, Physics of Fluids **19** (11), 113306 (2007).

196. D. J. Jeffrey and Y. Onishi, Journal of Fluid Mechanics **139**, 261-290 (2006).

197. S. G. Anekal and M. A. Bevan, The Journal of Chemical Physics **125** (3), 034906 (2006).

198. M. A. Bevan and D. C. Prieve, The Journal of Chemical Physics **113** (3), 1228-1236 (2000).

199. J. Dunstan, G. Miño, E. Clement and R. Soto, Physics of Fluids **24** (1), 011901 (2012).

200. D. J. Beltran-Villegas, R. M. Sehgal, D. Maroudas, D. M. Ford and M. A. Bevan, The Journal of Chemical Physics **137** (13), 134901 (2012).

201. J. Palacci, C. Cottin-Bizonne, C. Ybert and L. Bocquet, Physical Review Letters **105** (8), 088304 (2010).

202. H. Bysell, R. Månsson, P. Hansson and M. Malmsten, Advanced Drug Delivery Reviews **63** (13), 1172-1185 (2011).

203. W. Wang, X. Liu, Y. Xie, H. a. Zhang, W. Yu, Y. Xiong, W. Xie and X. Ma, Journal of Materials Chemistry **16** (32), 3252-3267 (2006).

204. M. A. Augustin and Y. Hemar, Chemical Society Reviews **38** (4), 902-912 (2009).

205. S. Magdassi, Colloids and Surfaces A: Physicochemical and Engineering Aspects **123**, 671-679 (1997).

206. X. Shi and F. Caruso, Langmuir **17** (6), 2036-2042 (2001).

207. Y. Yan, G. K. Such, A. P. R. Johnston, H. Lomas and F. Caruso, ACS Nano **5** (6), 4252-4257 (2011).

208. J. A. Champion, Y. K. Katare and S. Mitragotri, Journal of Controlled Release **121** (1), 3-9 (2007).

209. P. Decuzzi, R. Pasqualini, W. Arap and M. Ferrari, Pharmaceutical Research **26** (1), 235 (2008).

210. P. F. Noble, O. J. Cayre, R. G. Alargova, O. D. Velev and V. N. Paunov, Journal of the American Chemical Society **126** (26), 8092-8093 (2004).

211. C. Cortez, E. Tomaskovic-Crook, A. P. R. Johnston, A. M. Scott, E. C. Nice, J. K. Heath and F. Caruso, ACS Nano **1** (2), 93-102 (2007).

212. N. C. Bellocq, S. H. Pun, G. S. Jensen and M. E. Davis, Bioconjugate Chemistry **14** (6), 1122-1132 (2003).

213. G. Luo, L. Du, Y. Wang, Y. Lu and J. Xu, Particuology **9** (6), 545-558 (2011).

214. C. Ohm, N. Kapernaum, D. Nonnenmacher, F. Giesselmann, C. Serra and R. Zentel, Journal of the American Chemical Society **133** (14), 5305-5311 (2011).

215. S. Bhaskar, K. M. Pollock, M. Yoshida and J. Lahann, Small **6** (3), 404-411 (2010).

216. J. A. Champion and S. Mitragotri, Proceedings of the National Academy of Sciences of the United States of America **103** (13), 4930-4934 (2006).

217. L. Y. T. Chou, K. Ming and W. C. W. Chan, Chemical Society Reviews **40** (1), 233-245 (2011).

218. J. Shin, X. Zhang and J. Liu, The Journal of Physical Chemistry B **116** (45), 13396-13402 (2012).

219. Z. D. Draelos, International Journal of Trichology **2** (1), 24-29 (2010).

220. Hössel, Dieing, Nörenberg, Pfau and Sander, International Journal of Cosmetic Science **22** (1), 1-10 (2000).

221. P. Richetti and P. Kékicheff, Physical Review Letters **68** (12), 1951-1954 (1992).

222. R. Pool and P. G. Bolhuis, Physical Chemistry Chemical Physics **12** (44), 14789-14797 (2010).

223. R. Tuinier, J. Rieger and C. G. de Kruif, Advances in Colloid and Interface Science **103** (1), 1-31 (2003).

224. A. Halperin, M. Tirrell and T. P. Lodge, in *Macromolecules: Synthesis, Order and Advanced Properties* (Springer Berlin Heidelberg, Berlin, Heidelberg, 1992), pp. 31-71.

225. J. M. H. M. Scheutjens and G. J. Fleer, Advances in Colloid and Interface Science **16** (1), 361-380 (1982).

226. S. Kim, K. Hyun, J. Y. Moon, C. Clasen and K. H. Ahn, Langmuir **31** (6), 1892-1900 (2015).

227. J. Philip, G. Gnanaprakash, T. Jayakumar, P. Kalyanasundaram and B. Raj, Macromolecules **36** (24), 9230-9236 (2003).

228. A. D. Braem, D. C. Prieve and R. D. Tilton, Langmuir **17** (3), 883-890 (2001).

229. A. Tulpar, R. D. Tilton and J. Y. Walz, Langmuir **23** (8), 4351-4357 (2007).

230. S. Ji and J. Y. Walz, Current Opinion in Colloid & Interface Science **20** (1), 39-45 (2015).

231. M. Delcea, S. Schmidt, R. Palankar, P. A. L. Fernandes, A. Fery, H. Möhwald and A. G. Skirtach, Small **6** (24), 2858-2862 (2010).

232. W. N. Everett, H.-J. Wu, S. G. Anekal, H.-J. Sue and M. A. Bevan, Biophysical Journal **92** (3), 1005-1013 (2007).

233. G. A. Duncan, S. Gerecht, D. H. Fairbrother and M. A. Bevan, Langmuir **32** (46), 12212-12220 (2016).

234. H. Chew, D. S. Wang and M. Kerker, Appl. Opt. **18**, 2679 (1979).

235. D. C. Prieve, Adv. Colloid Interface Sci. **82**, 93 (1999).

236. B. Derjaguin and L. Landau, Progress in Surface Science **43** (1), 30-59 (1993).

237. E. J. W. Verwey and J. T. G. Overbeek, *Theory of the stability of lyophobic colloids*. (Elsevier, Amsterdam, 1948).

238. I. E. Dzyaloshinskii, E. M. Lifshitz and P. P. Lev, Soviet Physics Uspekhi **4** (2), 153 (1961).

239. D. C. Prieve and W. B. Russel, Journal of Colloid and Interface Science **125** (1), 1-13 (1988).

240. Y. Yang, T. D. Edwards and M. A. Bevan, Journal of Colloid and Interface Science **449**, 270-278 (2015).

241. L. Schäfer, *Excluded Volume Effects in Polymer Solutions: as Explained by the Renormalization Group*. (Springer Berlin Heidelberg, 2012).

242. D. T. Wasan, A. D. Nikolov and F. Aimetti, Advances in Colloid and Interface Science **108**, 187-195 (2004).

243. D. Henderson, Journal of Colloid and Interface Science **121** (2), 486-490 (1988).

244. R. I. Feigin and D. H. Napper, Journal of Colloid and Interface Science **75** (2), 525-541 (1980).

245. M. Aoudia, B. Al-Haddabi, Z. Al-Harthi and A. Al-Rubkhi, Journal of Surfactants and Detergents **13** (1), 103-111 (2010).

246. S. Banerjee, C. Cazeneuve, N. Baghdadli, S. Ringeissen, F. A. M. Leermakers and G. S. Luengo, Soft Matter **11** (12), 2504-2511 (2015).

247. I. Torres-Díaz and M. A. Bevan, Langmuir **33** (17), 4356-4365 (2017).

248. L. Colón-Meléndez, D. J. Beltran-Villegas, G. v. Anders, J. Liu, M. Spellings, S. Sacanna, D. J. Pine, S. C. Glotzer, R. G. Larson and M. J. Solomon, The Journal of Chemical Physics **142** (17), 174909 (2015).

249. P. Hänggi, P. Talkner and M. Borkovec, Reviews of Modern Physics **62** (2), 251-341 (1990).

250. G. A. Duncan, D. H. Fairbrother and M. A. Bevan, Soft Matter **12** (21), 4731-4738 (2016).

251. G. A. Duncan and M. A. Bevan, Langmuir **30** (50), 15253-15260 (2014).

252. H.-J. Wu and M. A. Bevan, Langmuir **21** (4), 1244-1254 (2005).

253. H.-J. Wu, T. O. Pangburn, R. E. Beckham and M. A. Bevan, Langmuir **21** (22), 9879-9888 (2005).

254. J. Y. Walz, Current Opinion in Colloid & Interface Science **2** (6), 600-606 (1997).

255. M. Showell, *Handbook of Detergents, Part D: Formulation*. (CRC Press, 2016).

256. J. J. Juarez, S. E. Feicht and M. A. Bevan, Soft Matter **8** (1), 94-103 (2012).

257. F. Kummel, P. Shabestari, C. Lozano, G. Volpe and C. Bechinger, Soft Matter **11** (31), 6187-6191 (2015).

258. J. Stenhammar, R. Wittkowski, D. Marenduzzo and M. E. Cates, Physical Review Letters **114** (1), 018301 (2015).

259. J. J. Juárez, B. G. Liu, J.-Q. Cui and M. A. Bevan, Langmuir **27** (15), 9219-9226 (2011).

260. J. J. Juarez, P. P. Mathai, J. A. Liddle and M. A. Bevan, Lab on a Chip **12** (20), 4063-4070 (2012).

261. L. P. Biró, K. Kertész, Z. Vértesy, G. I. Márk, Z. Bálint, V. Lousse and J. P. Vigneron, Materials Science and Engineering: C **27** (5), 941-946 (2007).

262. B. D. Wilts, K. Michielsen, J. Kuipers, H. De Raedt and D. G. Stavenga, Proceedings of the Royal Society B: Biological Sciences (2012).

Intended to be blank

VITA

Name:	Anna C. H. Coughlan
Birth:	January, 18, 1989, Baltimore, MD
Address:	Anna C. H. Coughlan may be contacted through Dr. M.A. Bevan at the Chemical and Biomolecular Engineering Department, Johns Hopkins University, Baltimore, MD 21218
Email Address:	acoughlan18@gmail.com
Education:	B.S., Chemical Engineering, University of Rochester, 2012
Research:	Separation and Characterization of Carbon Nanotubes, with Dr. Todd Krauss, University of Rochester, Rochester, NY, 2011 Efficiency Studies of Flow Battery Designs with Dr. Jacob Jorne and Dr. Mitchell Anthamatten, University of Rochester, Rochester, NY, 2010